UNIVERSITY OF SOUTHAMPTON

FACULTY OF PHYSICAL SCIENCES AND ENGINEERING

Optoelectronics Research Centre

All Dielectric Reconfigurable Metamaterials

By

Artemios Karvounis

A Thesis for the Degree of Doctor of Philosophy

October 2017

ABSTRACT

UNIVERSITY OF SOUTHAMPTON

FACULTY OF PHYSICAL AND APPLIED SCIENCE

OPTOELECTRONICS RESEARCH CENTRE

Doctor of Philosophy

ALL-DIELECTRIC RECONFIGURABLE METAMATERIALS

by Artemios Karvounis

This thesis reports on my research efforts towards all-dielectric metamaterials with reconfigurable functionalities:

- **I have reported the first optomechanical nonlinear dielectric metamaterial**. I have shown that such metamaterials provide extremely large optomechanical nonlinearities at near infrared, operating at intensities of only a few μW per unit cell and modulation frequencies as high as 152 MHz, thereby offering a path to fast, compact, and energy efficient all-optical metadevices.

- **I have experimentally demonstrated the first all-dielectric electro-optical nano-mechanical modulator based on all-dielectric nanomembrane metamaterial**. Furthermore, I have shown the dynamical control of optical properties of this device, with modulation frequency up to 7 MHz. I have also establish an encapsulation technique where any nano-membrane can be embedded within a fiber setup with electrical feedthroughs and pressure control.

- **I have studied for first time the optical properties of Diamond nano-membrane metamaterials**. Diamond membranes after nanostructuring with Focus Ion Beam, present broadband, polarization-independent absorption that can be used as efficient coherent absorbers for optical pulses as short as 6 fs. This novel class of metamaterials have been used for coherent modulation with modulation contrast up to 40% at optical fluences of few nJ/cm^2 across the visible spectrum.

- **I have reported the first optically-switchable, all-chalcogenide phase-change metamaterial.** Germanium antimony telluride alloys (GST) after nanostructuring subwavelength-thickness films of GST present high-quality resonances that are spectrally shifted by laser-induced structural transitions, providing reflectivity and transmission switching contrast ratios of up to 5:1 (7 dB) at near-infrared wavelengths selected by design, or strong colour contrast in visible due to its plasmonic nature.

- **This work has introduced dielectric nano-membrane metamaterials, as a platform to provide optically switchable, nonlinear, reconfigurable responses.** Due to nano-mechanical actuation based on optical/electromagnetic forces, coherent modulation based on the diamond absorbers and phase change media of Chalcogenide glasses.

Table of Contents

List of Figures

Declaration of Authorship

I, Artemios Karvounis, declare that the thesis entitled "All-Dielectric Reconfigurable metamaterials" and the work presented in the thesis are both my own, and have been generated by me as the result of my own original research. I confirm that:

• this work was done wholly or mainly while in candidature for a research degree at this University;

• where any part of this thesis has previously been submitted for a degree or any other qualification at this University or any other institution, this has been clearly stated;

• where I have consulted the published work of others, this is always clearly attributed;

• where I have quoted from the work of others, the source is always given. With the exception of such quotations, this thesis is entirely my own work;

• I have acknowledged all main sources of help;

• where the thesis is based on work done by myself jointly with others, I have made clear exactly what was done by others and what I have contributed myself;

• parts of this work have been published as the journal papers and conference contributions listed in Appendix E.

Signed: _____

Date: _____

Acknowledgements

I would like to thank my Supervisors Prof. Nikolay Zheludev and Prof. Kevin MacDonald. Professor Zheludev as leading researcher of the field has provided me with inspiration and guidance throughout my PhD studies, while he gave me the chance to deal with several interesting topics during my PhD. Prof. MacDonald was always been helpful in every aspect of my research.

I would like to thank all my collaborators/mentors, without whom some of my work would be impossible. Especially, Dr. Jun-Yu Ou for patiently assisting with optomechanical measurements and useful advices related with focused ion beam and generally for his assistance in the labs. Dr. Behrad Gholipour in the phase change metamaterial experiments, made the time in the lab to pass quite exciting, while his enthusiasm had many times motivate me to work more intensively. I would like also to thank Dr. Venkatram Nalla for his excellent collaboration related with the diamond metamaterial project, even though a huge distance separated us we always had an excellent collaboration.

I would like to thank all other members of the Nanophotonics & Metamaterials group not only for their help in my research, but also for the great time together. Especially, I had great time with Dr. Pablo Cencillo Abad as we shared many common interests and had good time in the office.

I would like to thank Neil Sessions and Dr. Alexander Buchnev for the training in cleanroom and Focused Ion Beam, respectively.

Finally yet importantly, I would like to thank all those that made my stay in a foreign country possible. Maria-Eleni Rizou for her partnership as well as for the valuable help in electrical measurements. I would like to thank my family, Giannis, Stella and Maria for their everyday support, who made my PhD studies in a foreign country possible.

Chapter 1

Introduction

Recent developments in photonics are focused in several directions, one important theme are reconfigurable nanophotonic technologies, with interest to control optical signals in the nano-scale, in high speed, low energy consumption and low fabrication costs. When the above requirements are fulfilled, nanostructured photonic technologies will cover everyday life with huge impact on the welfare and development of the public economy. Up to now, many commercial photonic applications have been realized with most profound development those in the field of optical fibre networks, which have boost the speed of internet. However when comes the time to manipulate and process the daily, increasingly signals, electronic devices are more widely used than nano-photonic counterparts.

Although electronics is a well-established technology, they have certain limitations, especially on the speed that they can operate, and this is clear when you try to manipulate signals in the GHz range, at these speeds fundamental operations of telecommunication networks start to lack from efficiency and can become extremely energy consuming and bulky. Alternative, if we take as an example how optical fibres have widely replace copper wires in order to transfer data, one might think that nanophotonic counterparts, should eventually replace the electronic components. Along my Thesis I will mainly describe methods and demonstrate devices which have the potential to replace electronic devices and provide reconfigurable functionalities of all-optical and electro-optical data control at the nano-scale.

1.1 Dielectric Nanophotonic Metamaterials

The aim of nanophotonics is to bring fundamental concepts of photonics such as emission, waveguiding, imaging, energy harvesting, data processing among others into the nano-scale. In this goal, the development of nanofabrication has boosted the potential of this technology, in cooperation with computational methods, which have assisted to understand or even predict novel nanophotonic applications.

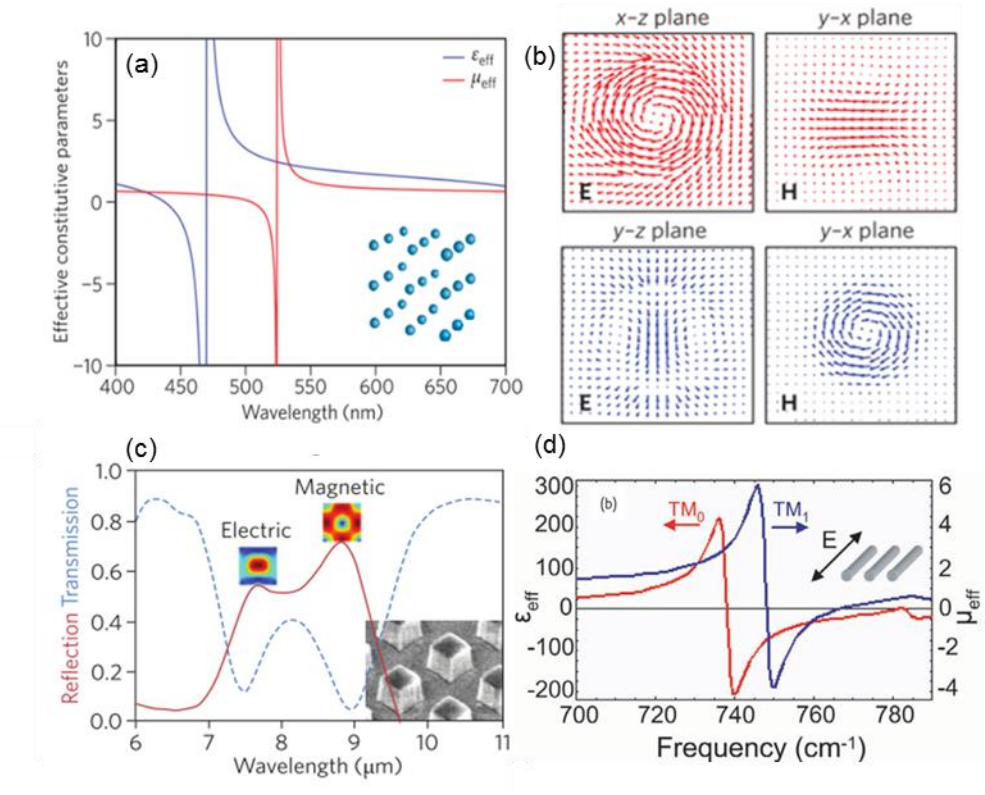

Figure 1.1 Effective parameters and collective response from high-index optical resonator arrays. (a) The effective permittivity (ε_{eff}) and permeability (μ_{eff}) of a 3D array of spherical high-index resonators (inset) with $\varepsilon = 12$, r = 150nm. [7] (b) The magnetic (red) and electric (blue) resonances correspond to an effective negative magnetic permeability and an effective negative dielectric permittivity. [7] (c) In the vicinity of electric or magnetic resonances, a 2D array of high-index tellurium resonators (inset; cube dimension = 1.45 μm) behaves like an electric or magnetic mirror, respectively. [34] (d) Calculated effective permittivity and permeability for a normal incidence TE illuminated array of infinitely long SiC rods. [9]

In order to harvest these benefits a good understanding of the underlying physics is needed. Mie scattering initiated the research on dielectric nanophotonic metamaterials. The problem of the diffraction of light by small particles of spherical shape has been considered, from the point of view of the electro-magnetic theory of light, by Lord Rayleigh, in 1881. In the case of a high index dielectric particle e.g. a sphere, with size comparable or smaller than the incident light, Mie resonances appear due to the excitation of electric displacement currents within the particles, lead to the formation of magnetic and/or dielectric dipoles, quadrapoles etc. [1]–[5] These resonances eventually have been used to create peculiar conditions such as high electric field confinement, magnetic light, forward and/or backward scattering. [6] Figure 1.1 shows calculated effective parameters and collective response from high-index optical resonator arrays, [7] such as GeTe cubes [8] and SiC nanowires. [9] In Shemouskina's paper [10] proposed and experimentally demonstrated that the coupling among periodic arranged dielectric particles could result in microwave narrow bandpass filters, realizing the first all-dielectric metamaterial. Later on other works extend this behaviour in infrared and visible regimes. [8], [9], [11], [12]

Research on metamaterials started due to the demand to control light properties with artificially nanostructured media. Initial work on metamaterials started from a theoretical paper from Veselego, [13] in that theoretical work it was suggested that exotic materials with both negative permittivity ε and permeability μ existed, this should lead to peculiar effects in wave optics. These conditions however are impossible to occur in natural media. Pendry's theoretical paper and later Smith's group managed to demonstrate that these exotic properties are possible in the microwave regime and demonstrate microwave devices with μ, ε negative and as a result, negative refractive index. [14], [15] For the next few years, metamaterials research was devoted to the understanding of this scheme, how effective parameters (μ, ε) can occur after subwavelength design, with special interest triggered by the opportunity to achieve novel optical properties, some with no analog in naturally available materials. Despite the fact that researchers in the field of optics had started to realize that light could be concentrated in small volumes and channeled using subwavelength metallic structures since the late 90's, [16], [17] the first experimental nanostructured photonic metamaterials were demonstrated a decade later. Extraordinary transmission, [18] artificial magnetism and negative refraction, [19] invisible metal, [20] magnetic mirror, [21] asymmetric transmission [22] and filtering [23] were just few examples of the new phenomena emerging from the development of artificially structured matter. This revolution in optics result in miniaturized photonic circuits with length scales much smaller than those currently achieved. As a result plasmonic metals were established as the most prominent building blocks for photonic metamaterials. Despite these achievements, photonic metamaterials still could not be used in many practical applications because of their limitations associated with energy dissipation in the metals used to construct them.

Alternatives are being sought in oxides and nitrides [24], [25] and in high-index dielectrics delivering resonant metamaterial properties with negligible losses. [26] Dielectric metamaterials benefit from the exclusion of joule heating, as a result many times higher q-factors have been exhibited so far [26], [27] in comparison with plasmonic counterparts. Optical resonances can be excited in dielectric materials, due to Mie modes excited by high index dielectrics. Since the 1st experimental demonstration in microwave regime of an all-dielectric metamaterial, [10] the Mie resonances of dielectric particles have been proposed as a platform for the engineering of magnetic resonances [3], [9], [11], [28]–[30], and on this basis magnetic responses have been experimentally realized in metamaterials and photonic crystals fabricated from high permittivity dielectrics such as titanium dioxide, germanium and silicon, at microwave and terahertz frequencies [31]–[33] , in the infrared/optical range [8], [34]–[36]. Whilst the field of dielectric metamaterials keep evolving new functionalities are emerging

such as chirality [27], zero-index response [37], phase control, [38], [39] Huygen's sources, [40] lenses [41], [42] and 2nd and/or 3rd harmonic generation [43], [44] as it can be seen in Figure 1.2.

While in plasmonic structures the electromagnetic fields are typically concentrated in the surrounding medium, in dielectric Mie-like resonators, the fields are normally concentrated

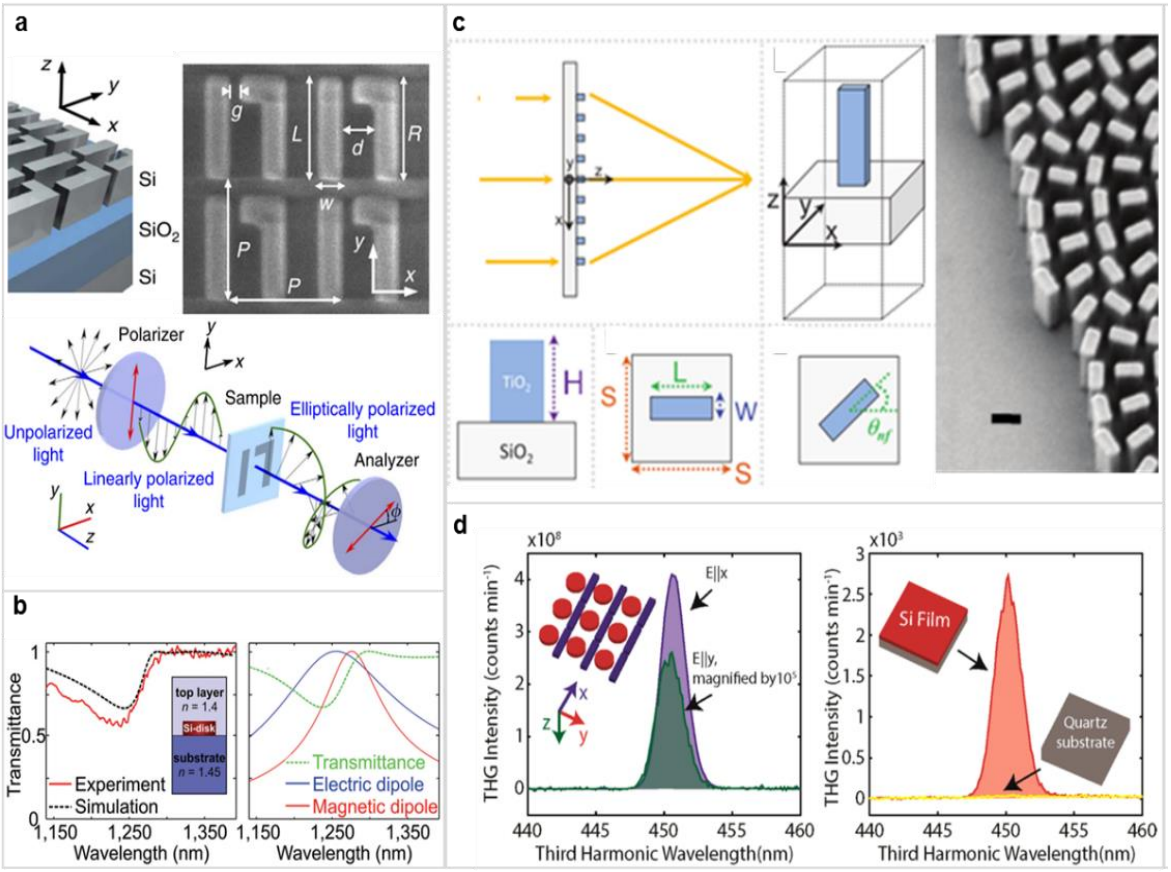

Figure 1.2 Functional Dielectric Metamaterials. (a) Chiral metamaterials made out of periodic Silicon/SiO2 bulding blocks, that lack from inversion symmetry. [27] (b) Experimental implementation of a Huygens metasurface made out of periodic array of silicon nano-pillars, after appropriate design of the aspect ratio: height/diameter the spatial overlap of an electric and magnetic dipole lead to forward scattering only from the metamaterial array. [40](c) A dielectric meta-lense formed by TiO_2 nano-bricks operate at visible wavelengths, scale bar 300nm. [42] (d) A nonlinear dielectric metamaterial enhances the inherit 3rd harmonic generation of an unstructured silicon film. [43]

within the volume of the resonator, resulting in fundamentally different behaviour from plasmonic counterparts. First consequence of this, is that some modes of dielectric resonators are insensitive to imperfections in the surrounding, making them tolerant to fabrication imperfections [45], but other are not, while in plasmonics high fabrication precision is needed at the interfaces where the field is focused. Field enhancement is lower than in plasmonic structures and the electric field hotspots can be controlled to lie either inside or outside the resonator in the near-field environment, as a result dielectric metamaterials can become either structurally or phase change reconfigurable after appropriate design. Depending on the design

of the metamaterial unit cell, different array size is needed to achieve optical resonance and furthermore this leads to sensitivity of the structure to the angle of light incident. As stated in [26] an array of 100x100 meta-molecules is needed to obtain collective behaviour while in [46] only an array of 5x5 unit cells is enough to achieve the collective behaviour and the quality factor of those resonances seems independent to the array size, this effect have been explicitly explained for plasmonic counterparts in [47]. How to couple of the incident light to the dielectric metamaterial is another issue, which has to be solved. For example in [26] an NA of 0.025 is used in order to achieve incident light beam angle close to normal, however recent publications reveals that is not always the case as in [46] where NA of 0.40 is enough to achieve q-factors of 600.

Apart from the design of the dielectric structures, fabrication methods and materials used vary depending on the application. Standard lithographic approaches, such as electron-beam lithography or focused ion beam milling, (see Appendix A), have been used to create periodic subwavelength arrays of dielectric nano-resonators. Beyond those techniques, dielectric nano-particles are fabricated using chemical methods leading to a broad distribution of particle sizes. [48] In contrast, femtosecond laser ablation of a silicon wafer produces silicon nanoparticles and simultaneously induces a transfer of these nanoparticles to a nearby glass substrate. [3]

The most commonly used material up to know used to develop dielectric metamaterials is Silicon, [49]. However other materials with low refractive index such as Silicon Nitride, SiN [50], Titanium Dioxide, TiO_2 [51], [52] or much higher refractive index like Germanium, Ge [46] and Tellurium, Te have been used. [8] These dielectric nanostructures are considered more preferable than metallic nano-structures, due to the fact that are made out of materials, which are compatible with CMOs technologies. Continuous efforts are devoted to the discovery of novel, functional, dielectric materials like topological insulators, [53] organometallic perovskites [54] and chalcogenide glasses. [55]

Similar with All-Dielectric metamaterials, Photonic Crystals support optical resonances. They are both made of similar materials and periodic nanostructures. So which is the difference between these two categories of nanophotonics structures. In photonic crystals optical properties can be described by combing Maxwell equations with Bloch's Theorem. The dielectric function of a photonic crystal is a periodic function defined by the periodic pattern of the crystal. The Hamiltonian that describes this eigenvalue problem leads to permitted and forbidden photonic bands. These photonic band gaps are result of the destructive/ constructive interference among scattered (partially reflected) waves.

Under resonant conditions (PhBGs), neighboring unit cells coupling is necessary for the Bragg scattering. So it is normal to consider effective refractive index only for certain directions. On the other hand, all-dielectric metamaterials rely on different type of resonances. The energy of the field at the resonance is concentrated in a small fraction of the unit cell volume. The coupling between metamolecules is neglible, as a result an effective medium frequency dependent is appropriate to apply. One of the basic ways of this effective theory is the retrieval method of characterizing the metamaterials effective permittivity and permeability.

1.2 Nanophotonic Reconfigurable Technologies

Reconfigurable nanophotonic technologies are named the general family of nano-devices, which demonstrate "optical properties on demand". [56] Physical mechanisms like thermo-optic tuning, modulation of free carrier concentration in semiconductors, optical Kerr effect,

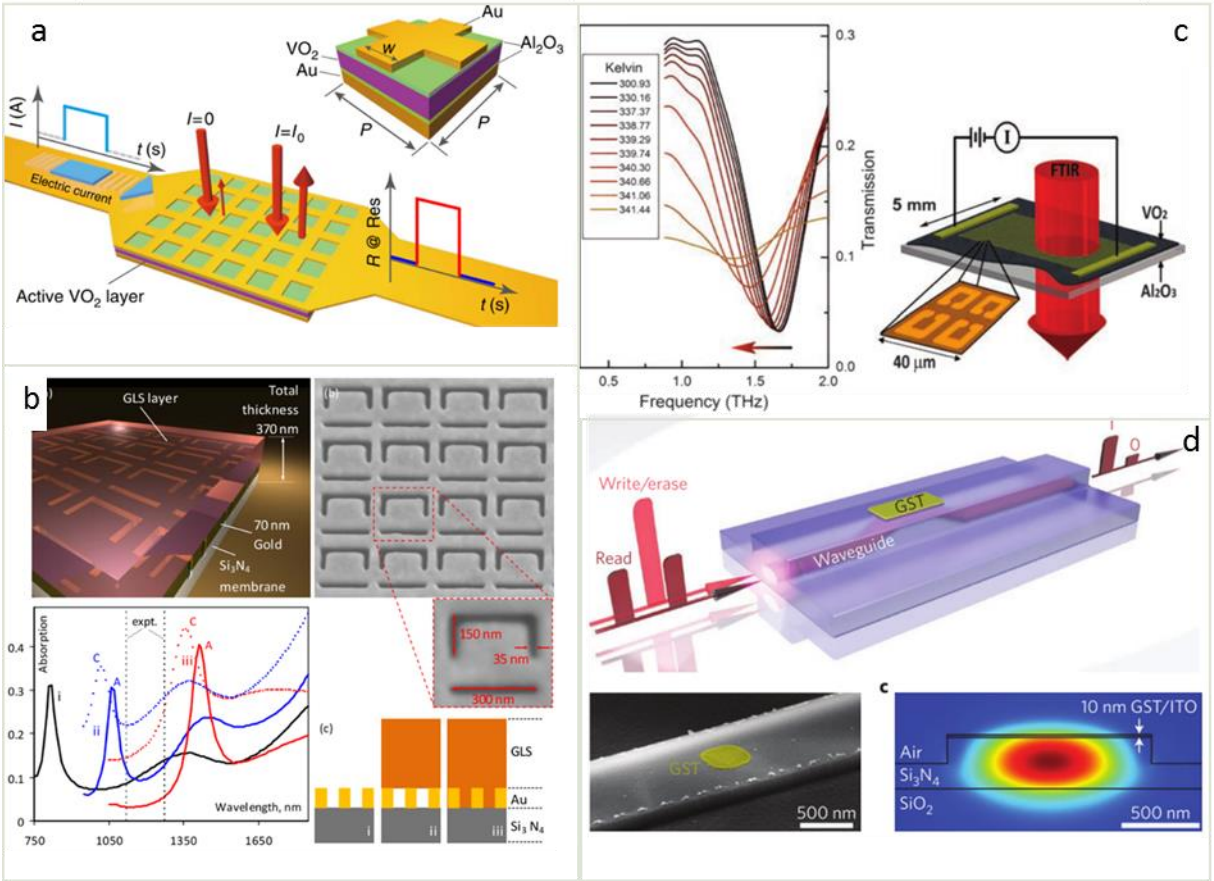

Figure 1.3 Phase change based reconfigurable photonic devices. (a) Schematic sketch of an electrically switchable nanostructure made out of Au-VO_2-Au micro-structures, operating at mid-infrared. [182] (b) similar electrically switchable device based on GLS-Au-Silicon Nitride nano-structure operating in visible-NIR regime. [113] (c) thermally actuated metasurface based on Au-VO_2-Saphire structure. [73] d, side view of a Si_3N_4 waveguide resonator employing a GST switch. Bottom left SEM image and bottom right simulated response of electric near field. No capping layer is used and the actuation process is based on optical pulses. [61]

electro-optic effects such as, pockels effect or electro-absorption (Frantz-Keldish) are some of the most commonly used techniques to control optical behavior of nanophotonic structures and have been used to develop all-optical and electro-optical modulators. [57], [58] Furthermore, the development of novel materials incorporated in schemes like waveguides, photonic crystals or even metamaterials, harvest the near field enchancement to achieve even stronger responses [59]–[63]. As the materials science develops new functional materials appear as strong candidates for optical or electrical reconfiguration. Graphene with optically/electrically controllable energy band gap [64]–[66] and more generally two dimensional materials[67], liquid crystals [68], [69] with distinct refractive indexes for different orientation of the molecules or photoresponsive polymers [70], [71], phase change materials like gallium, [72] vanadium dioxide VO_2, [73] and chalcogenide glasses, [74] have fueled the field of

nanophotonic reconfigurable technologies. Phase-change materials can provide a way to shrink optical switching devices down to the nanoscale. They form devices smaller than (or comparable in size to) the carrier wavelength of the signals. This is of great importance in nanophotonics and creates conditions, which are unfeasible for electronic circuits. [75] Large

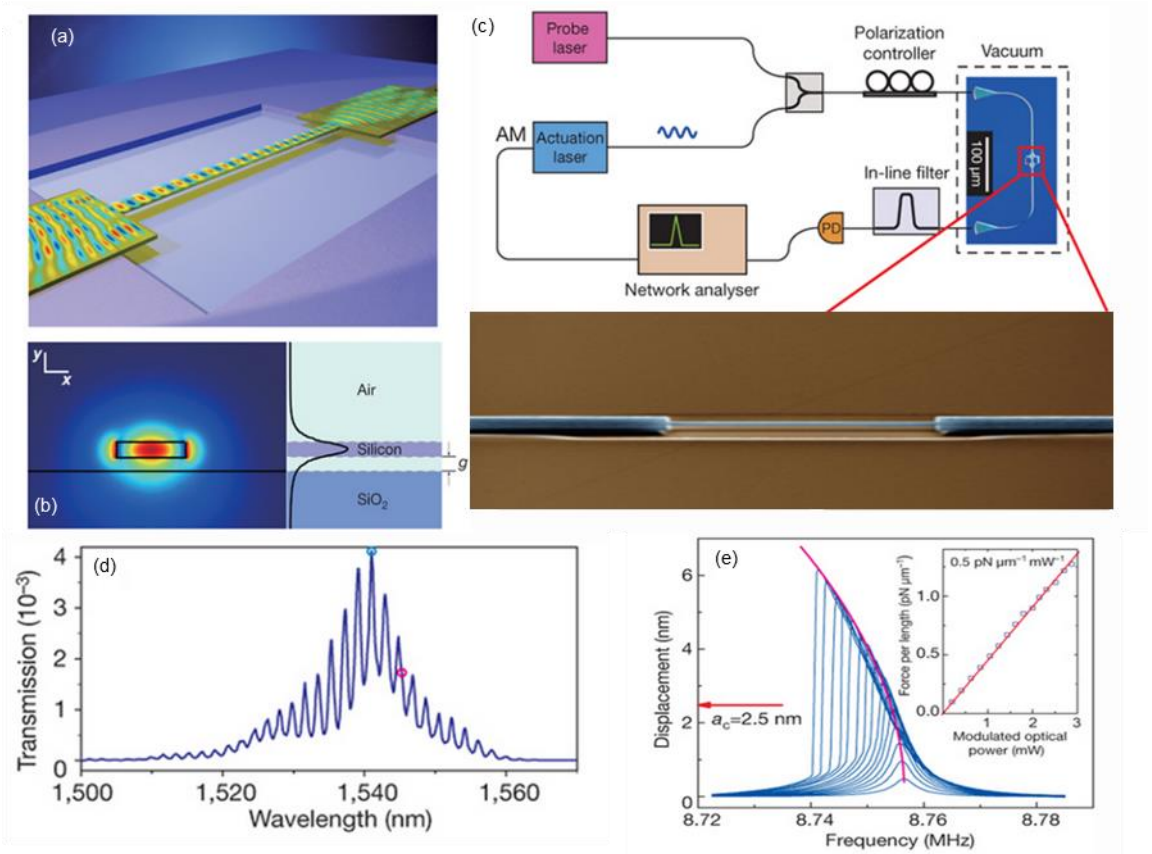

Figure 1.4 Reconfigurable photonic dielectric waveguides based on optical forces. (a) Schematic sketch of a free-standing Si waveguide beam. (b) Left simulated response of the Electric component of the optical field. Right, the intensity of electric field across the waveguide, light is highly confined in the high-index material, while evanescent waves are coupled to the SiO_2 substrate (c) The experimental set-up used to detect optical force actuation of a free-standing, 10-micron Silicon beam. Pressure on the chamber is 10^{-6} mbar (d) The typical transmission spectrum of the device, showing interference fringes of the internal Fabry–Perot interferometer formed by the input and output couplers. The wavelengths of the actuation and probe light are marked with the blue and magenta markers, respectively. (e) Resonance response curves of a 10-microm-long waveguide beam at varying modulation levels of the actuation light. When the vibration amplitude exceeds the critical amplitude ac, the response shows a strong softening nonlinearity. The critical amplitude of 2.5nm, determined from the backbone curve (magenta line), agrees well with the theoretical value of 2.2 nm. Inset, the vibration amplitude versus modulated optical power on the device shows a linear response. [78]

non-volatile change in optical properties have been demonstrated, however the integration of these materials with metals limits the total number of transition cycles that can be achieved. This is due to degradation of metals. Capping layers have been used to address this issue, Metal free phase change nano-devices are still of great interest, (see Figure 1.3.). Other effects are based on concepts such as nano-mechanical motion of optically resonant structures. [76] At the nanoscale, elastic forces are comparable to electromagnetic forces. As a result, effective optical

parameters of the nanodevices can be controlled externally to provide reconfigurable response. This motion can be triggered in several ways to provide modulation of incident light by thermal, electrical, magnetical, mechanical or even optical methods. [77] In optomechanical systems like those presented in [78], [79] a free-standing nano-beam made out of a high-index dielectric material is excited optically by in-plane light. A pump-probe measurement is conducted over a broadband wavelength range. As illustrated in Figure 1.4 two light beams are coupled through a WDM in the waveguide, and after the device a bandpass filter blocks the pump. Probe light is converted into an electrical signal by a photodetector and is recorded as a vector network analyzer, VNA. The other port of the VNA, is used to drive the pump laser. The excited optical force can move the nano-beams on the scale of a few nm, which is enough to cause change of

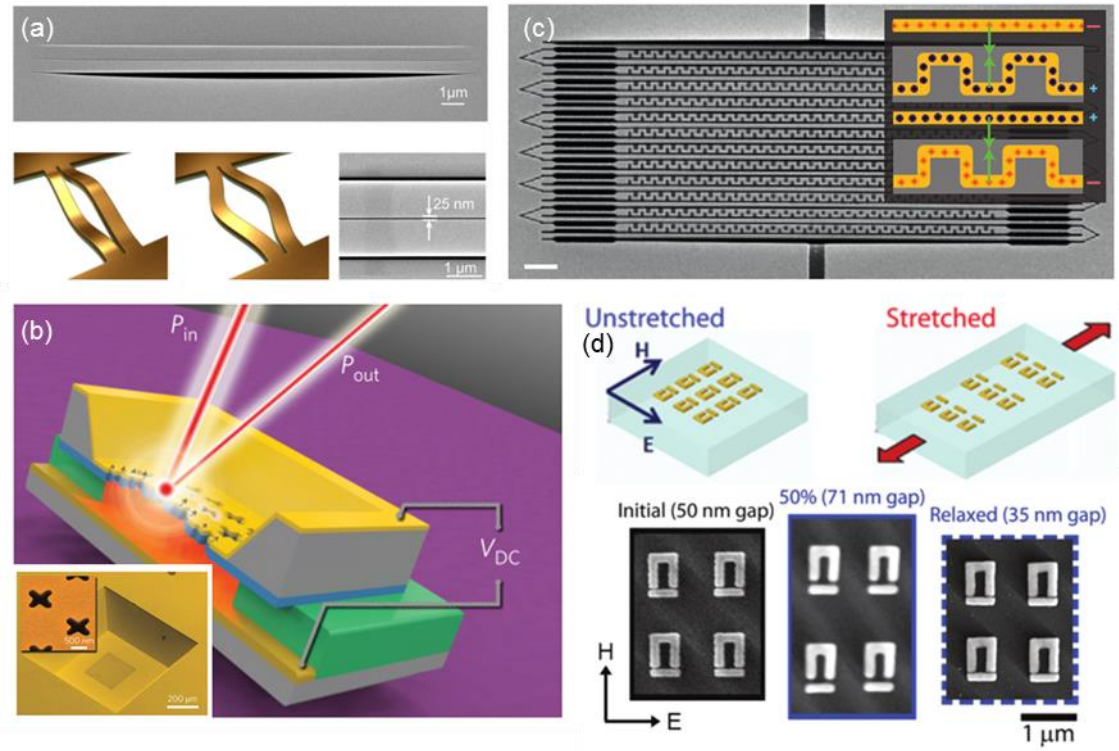

Figure 1.5 Plasmonic nano-mechanical light modulators. (a) Scanning electron micrograph (incident angle 52°) of the double bridge structure after fabrication. The two-bridge structure is freestanding and lifted above the surrounding membrane due to mechanical stress in the latter. Cartoon of the antisymmetric out- of-plane and in-plane mechanical mode of the double bridge structure. Scanning electron micrograph (incident angle 0°) of the center part of the double bridge, showing the 25-nm-wide central gap.[83] [97] (b) Schematic of the metamaterial absorber with a mechanically compliant bilayer (Au (25 nm)/SiN (100 nm)) membrane component decorated with a nanoantenna array. The structure simultaneously supports optical Fano and mechanical resonances, which are coupled via thermomechanical forces induced by absorption. The absorber gap can be electrostatically tuned with an applied voltage. Inset, the false-colour scanning electron microscopy (SEM) image of the fabricated cross-shaped nanoslot (length (360 nm)/width (150 nm)) antenna array (period 800 nm) that covers an area of 250 μm by 250 μm at the centre of the 500 μm by 500 μm membrane. (c) An electro-optical modulator: metadevice driven by electrostatic forces (green arrows) between oppositely charged nanowires (+, −). (d) Schematic of the substrate prior to stretching with Au split ring resonators attached. The ESEM images of an array of 2 × 2 SRR-bar unit cells initially, relaxed, and for 50% strain. The measured gap distances from ESEM images are shown in parentheses.[183]

the effective refractive index of these waveguides by a few percent. The modulation of light is only a small percentage of the incident light, which make this technology unsuitable for commercial all-optical modulators.

An alternative technique to achieve structurally reconfigurable devices is based on plasmonic resonances achieved in free-standing, flexible nanomembranes or in flexible substrates. Due to the strong coupling between plasmonic resonators, any displacement between the plasmonic meta-molecules can lead to change in the effective index of the device. The main advantage of this scheme over the dielectric photonic crystals or waveguides is that light is confined in deeply subwavelength regions. As a result the interaction length of those devices is limited to the thickness of the plasmonic surface, e.g. around 100nm. The optical modulation of these devices are on the scale of a few percent, while there is also the ability for fast dynamical control of the optical response. This speed is determined from the size of the supporting nanowires or nanomembranes. The corresponding frequency is at the level of a few MHz. However for shorter nanowires with appropriate design can reach the GHz frequencies. Figure 1.5 presents several experimental examples of this concept.

1.3 Dielectric Reconfigurable Metamaterials

Dielectric reconfigurable metamaterials outperform plasmonic counterparts in many aspects. Joule losses are a-priori limited, they are made from CMOS compatible materials, they can operate in transmission mode and recently have been shown to be an adequate platform to achieve optical reconfigurable properties (as illustrated in Figure 1.6). A nano-difraction grating can support guided modes, and support certain reflection peaks in the visible, and as a result give different colours for different periods and angle of incident light. Upon stretching the flexible substrate, colour can be actively controlled. [80] Another example, an array of silicon nano-disks embedded within a liquid crystal can provide reconfigurable response upon either heating or biasing. [81], [82] The modulation depth reported in these works is better than plasmonic counterparts but modulation speeds are still low due to the limited modulation speed of liquid crystals, mechanical reconfiguration of the flexible substrate still limits the modulation frequencies up to few a KHz. So the reconfigurable response of dielectric

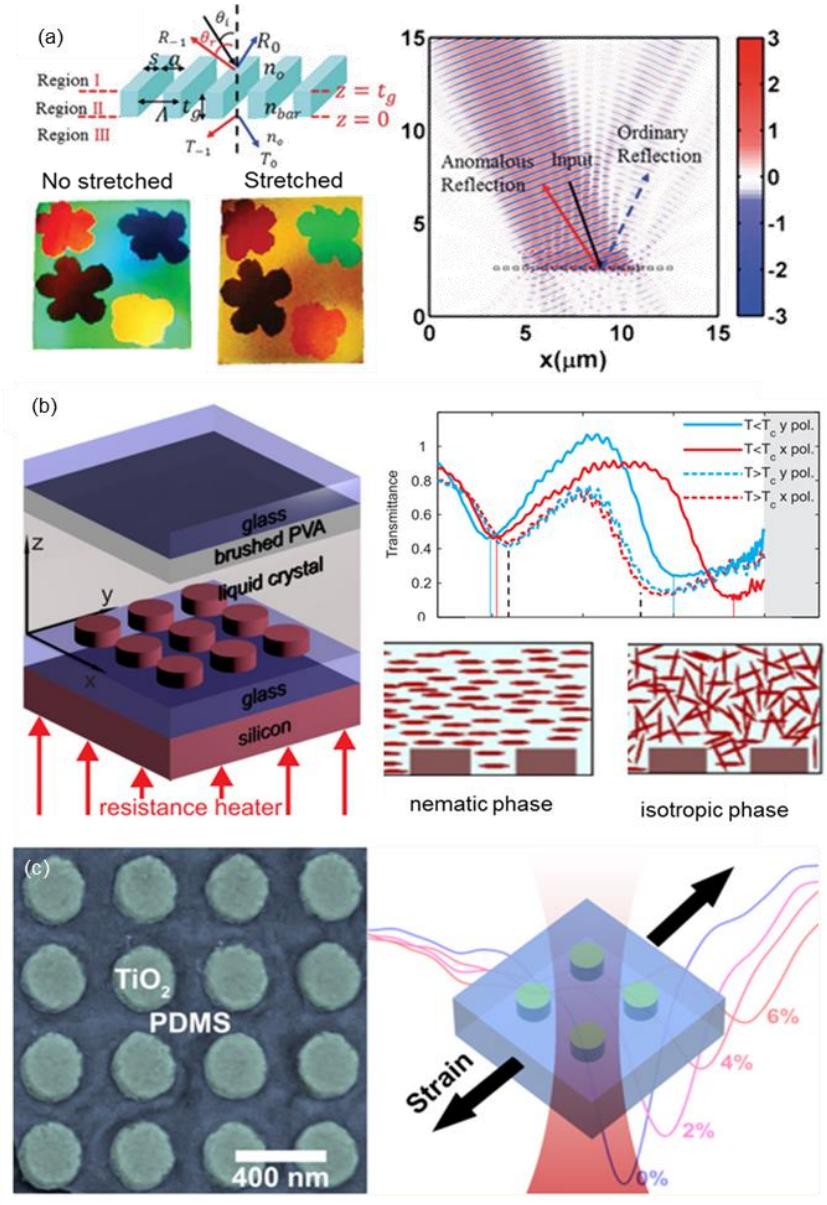

Figure 1.6 Dielectric Reconfigurable metamaterials. (a) Left, schematic of a one-dimensional high-contrast nano-grating. The optical properties are determined by period Λ, thickness t_g, and duty cycle η= s/Λ, where s is the width of the high-index bar. In the two-order diffraction regime, the incident light is diffracted into four possible orders: R_{-1}, R_0, T_{-1}, and T_0. Right, anomalous reflection effect for the proposed device with 180 nm thickness and 32° incidence angle. [80] (b). Left, Schematic of the silicon nanodisk metasurface integrated into an LC cell. The silicon nanodisk sample is immersed in the LC, and the cell is heated by a resistor. Right, Sketch of the (idealized) arrangement of the LC molecules in the nematic and the isotropic phase, respectively, while transmission spectra are ploted for heted and non0heated samples in near infrared. [82] (c) Left, TiO_2 resonators embedded in PDMS imaged with a scanning electron microscope and represented in false color, where blue indicates PDMS and green TiO_2. Right, polarization-dependent transmission spectra of the metasurfaces with increasing applied strain. [52]

metamaterials is an open field with the demand of faster modulation speeds and large bandwidths as well as the eventual commercialization of those devices into fiber-integrated systems. Recent published works have shown more complex application than simple active modulation of the transmission/reflection spectrum. For example [55] dynamic focussing of light was demonstrated using phase change Fresnel and super-oscillatory lenses.

1.4 Thesis overview

Dielectric metamaterials have the potential to combine metamaterials with industrial fabrication techniques developed in silicon nano-electronics. This thesis presents a study of potential for reconfigurable dielectric metamaterials through three schemes: nanomechanical, phase change and coherent control mechanisms. The research done has led to intriguing results, such 1) **the demonstration of the first opto-mechanical nonlinear dielectric metamaterial operating at 152MHz**, which is the highest modulation frequency presented to date. 2) The experimental demonstration of the first nanomechanical electro-optical switch made out of dielectric materials, actuated by few volts. 3) The demonstration of chalcogenides glasses, in particular $G_2S_2T_5$, **as optically reconfigurable material (optical switch) with strong reflection and transmission contrasts up to 5:1 and 3:1**, **respectively between amorphous and crystalline states**. This is explained by the fact that $G_2S_2T_5$ is a high-index dielectric at near infrared regime and plasmonic in visible. 4) **The report of the first Diamond nano-membrane metamaterial, which operates as coherent absorber of light pulses as short as 6fs at visible-NIR wavelengths.**

The content of this thesis is summarized as follows:

In the 1st chapter a short review is considered upon metamaterials and especially the progress of dielectric metamaterials the previous years. Next, I present how reconfigurable technologies have led to technological breakthroughs and how plasmonics offer a solution on this direction. However, I emphasize the fact that dielectrics reconfigurable metamaterials could lead to eventual commercialization of metamaterials technology as they can be developed with CMOS compatibles methods and demonstrate stronger performance, e.g.: modulation depth, etc.

In the 2nd chapter, structurally reconfigurable metamaterials actuated by optical forces are presented. First, I report that resonant localized electromagnetic modes in a nanostructured silicon membrane can provide an all-dielectric metamaterial, which operates as a nonlinear medium at optical telecommunications wavelengths. I show that such metamaterials provide extremely large optomechanical nonlinearities, operating at intensities of only a few μW per unit cell and modulation frequencies as high as 152 MHz, thereby offering a path to fast, compact and energy efficient all-optical metadevices.

In the 3rd chapter, experimental demonstration of a free-standing, all-dielectric, nano-mechanically reconfigurable photonic metasurface actuated by electrostatic forces is reported. The subwavelength-thickness device is manufactured by CMOS-compatible, high refractive

index and transparent conductive media (silicon and indium tin oxide) and applied biases of only a few volts, to deliver reversible optical changes approaching 10% in near-infrared and dynamic modulation of 7MHz. Last, is explained how those metamaterials can be evolve as fiber-coupled meta-devices, operating as fiber integrated electo-optical modulators.

In the 4th chapter, non-volatile, amorphous-crystalline transitions in the chalcogenide phase-change medium germanium antimony telluride (GST) are harnessed to realize optically-switchable, all-dielectric metamaterials. Nanostructured, subwavelength-thickness films of GST present high-quality resonances that are spectrally shifted by laser-induced structural transitions, providing reflectivity and transmission switching contrast ratios of up to 5:1 (7 dB) at visible/near-infrared wavelengths selected by design. At the same time, the GST nano-gratings at the visible regime can operate as plasmonic materials with colour tunability across this regime and strong contrast in optical properties as well.

In the 5th chapter, the first experimental demonstration of coherent light-by-light modulation at few-optical-cycle (6 fs) pulse durations, enabled by a nanostructured polycrystalline diamond broadband metasurface absorber only 170 nm thick is present. I study the optical properties of diamond metamaterials for first time and I present how broadband absorption in diamond metamaterials is feasible.

In the last chapter an outlook work is presented together with a future work.

An appendix is included in the end to briefly explain main experimental and computational techniques used for the completion of this thesis.

Chapter 2

Reconfigurable Nano-membrane Dielectric Metamaterials.

The ultimate goal of nanophotonics — that is, to create devices smaller than or comparable in size to the carrier wavelength of the signals they handle, a relationship of proportions that is easily achieved in most electronic circuits, are provided by nanomechanical devices that take advantage of the changing balance of forces at the nanoscale. As the physical dimensions of a system decreases, the electromagnetic forces between constituent elements grow, as illustrated by the repulsive force between electrons as their separation diminishes. In contrast, elastic forces, such as the force restoring a deformed beam, decrease with size. At the sub-micrometre dimensions of the meta-molecules in photonic metamaterials, electromagnetic Coulomb, Lorentz and Ampère forces compete with elastic forces and can thus be used to reconfigure the shape of individual meta-molecules or to change their mutual arrangement. The nanoscale metamaterial building blocks can be moved fast, potentially offering modulation at gigahertz frequencies. Such structures can also be driven thermo-elastically or by light, through optical forces arising within illuminated meta-molecules.

Elastic structured nano-membranes are the ideal platform for such nanomechanical reconfigurable metamaterials. This new high-throughput and silicon-compatible technology benefits from related advances in nano-optomechanics, which have led to the demonstration of thermally driven plasmonic nanomechanical oscillators and resonators[83], [84]. Nanomechanical metamaterials are being developed alongside other approaches for creating nonlinear, tunable and switchable metamaterials from the microwave to the optical parts of the spectrum. The technology for growing high-quality free-standing nanomembranes, such as ultrathin films of silicon nitride [85], silicon [86] and diamond [87], that are supported by bulk semiconductor frames is well established. Individual membranes, both polycrystalline or nearly single crystal, typically have thicknesses ranging from a few tens of nanometres to one micrometre, with overall sizes up to a few square millimetres.

Elements of reconfigurable metamaterials can oſten be represented as nanowires. At the nanoscale, electromagnetic forces acting on such nanowires are comparable with elastic forces

of the supporting structure and therefore can be used to reconfigure metamaterials. Even small mutual motion of the elements of the metamaterial array can create substantial changes in its interaction with light and its optical properties (see Figure 2.1). For simplicity, let us consider two cylindrical nanowires of diameter D spaced by a centre-to-centre distance d and evaluate forces acting on a segment of nanowire of length L.

By illuminating nanowires with monochromatic light, optical force excitation can happen. Nanowires that have a length L of approximately half of the wavelength of incident radiation act as resonant antennas for light. Light-induced oscillating dipoles in a pair of parallel nanowires will repel with time-averaged optical force F, which is proportional to the incident light intensity P, if the radiation is polarized with the electric field E parallel to the nanowires and the optical wavevector k is directed perpendicular to the plane defined by them. When such gold plasmonic nanowires of diameter D = 100 nm, length L = 500 nm and spacing d = 300

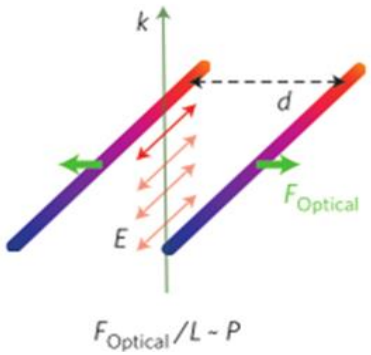

Figure 2.1 Optical force excitation under monochromatic beam illumination. Near field of oscillating dipoles lead to mutual repulsion of the pair of golden nanowires. Elastic forces remain constant while optical forces are proportional to the intensity of the input light beam.

nm are illuminated by light with wavelength λ = 925 nm and intensity P = 1 mW μm^{-2}, the repelling optical force between them is about 1.5 pN. This is calculated with the usage of Maxwell stress tensor in a Comsol model, with more details explained in page 25 and 26.

Optical force excitation has been an intense research field the last few year with several theoretical publication related either with plasmonic or all-dielectric metamaterials. [88]–[91] However, there is a power limit that these devices can sustain, this fact set dielectric metamaterials as a better candidate for stronger optomechanical forces in comparison with plasmonic counterparts. [77]

2.1. Free-standing Dielectric Nano-membrane Metamaterials

The all-dielectric metamaterial designs experimentally implemented to date are ubiquitously 'positive' structures based on assemblies of discrete nanoparticles/rods/rings supported by transparent low-index substrates [8], [26], [27], [36], [37], [41], [69], [92]–[95], engineered to present resonant responses based typically on (coupled) Mie/cavity modes. In this work, I have developed and experimentally demonstrated free-standing all-dielectric photonic metamaterials based on 'negative' slot patterns in continuous nano-membranes of Silicon Nitride and poly-crystalline Silicon. Silicon Nitride membranes have been employed previously as flexible and ultrathin substrates for thermo/electro-mechanically reconfigurable and coherently controlled photonic metamaterials [96]–[98], but I show here that as high-index, low-loss media they may serve as a metamaterial platform in their own right.

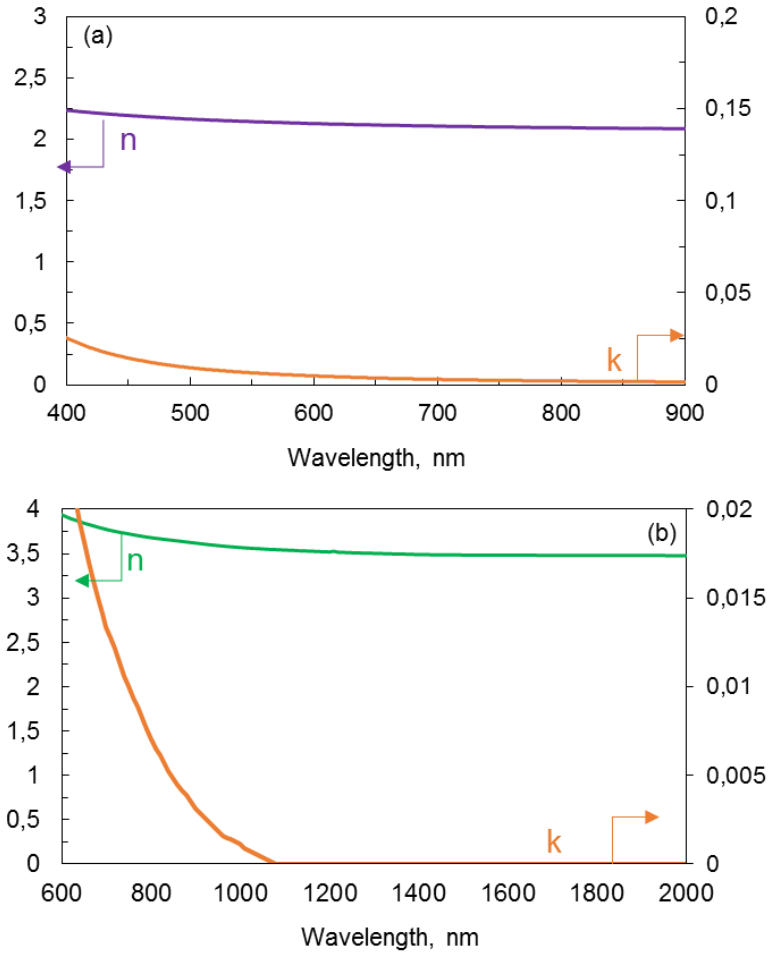

Figure 2.2 Refractive Index and Extinction ratio of Silicon Nitride and Silicon nanomembranes. (a) Silicon Nitride typical ellipsometry spectra in NIR regime. Losses become negligible for wavelengths longer than 600nm (b) Silicon typical ellipsometry spectra in NIR regime. Losses become negligible for wavelengths longer than 1100nm. Thickness and stress of the films influence refractive index and extinction ratio, respectively.

Ellipsometry measurements of typically used silicon and silicon nitride membranes are presented in Figure 2.2. This is the first test to quantify if the materials' optical properties are appropriate to support dielectric optical resonances. As can be seen Silicon retains a refractive index around 3.5 with negligible losses for wavelengths longer than 1100nm while Silicon Nitride have been lossless even from shorter wavelengths, however with a lower refractive index, close to 2. Samples are fabricated in commercially sourced 100nm thin membranes via FIB milling, see Appendix A. The metamaterials typically comprise either square arrays of micron scale unit cell slot features such as the ⊓ shape illustrated in Figure 2.3 or subwavelength periodic nanowires as in Figure 2.4 (in a 100 nm SiN membrane).

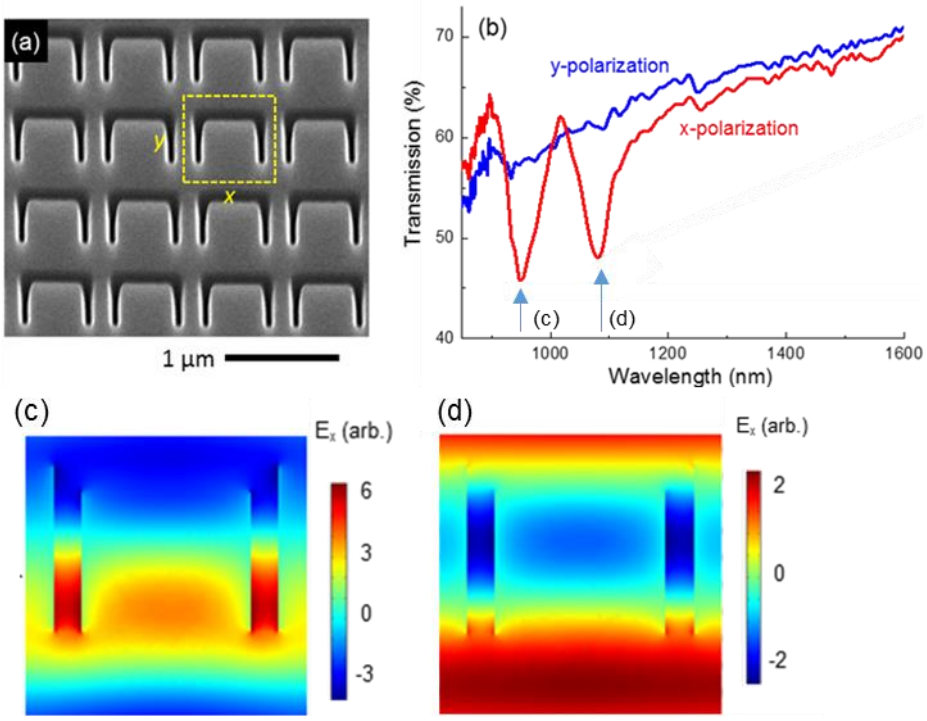

Figure 2.3 Free-standing silicon nitride membrane resonant metasurface. (a) scanning electron microscope image of an array of silicon nitride, SiN membranes [thickness 100 nm, width slit 100nm]. Experimentally measured transmission spectra, for x- and y-polarized normally incident light, for the free-standing silicon nitride metasurface. (c,d) Computationally modelled distributions of the x component of electric field, E_x in the middle of the membrane at the indicated spectral positions.

High-quality resonances are observed in the transmission spectra for such structures at near-infrared (visible) wavelengths for normally incident light polarized parallel to the opening of the ⊓-slots (nano-wires), which may be tuned by design via the structural dimensions of the milled pattern see Figure 2.3, figure 2.4). For nanostructures like those in Figure 2.3 3D finite element numerical simulations reveal that the resonances relate to interactions between Fabry-

Perot and Mie modes excited within the dielectric structure, presenting the characteristic lineshape of a fano-type resonance, (more details are given in the next section). Manufacturing imperfections and inhomogeneities so far limit observed quality factors for the resonances to Q~60, but computational models indicate that in principle values several times higher than this are possible. At the same time as in [96]–[98] silicon nitride nanowires play the role of supporting beams, and the optical resonance provided by plasmonic metals, here it is shown

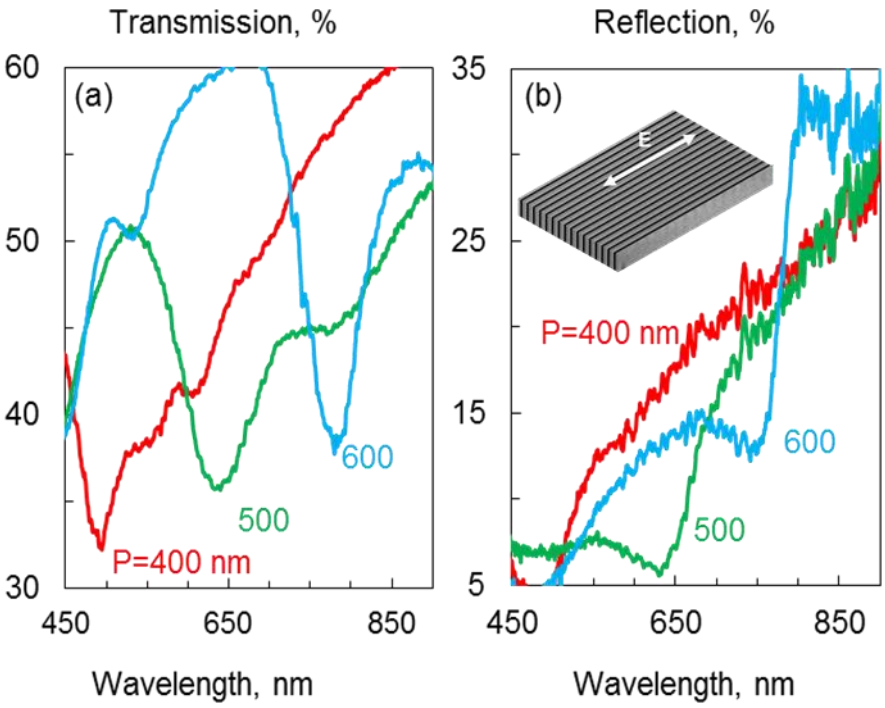

Figure 2.4 Free-standing silicon nitride membrane resonant nanogratings. Experimentally measured transmission (a) and reflection spectra (b), y-polarized normally incident light, for the free-standing silicon nitride metasurfaces, nano-gratings with periods P=400, 500 and 600nm as annotated [thickness 100 nm]. Groove size is kept constant at 100nm for every period.

that nano-gratings support guided resonances with Q~40, paving the way to engineer optical properties in the visible regime and suggests SiN as a (new) all-dielectric nano-membrane material platform.

Apart from SiN, polysilicon free-standing membranes with 100nm thickness have been tested after nanostructuring. The shape of the unit cell remains the pi shaped slot, and as it can be seen in Figure 2.5 that strong optical resonances are recorded at NIR wavelenghth with optical response defined by the nano-cantilevers length, L while pitch and other geometric features remain the same. These resonances could be used in sensing applications or in nonlinear responses via optomechanical coupling of the optical resonant mode with the vibrational modes of the nano-cantilevers in the range of few hundreds of MHz.

Under appropriate illumination, the optical forces generated in low-loss dielectric metamaterials such as these can be sufficient to deflect elements of the structure (e.g. the nano-cantilever within each cell (Fig. 2.4, 2.5 and 2.6). Each has a mass of order of hundreds of femtograms.

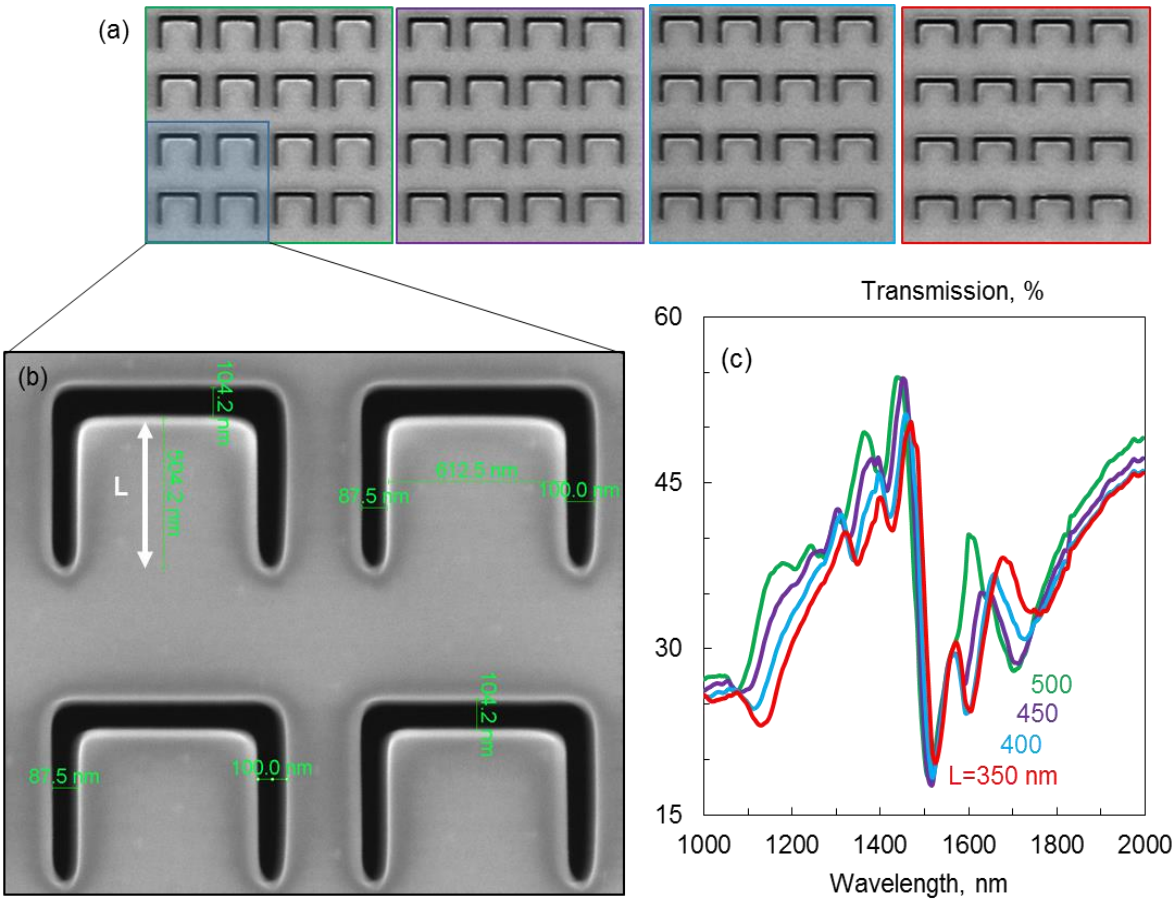

Figure 2.5 Free-standing silicon membrane resonant metasurface. (a) Scanning electron microscope image of part of a free-standing silicon membrane metasurfaces for several cantilevers length. (b) Zoom in image of a 2x2 array of Silicon nano-cantilevers with unit cell size of 1.05 μm × 1.05 μm; and thickness 100 nm. (c) Experimentally measured near –IR transmission resonance spectra for x-polarized light (vertical to the cantilever) normally incident on structures such as in panel (a), with varying nano-cantilever lengths L.

In fabricating a variety of Si and SiN membrane metamaterials, I have found that the equilibrium position of the nano-cantilevers depends sensitively on stress within the membranes (which can vary among nominally identical membranes and even across a single membrane) as well as the length/width of the cantilever arms and thickness of the membrane. Interestingly, I have established that varying the position and dimensions of a straight cut across the fixed end of a cantilever (a cut which would constitute the short arm of the classic asymmetric split ring metamaterial unit cell design; as illustrated in Fig. 2.6c) enables one to

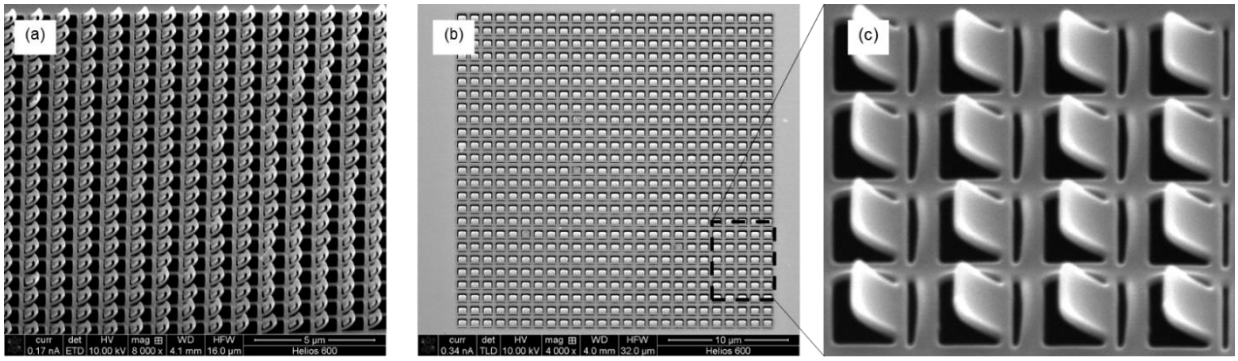

Figure 2.6 Control by design of nano-cantilevers tilt. (a) an array of tilted meanders, where internal stress of Silicon membranes deforms meta-molecules from their in plane position. (b) An array of ASR The presence/absence of an additional slot cut across the fixed end of each cantilever determines the extent to which it tilts out of plane under the action of stresses within the membrane. In-plane nano-cantilevers in a 100 nm thick poly-Si membrane (b) are uniformly tilted out of plane (c oblique view) with the addition of such a slot.

manipulate the degree of tilt in the equilibrium position of the cantilever. This technique could possibly enable the fabrication of 3d-nano-structures. 3D nanostructures have been recently reported in ref [99]. In that work ion-implantation induced stress, (while here appropriate cuts) result in tilted structures, (see Figure 2.6). Those tilted structures might lead to excite optical modes which are inaccessible in a planar 2D nanostructure.

Furthermore, I have continued developing the next generation all-dielectric metamaterial samples made out of bilayer (Silicon and Silicon nitride) dielectric membranes. The starting point is still commercially available Silicon membranes, RF sputter deposition method was used to create the second layer of a low index dielectric material (Silicon nitride), operating as a supporting material, (see Figure 2.7). These type of structures have previously been proposed theoretically, and have been suggested as nanostructures where assymetric transmission, bistable response and chirality control could be actuated based on optical forces, [89], [91]. I am the first one to develope experimentally these structures, (see Figure 2.7), with great uniformity. The high aspect ratio between the length and the width of each wire, make the fabrication of these samples a challenging task, where a balance between internal stress and elastic force is needed to be found in order to provide a uniform metamaterial array,(see Figure 2.7c). An optimum aspect ratio is possible to be found in order to fabricate these kind of structures. In the structure presented in Fig. 2.7, a pair of bricks with assymetric thickness were fabricated, (see inset Fig.2.7c). Each nano-beam was 14um long with a width of 300nm, while the unit cell size was 900nm x 750nm. However, Ga^+ implantation hampers optical resonance in this structure as the resonant optical modes excited are very sensitive to losses induced by FIB milling. Appropriate techniques such as low ion beam acceleration voltage and current, or

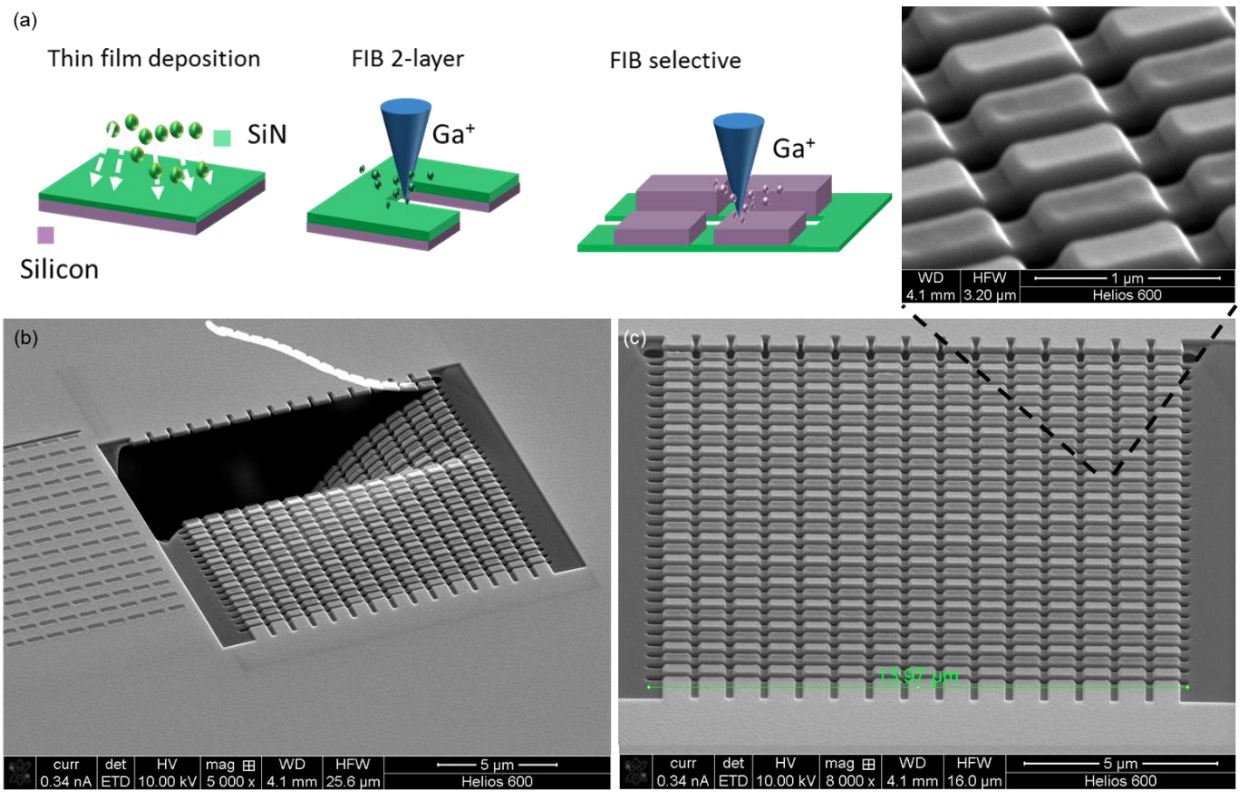

Figure 2.7 Bilayer Si/SiN nano-membrane metamaterials. (a) Schematic of bilayer all-dielectric metamaterial fabrication: a 100 nm thick Si membrane in 1 cm^2 Si frame was deposited by SiN, 100nm . Afterwards, a highly concentrated ion column sputters target materials after ion bombardment of high momentum. Fib milling define an array of nano-wires with extreme aspect ratio, while in the next stage FIB selectively defines nanostructured patterns on the silicon film only(b) SEM image of unsuccessful attempt of a sample where strength of the supporting layer was not enough to hold the Silicon nano-bricks. (c) Oblique view of the nano-brick array: period = 750nm x 900 nm, dark areas = air, gray areas SiN only while every pair of brick have different thickness.

the use of a sacrificial layer or an e-beam lithographic method could be used as alternatives to improve the optical response of those devices.

Overall free-standing nano-membrane metamaterials seem adequate to provide optomechanical response as they can provide both optical resonances at NIR and vibrational modes in the MHz to sub-GHz regime excited via optical forces. A proper design is needed to excite optical forces, while at the same time the device needs to be optically sensitive to any structural deformation to provide a nonlinear optical response.

2.2 Nano-optomechanical nonlinear dielectric metamaterials

Non-metallic metamaterial nanostructures currently attract intense attention as they promise to reduce the losses and costs associated with the use of noble metals in traditional plasmonic architectures. [25] It has already been shown that oxides and nitrides, [24] graphene, [100] topological insulators, [53] and high-index dielectrics [26], [27], [34], [36], [37], [41], [82], [92], [94], [101] can be used as platforms for the realization of high-Q resonant metamaterials. A variety of non-metallic media, such as graphene, [102] carbon nanotubes, [103] liquid crystals [104] and semiconductors, [105], [106] have also been engaged through hybridization with plasmonic metamaterials to create media with strongly enhanced optical nonlinearities, while a nano-optomechanical nonlinearity has recently been observed in a plasmonic metamaterial. [107] Here I experimentally demonstrate an all-dielectric metamaterial, fabricated from a free-standing semiconductor nano-membrane, with sharp near-infrared optical resonances. It exhibits a strong optical nonlinearity associated with light-induced nano-mechanical oscillations of the structure, which change the physical configuration and thus the resonant response of the metamaterial array's constituent meta-molecules.

Optical forces at the sub-micron scale can be comparable or even stronger than elastic forces, and resonantly enhanced optical forces in photonic metamaterials have been theoretically studied for both plasmonic and all-dielectric structures.[88]–[90] The exchange of energy between incident light and a nano-mechanical resonator can be further enhanced when the light is modulated at the mechanical eigenfrequency of the resonator. Indeed it has recently been shown that plasmonic metamaterials can be optically reconfigured on this basis with light modulated at MHz frequencies. [107] In consequence of the fact that the mechanical eigenfrequencies of objects are dictated by their stiffness (Young's modulus) and dimensions, nano-scale mechanical oscillators made of silicon offer the prospect of mechanical vibration at hundreds of MHz or even GHz frequencies.

Considerable efforts have been devoted to the reduction of radiative losses in resonant plasmonic metamaterials, as non-radiative losses (Joule heating) are unavoidable in the constituent metals. In 'all-dielectric' metamaterials non-radiative losses are a-priori limited, so with appropriate design they can present even stronger optical resonances, and thereby generate stronger optical forces, than plasmonic counterparts. [90] Previous works have demonstrated that high-index media such as silicon can support optical frequency resonances [26], [27], [34], [36], [37], [41], [82], [92], [94], [101] and we harness that characteristic here to engineer an ultrathin medium with optical properties that are highly sensitive to structural reconfiguration.

The metamaterial is fabricated by direct focused ion beam milling of a commercially sourced (Norcada Inc.), 100 nm thick polycrystalline silicon membrane in a silicon frame (Figure 2.8a). To date, all-dielectric metamaterials have invariably been realized as 'positive' structures – arrays of discrete high-index features (nanorods, discs, bars, etc.) supported on a lower-index substrate. [26], [27], [34], [36], [37], [41], [82], [92], [94], [101] The metamaterial employed in the present study shows however that strong localized resonances can also be excited in 'negative' dielectric nanostructures, i.e. a pattern formed by slots cut into a continuous layer of high-index material. The free-standing configuration has the additional advantage of maximizing refractive index contrast with the near-field environment and thereby resonance quality factor. [108] Each 1.05 μm × 1.05 μm unit cell (meta-molecule) contains a rectangular nano-cantilever of length L = 300 nm and width W = 600 nm, with an additional slot across

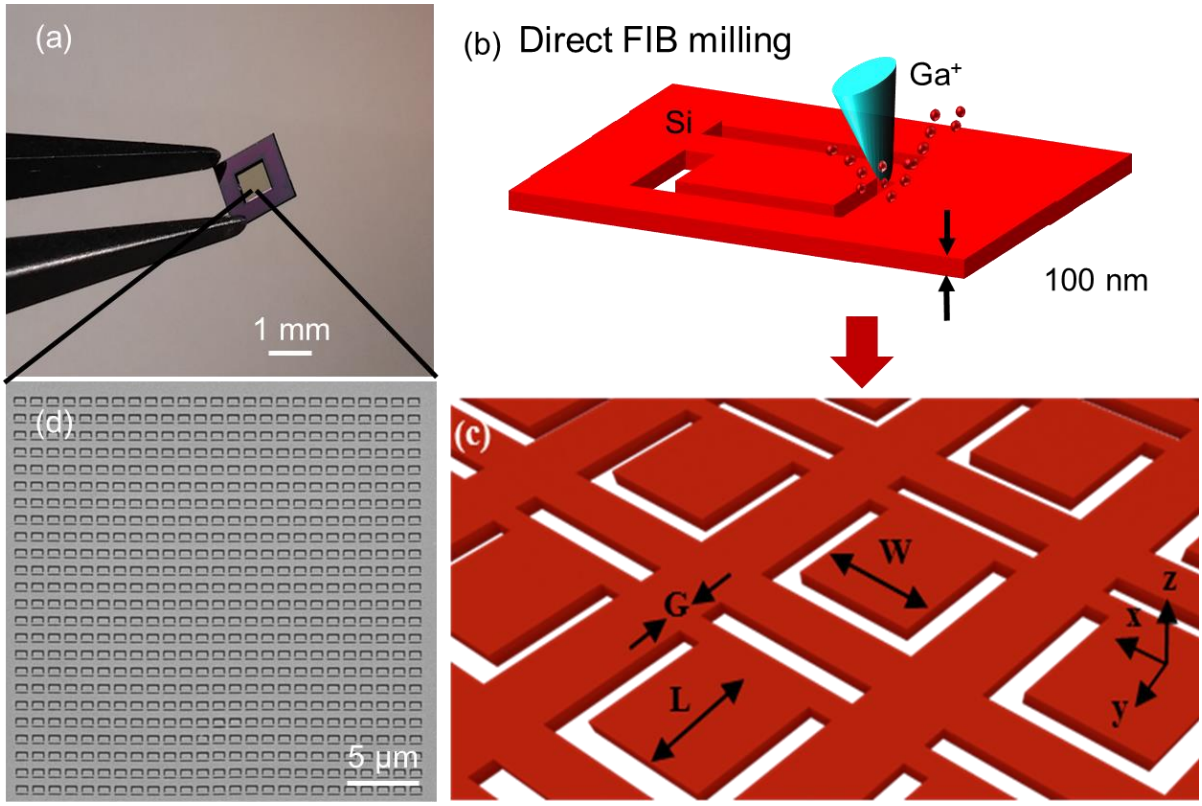

Figure 2.8 Free-standing silicon nano-membrane metamaterials. (a) 100 nm thick Si membrane in 1 cm^2 Si frame used as a platform for fabrication of free-standing all-dielectric metamaterials. (b) Schematic of FIB principle, a highly concentrated ion column sputters target materials after ion bombardement of high momentum. (c) Schematic oblique view of the nano-cantilever array: period = 1.05 μm; *L* = 300 nm; *W* = 600 nm; *G* = 100 nm; slot width = 100 nm. (d) Scanning electron microscope image of part of a nano-cantilever metamaterial array fabricated in a Si membrane by focused ion beam milling [dark areas = slots cut through the membrane].

the fixed end of the cantilever arm to increase flexibility (Figure 2.8c shows a geometric schematic of the structure). The metamaterial array is composed of 25 × 25 meta-molecules.

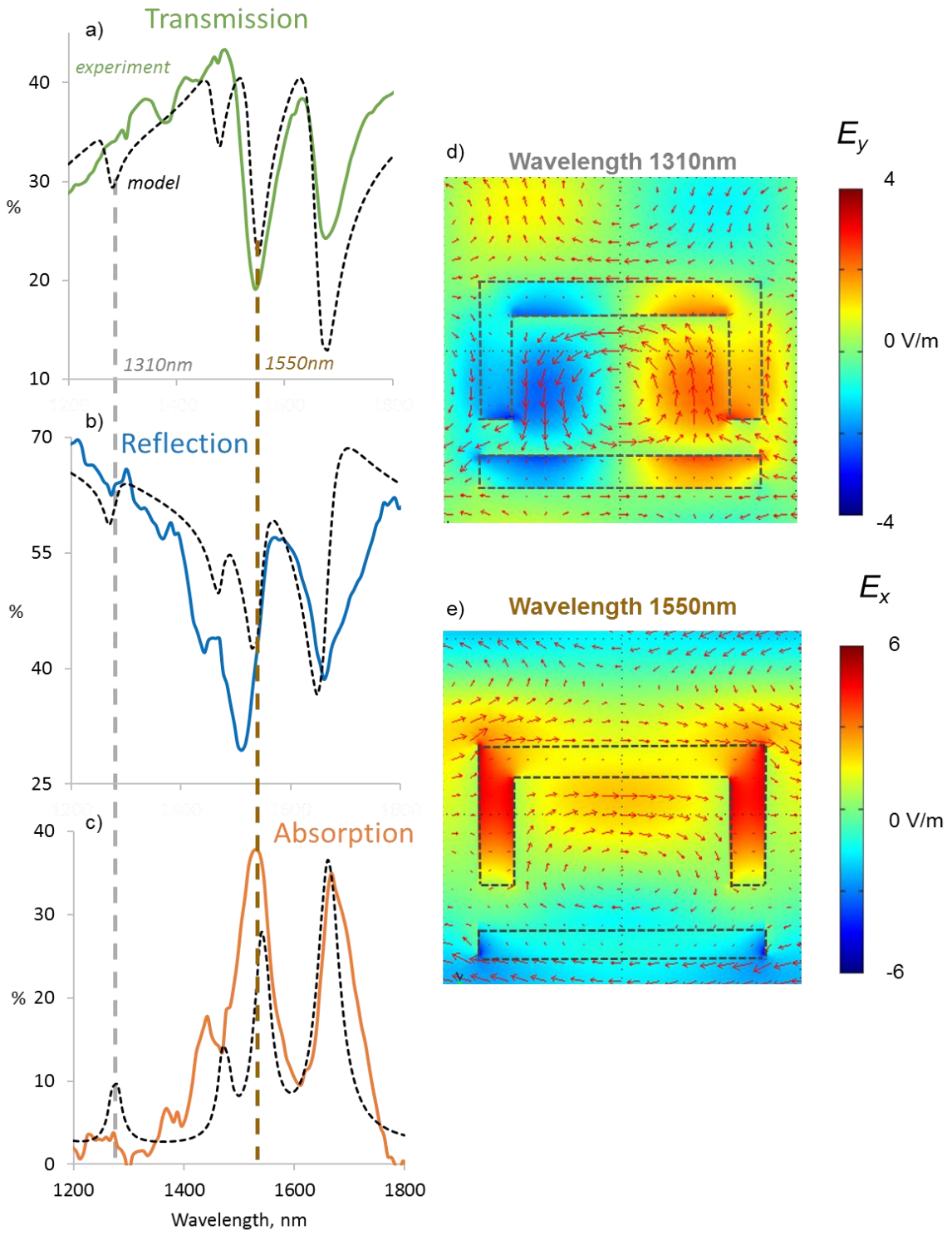

Figure 2.9 Optical resonances in free-standing silicon nano-membrane metamaterials. (a-c) Normal incidence reflection, transmission and absorption spectra of the metamaterial for *x*-polarized light. Black lines correspond to experimental measurements, dashed lines to numerical modelling results; Grey lines show measured spectra for the unstructured silicon membrane. (d,e) Field maps, in the *xy* plane at the mid-point of the membrane thickness, for (d) the electric mode resonance at 1550 nm [E_x field component] and (e) the magnetic mode at 1310 nm [E_y field] – experimental pump and probe wavelengths respectively. The field maps are overlaid with arrows indicating the direction and magnitude of electric displacement.

This structure supports several optical resonances in the near-infrared range, as illustrated by the microspectrophotometrically measured reflection, transmission and derived absorption spectra presented in Figs. 2.9. This data shows good correlation with spectra obtained via 3D finite element numerical modelling (Comsol MultiPhysics), using a fixed complex refractive index for polycrystalline silicon of 3.2 + 0.04i (following Ref. [109] with an imaginary part tuned to reproduce the observed resonance quality at the experimental pump wavelength of 1550 nm – the elevated value being representative of material and manufacturing imperfections including gallium contamination from the ion beam milling process).

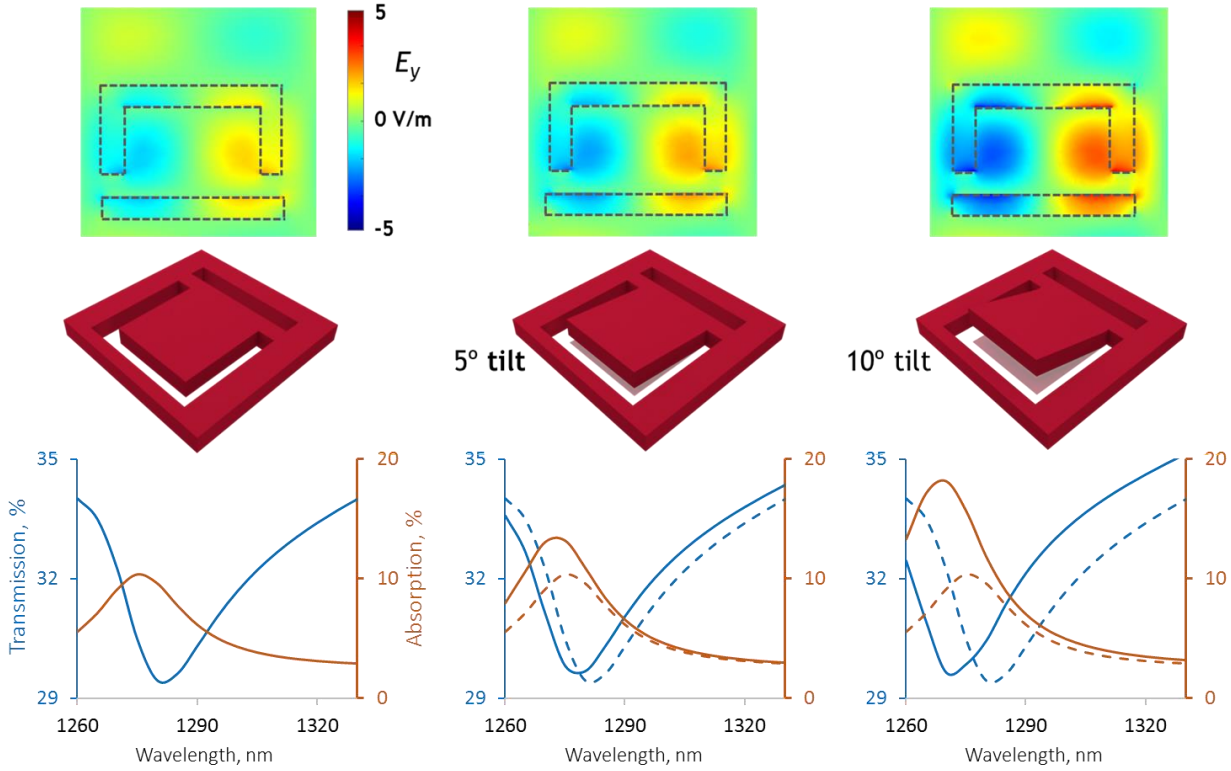

Figure 2.10 Changes in optical properties resulting from structural reconfiguration. (a) Numerically simulated dispersion, Transmission and Absorption of metamaterial around the experimental 1310 nm probe wavelength for a 0o, 5o, 10o of nano-cantilever tilt angles, as labelled and illustrated schematically to the bottom, alongside corresponding *Ey* field maps for the xy plane at the mid-point of the membrane thickness at 1310nm, top row. As the cantilever tilts the resonance blueshifts, this can be justified, if you consider that effectively the length of cantilevers shortens.

In order to achieve a strong optomechanical nonlinearity we require a metamaterial that is highly sensitive at the probe wavelength (1310 nm in the present case) to structural reconfiguration driven by strong optical forces generated within the structure at the pump wavelength (1550 nm). Fig. 2.10 shows simulated transmission around 1310 nm and corresponding maps of field distribution at this wavelength for three different configurations – tilt angles – of the metamolecule nano-cantilevers. The probe wavelength sits to one side of a

resonance based upon a spatial distribution of electric field and displacement currents in the cantilever arms which generate magnetic dipoles (in the manner of the familiar plasmonic asymmetric split ring metamaterial 'trapped mode' [23]). The spectral dispersion depends strongly on the cantilever tilt angle, with the resonance blue-shifting as the cantilever arms tilt out of plane (i.e. as their effective length decreases), resulting in a transmission increase at the fixed 1310 nm probe wavelength (there is a concomitant reflectivity decrease, and no meaningful change in absorption).

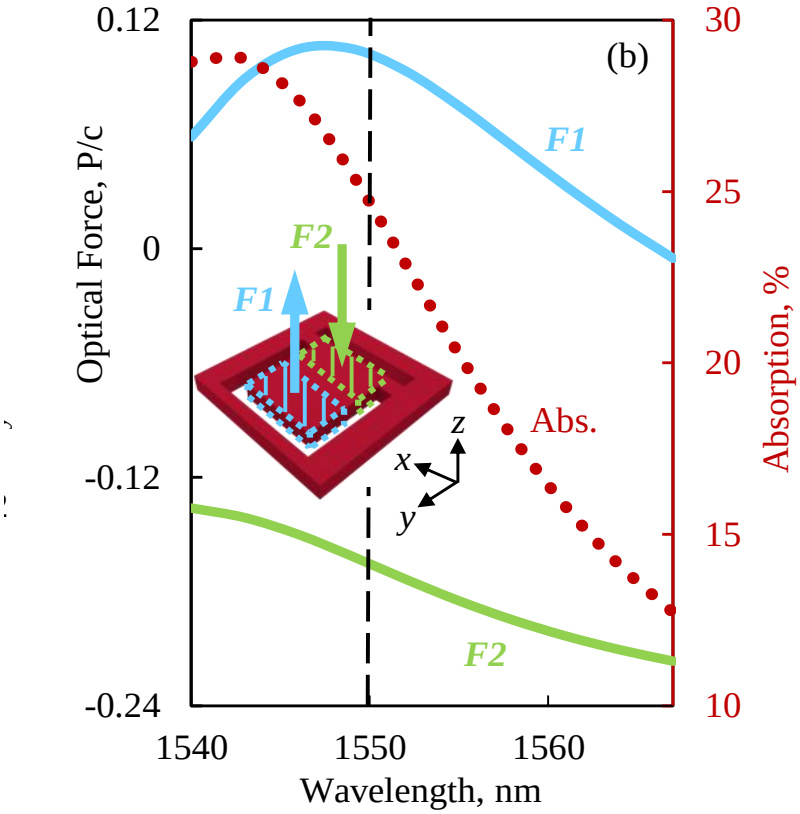

Figure 2.11 Modelling of optical forces in a periodic array of silicon nano-cantilevers. Spectral dispersion of the normalized out-of-plane optical forces acting on either end of the meta-molecule nano-cantilevers [as illustrated inset], and of metamaterial absorption, around the experimental 1550 nm pump wavelength. [In all cases, simulations assume normally-incident, *x*-polarized light.] opposite pair of forces act in every metamolecule result in out of plane displacement of the tip.

The absorption resonance at around 1550 nm waveband is derived from the excitation of an electric dipole, hybridized with higher order electric multipoles, within each unit cell (Figure 2.9 e), giving rise to a spatial distribution of optical forces that tilts the cantilever arms out of the sample plane. In classical electrodynamics the components of the total time-averaged force F acting on an object illuminated with light can be calculated using the surface integral: [110]

$$\langle F_i \rangle = \oiint_S \langle T_{ij} \rangle n_j dS \qquad (2.1)$$

S being a closed surface around the region of interest, nj are the unit vector components pointing out of the surface and <Tij> is the time-averaged Maxwell stress tensor defined by

$$\langle T_{ij} \rangle = \frac{1}{2} Re \left[\varepsilon \varepsilon_0 \left(E_i E_j^* - \frac{1}{2} \delta_{ij} |E|^2 \right) + \mu \mu_0 \left(H_i H_j^* - \frac{1}{2} \delta_{ij} |H|^2 \right) \right] \quad (2.2)$$

The optical force given by equations (2.1) & (2.2) encompasses both radiation pressure, which arises through the transfer of momentum between photons and any object on which they impinge, and the gradient force, which is associated with intensity variations in the local field around an object. Applied to the metamaterial unit cell (Fig. 2.11), this stress tensor analysis reveals antiparallel forces acting on the two ends of the cantilever arms – a net 'positive' force F1 (in the +z direction towards the light source) at the free end of the arm and an opposing force F2 (in the –z direction of light propagation) at the other.

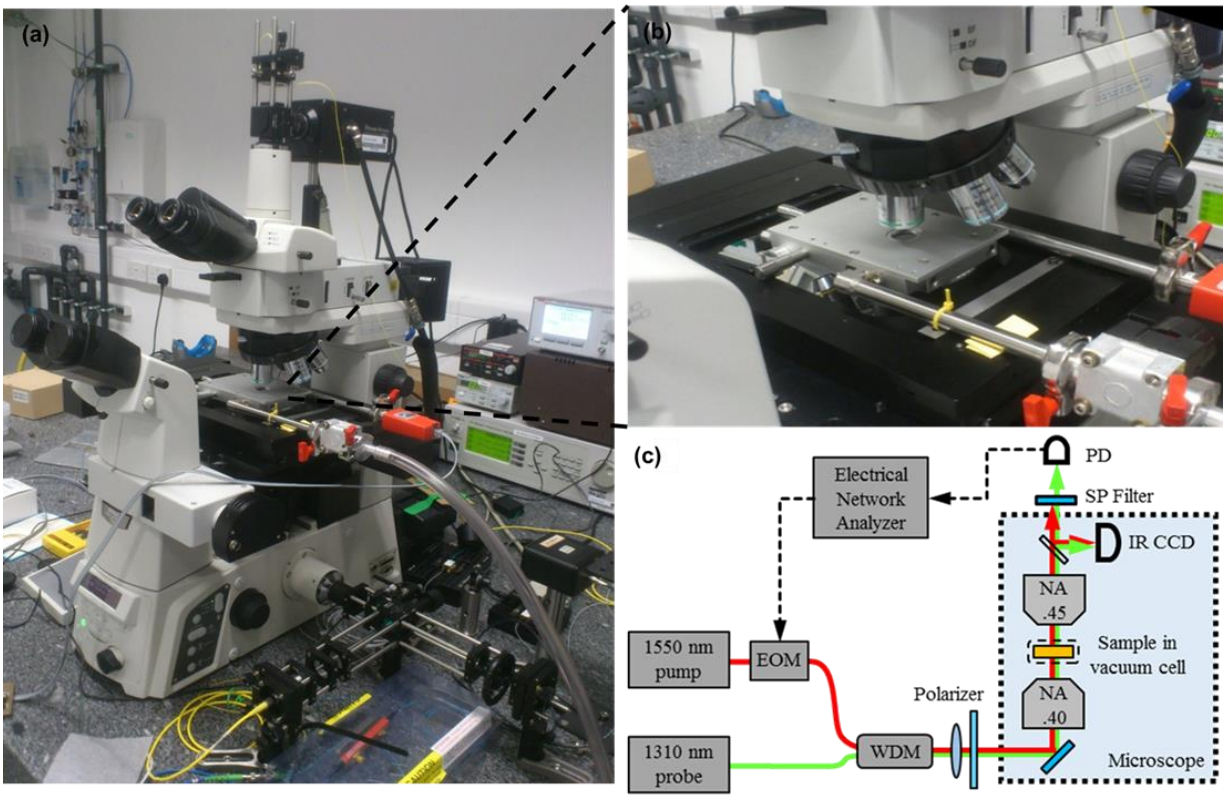

Figure 2.12 Measuring the nonlinearity of nano-optomechanical all-dielectric metamaterials. (a) An inverted microscope is used as a stage to focus light on the sample and afterwards collected on a fast photodetector. (b) inset presents the vacuum chamber (Linkam stage) where sample was kept in low pressure, 10^{-4} bar. (c) Schematic of the pump-probe experimental arrangement for transmission-mode measurements of metamaterial nonlinear response.

In normalized units these can respectively reach levels of 0.1 and -0.16 P/c (where P is the incident power per unit cell and c is the speed of light). In absolute terms, for an illumination intensity of 60 μW/μm2, this corresponds to a force of ~20 fN on the cantilever tip and an opposing force of ~35 fN at the hinge, which would be sufficient to induce a static deformation

(i.e. tilt) of only 2″ - displacing the tip of the cantilever arm by ~5 pm. However, much larger deformations can be achieved by the same instantaneous driving forces at the structure's mechanical resonances, where displacement will be enhanced by the quality factor of the mechanical resonator. Assuming a Young's modulus of 150 GPa [111] for the silicon membrane, the first mechanical eigenmode of the 300 nm meta-molecule cantilevers – the out-of-plane oscillation of the arms – is expected to occur at a frequency of 165 MHz.

The optomechanical nonlinearity of the free-standing silicon membrane metamaterial was evaluated using the pump-probe experimental configuration illustrated schematically in Fig. 2.12. Probe and pump beams at 1310 and 1550 nm respectively are generated by CW single-mode-fiber-coupled diode lasers, with the pump beam subsequently electro-optically

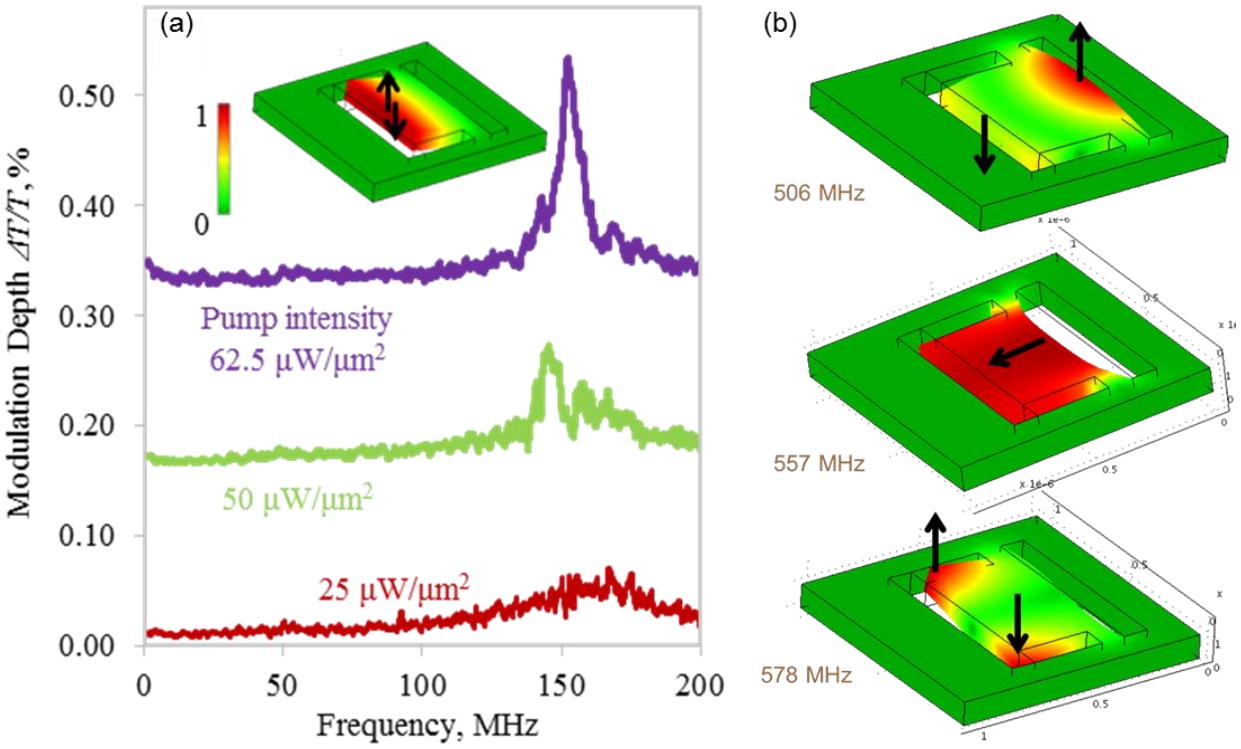

Figure 2.13 Nonlinear optical response of all-dielectric metamaterials based on optomechanical coupling. (a) 1310 nm [probe] transmission modulation depth as a function of pump [1550 nm] modulation frequency for a selection of peak pump intensities [as labelled]. The inset shows a nano-cantilever unit cell colored according to the relative magnitude of out-of-plane displacement, from numerical modelling, for the structure's first mechanical eigenmode. (b) the mechanical eigenmodes of higher order are presented here. It is apparent due to the complex type of deformation not all the mechanical modes are coupled with incident light, except the 1st mode inset in column (a).

modulated at frequencies up to 200 MHz. The beams are combined using a wavelength division multiplexer into a single fiber and then pass via a free-space collimator to the input port of an optical microscope operating in transmission mode. They are focused at normal incidence to concentric spots on the metamaterial, with diameters of ~10 μm. A fixed probe intensity of 25 μW/μm^2 is maintained at the sample, while peak pump intensity is varied up to a maximum

level of 62.5 $\mu W/\mu m^2$. A low-pass filter blocks transmitted pump light and the probe signal is monitored using an InGaAs photodetector (New Focus 1811) connected to an electrical network analyzer (Agilent Technologies E5071C). The sample is held under low vacuum conditions at ~0.1 mbar to reduce atmospheric damping of mechanical oscillations. Figure 2.13a presents the relative pump-induced change in probe transmission as a function of pump modulation frequency. As pump intensity increases the observed optomechanical resonance grows in strength and collapses spectrally to a central frequency of 152 MHz, reaching a maximum modulation depth of 0.2%. From numerical modelling, a transmission change of this magnitude corresponds to an induced nano-cantilever tilt of order 10', or a tip displacement of ~830 pm – some two orders of magnitude more than the expected static displacement at the same pump intensity. This implies a mechanical resonance quality factor of order 100, though we take this to be a lower limit on the value for individual silicon cantilevers inhomogenously broadened (due to slight manufacturing defects and structural variations) across the metamaterial array. Indeed, at low pump intensities a spectrally disparate set of peaks emerges, suggestive of the distribution of individual cantilevers' different mechanical eigenfrequencies. At higher intensities the coupling among oscillators leads to synchronization and collective oscillation at a common frequency in good agreement with the computationally projected frequency of the structure's first mechanical eigenmode.

It is instructive to estimate what nonlinear susceptibility a hypothetical homogeneous medium would need to possess to provide a response of comparable magnitude to the nano-optomechanical silicon membrane metamaterial: Absorption in a nonlinear medium is conventionally described by the expression $-dI/dz = \alpha I + \beta I^2 + ...$, where I is light intensity, z is the propagation distance in the medium and α and β are the linear and nonlinear absorption coefficients respectively. The observed nonlinear transmission change ΔT is proportional to the pump power, so can be quantified via an estimate of the first nonlinear absorption coefficient $\beta \sim \Delta T/(It)$, where t is the metamaterial thickness. At the 152 MHz resonance frequency, $\beta \sim 7\times10^{-5}$ m/W, which corresponds to a nonlinear susceptibility of order $Im\{\chi(3)\}/n^2 \sim 3.9\times10-14\ m^2V^{-2}$.

In conclusion, by structuring a free-standing nano-membrane of silicon at the sub-wavelength scale we engineer optical resonances strong enough to deliver a substantial optomechanical nonlinearity in an otherwise linear ultrathin medium. The nonlinear all-dielectric metamaterial operates at sub-GHz frequencies and μW/unit-cell intensities in the near-infrared spectral range. These free-standing all-dielectric metamaterials offer a compact, energy efficient and

fast active optoelectronic platform potentially suited to practical application in high speed photonic applications. Improvements may be made in the design and fabrication of membrane metamaterials to enhance the probe transmission or reflectivity change per degree of tilt or nanometre of displacement, and to maximize the efficacy with which optical forces can generate such movements. But even while absolute changes are small, their sharply resonant nonlinear character may serve a variety of sensing (e.g. gas pressure, chemical binding) applications.

Chapter 3

Electro-optical Reconfigurable Dielectric Metamaterials

3.1 All-dielectric nano-mechanical metasurface electro-optic modulator

The interface between electronic and optical/photonic signals is of enormous technological importance at macro-, micro-, and increasingly nano-scopic scales. This is true both of the conversion between signal formats – i.e. generation and detection of light and in the context of electrically controlling (modulating/routing) guided and free-space optical signals/beams. In regard to the latter, mechanisms for electrically controlling the optical properties of bulk or thin film media and surfaces have been the subject of research interest over many decades. The Kerr and Pockels electro-optic effects are widely used in amplitude and phase modulators, carrier-induced changes in doped semiconductors are harnessed in optoelectronic and silicon photonic devices [58] ; Liquid crystals (electric field-induced molecular reorientation) and MEMS (micro-electro-mechanical systems) are the foundation of numerous display, spatial light modulation and adaptive optics technologies.

In recent years, photonic metamaterials – manmade media with nanostructurally engineered optical properties [62] – have emerged as an enabling technology platform within which all kinds of light-matter interaction can be resonantly enhanced. Large electro-optic effects (reversible changes in transmission, reflection and absorption of light) can be achieved over extremely short (subwavelength) interaction lengths through the hybridization of active media (e.g. semiconductors [105], [112], graphene [102], phase-change materials [73], [113]–[115], liquid crystals [104], [116]) with plasmonic nanostructures. Nano-mechanical plasmonic metasurfaces can deliver effective electro-optic coefficients orders of magnitude larger than any naturally occurring material [77] and interaction regimes (e.g. electro-magneto-optic effects [98]) with no analogue in conventional nonlinear optics. However, plasmonic architectures are unsuitable for many applications [24], [95]: they are absorbing in the visible to near-infrared spectral range (i.e. insertion losses are high even at nanoscale thickness); they cannot withstand high optical intensities (as a consequence of resonantly enhanced absorption

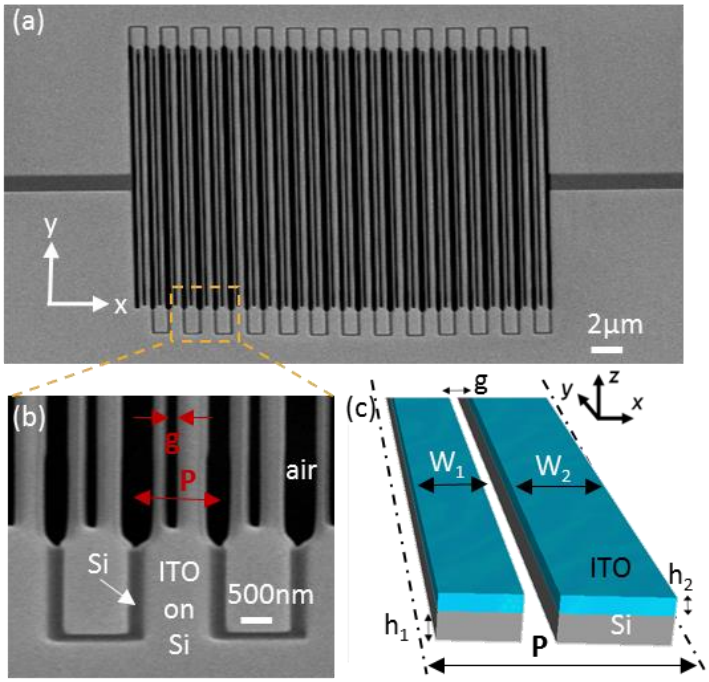

Figure 3.1 All-dielectric nano-mechanical metasurface (a) Scanning electron microscope image of a free-standing nanowire array [viewed at oblique incidence] manufactured in a silicon/ITO bilayer membrane. (b) Plan view SEM image showing detail of the periodic arrangement of asymmetric nanowire pairs and the structure imposed at each end of the array where the ITO layer is selectively etched to electrically isolate pairs of nanowires. (c) Dimensional schematic of the asymmetric Si/ITO nanowire pair within each period of the metasurface array [by design, $P = 800$, $h_1 = 100$, $h_2 = 70$, $w_1 = 180$, $w_2 = 240$, $g = 80$ nm].

local temperatures may readily exceed the size-effect-suppressed melting points of nanostructured noble metals); and they are not compatible with established (CMOS) micro/nanoelectronic manufacturing processes. For these reasons, attention has lately turned towards 'all-dielectric' photonic metamaterials and metasurfaces [36], [37], [39], [41], [82], [93], with active switching and tuning of optical (VIS-NIR) properties experimentally demonstrated via liquid crystal hybridization,[82] elastic substrate deformation, [52] two-photon absorption in silicon, [43], [117] opto-mechanical reconfiguration, [118] and non-volatile optically-induced phase transitions in chalcogenide glass.[119] Here we present an electrically controlled, free-standing, all-dielectric metasurface (Figure 3.1) in which electrostatic forces are harnessed to reversibly reconfigure the structure, providing a mechanism for low-voltage/low-power reflectivity and transmission modulation.

Devices are manufactured on commercially sourced polycrystalline silicon membranes (1 mm × 1 mm windows supported in 200 µm thick silicon frames). These are coated (including the frame) with 70 nm of indium tin oxide by radio-frequency sputtering from an In2O3/SnO2 (90/10 wt%) alloy target. A base pressure of 4 × 10-5 mbar was achieved before deposition and a high-purity argon gas flow of 70 ccpm was used to strike the plasma. A 20:5 argon: oxygen deposition gas mixture was used to maintain the plasma and ensure sufficient oxygen content

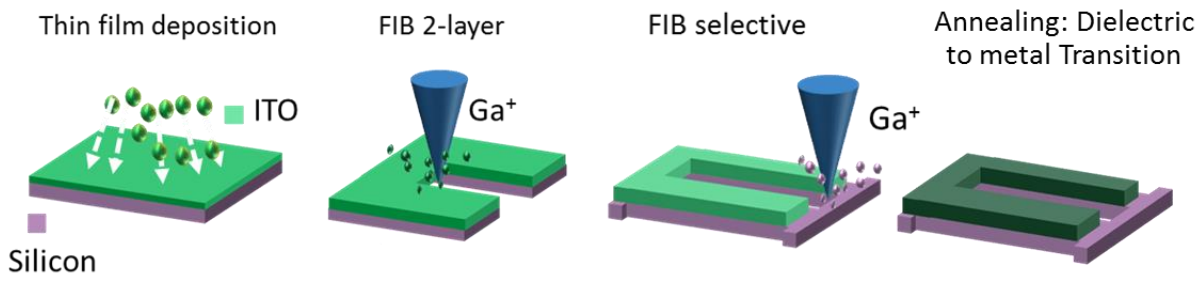

Figure 3.2 Fabrication procedure of all-dielectric electro-optical metamaterial.

in the deposited ITO film. The membrane substrate was held on a rotating platen approximately 150 mm from the target where it is subject to a temperature increase of <10°C during deposition, ensuring minimal stress in the film, which was subsequently annealed at 200°C for 60 minutes under an oxygen atmosphere to increase conductivity (measured sheet resistance decreases from 3.4 x 10^6 Ohm/sq to 1 x 10^3 Ohm/sq; carrier concentration increases from 3.5 x 10^{16}/cm^3 to 10^{21}/cm^3). Metasurface nanostructures - one-dimensional arrays of 20 μm long nanowires with a period of 800 nm (Figure 3.1), were fabricated by focused ion beam (FIB) milling from the ITO side of the bilayer membrane (cutting through both layers of material). Each period contains an asymmetric pair of Si/ITO strips (one 300 nm wide, the other 200 nm wide) separated by a gap of 100 nm, which was subsequently annealed at 200°C for 60 minutes in oxygen atmosphere, see Figure 3.2. The optical response of the nanowire array is predominantly determined by the silicon component (see Fig. 3.3 below) while the ITO layer provides electrical connectivity to facilitate electrostatic tuning of the gap size g. To this end the ITO layer alone is further patterned at the ends of the nanowires such that the two nanowires in each asymmetric pair are electrically isolated from each other and connected to opposing terminals either side of the device.

The nature of the metasurface is (inevitably) anisotropic optical response and its dependence on the gap size g are revealed in numerical simulations (Figure 3.3). We model a single period of the nanowire array in the cross-sectional xz plane (as defined in Figure 3.1) with periodic boundary conditions in the y-direction (i.e. effectively assuming an infinite array of infinitely long nanowires) using the finite element method (Comsol MultiPhysics). The simulations utilize material parameters for polycrystalline silicon and for ITO derived from ellipsometry measurement. Both have weakly dispersive refractive indices in the near-IR spectral range above ~1300 nm: around 3.8 + 0.002i for Si and 1.9 + 0.08i for ITO), and they assume normally incident, narrowband, linearly polarized plane wave illumination. For TE-polarized light (incident electric field parallel to the nanowires) the metasurface presents a sharp (Q ~94) Fano-

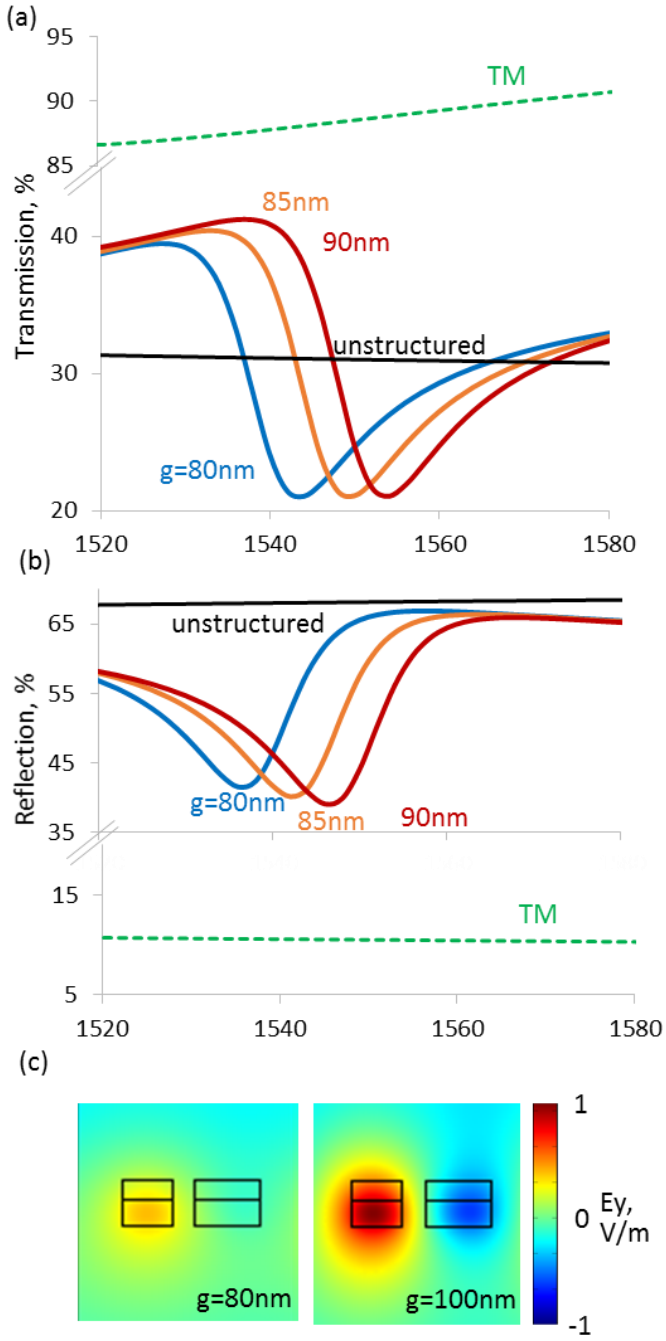

Figure 3.3 Computational modelling of Si/ITO assymetric nanowires metasurface. (a, b) Numerically simulated transmission (a) and (b) reflection spectra for the Si/ITO nanowire array geometry of Fig. 1c, for normally incident TE- and TM-polarized light [electric fields respectively parallel and perpendicular to the nanowires], and corresponding [polarization independent] spectra for the unstructured Si/ITO bilayer membrane. TE spectra are presented for a selection of gap sizes *g* [as labelled]; TM spectra are invariant with *g*. (c) Cross-sectional maps in the *xz* plane of the TE-mode E_y field distribution over a single period of the metasurface array, i.e. an asymmetric pair of nanowires, for gap sizes *g* = 80 nm (c) and 100 nm (d) at the 1542 nm optical resonance wavelength for *g* = 80 nm.

type resonant response that is based upon the excitation of anti-parallel displacement currents in the nanowire pairs (predominantly within the silicon as illustrated in Figure 3.3c) and reliant upon their dimensional asymmetry. [120] Resonances are blue-shifted and the local field strength in the nanowires increases as their separation g decreases, leading to substantial

changes in reflectivity and transmission. For example, a reduction in gap size from 100 to 80 nm produces an increase of 30% in absolute reflectivity at 1550 nm and a decrease of 25% in transmission at the same wavelength. For TM-polarized light no resonant mode is supported; reflectivity and transmission are weakly dispersive (as for the unstructured Si/ITO bilayer) and do not depend on gap size.

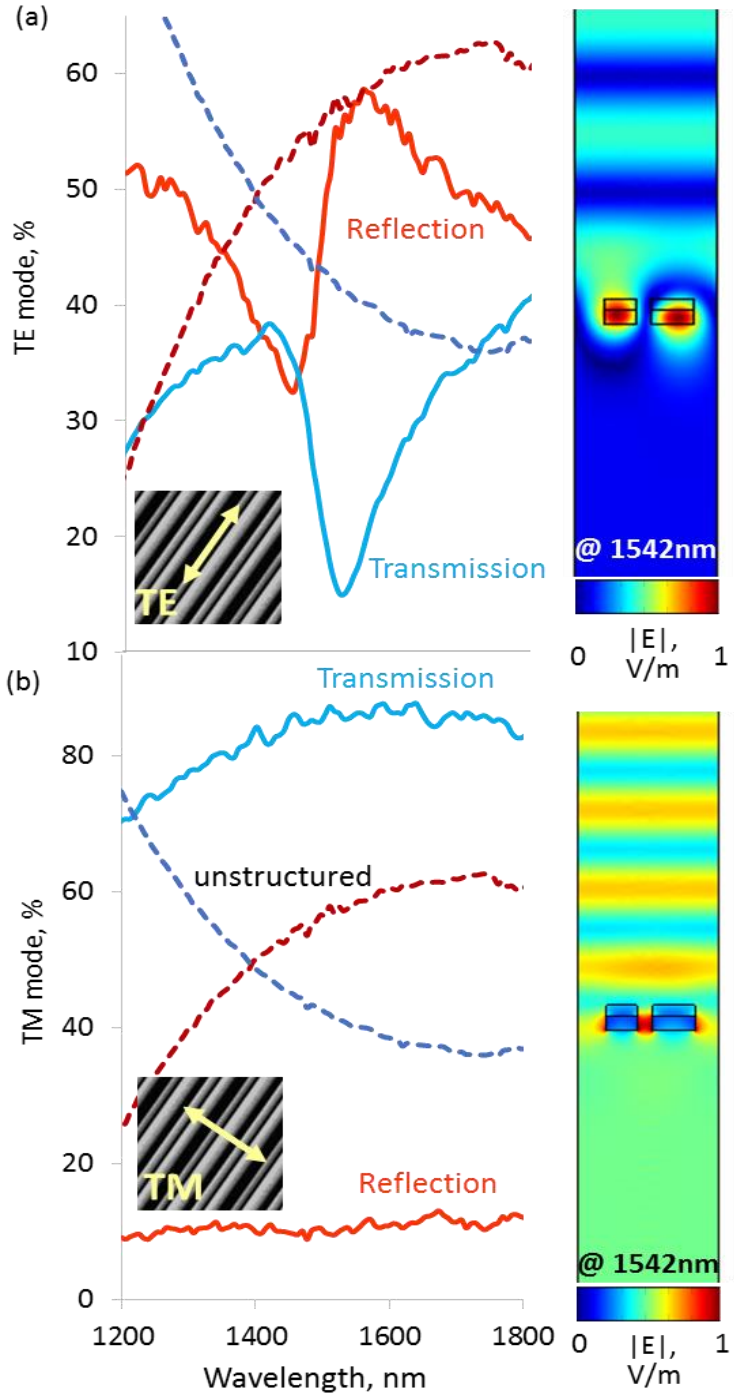

Figure 3.4 Si/ITO nanowire metasurface optical characterization. Microspectrophotometrically measured reflection and transmission spectra (continuous line) for the Si/ITO nanowire array shown in (a) for TE- and (b) TM-polarized light, with corresponding Electric field maps for a single pair of wires. spectra for the unstructured Si/ITO bilayer membrane has been plotted (dashed line) for comparison with nanostructured response.

Normal incidence reflection and transmission spectra for experimental metasurface devices (Figure 3.4) are measured using a microspectrophotometer with a 15 μm × 15 μm sampling domain. For the TE-mode, the spectral positions of observed trapped resonant modes (for the as-fabricated nanowire pair separation g = 100 nm) are well-matched to numerical simulations,

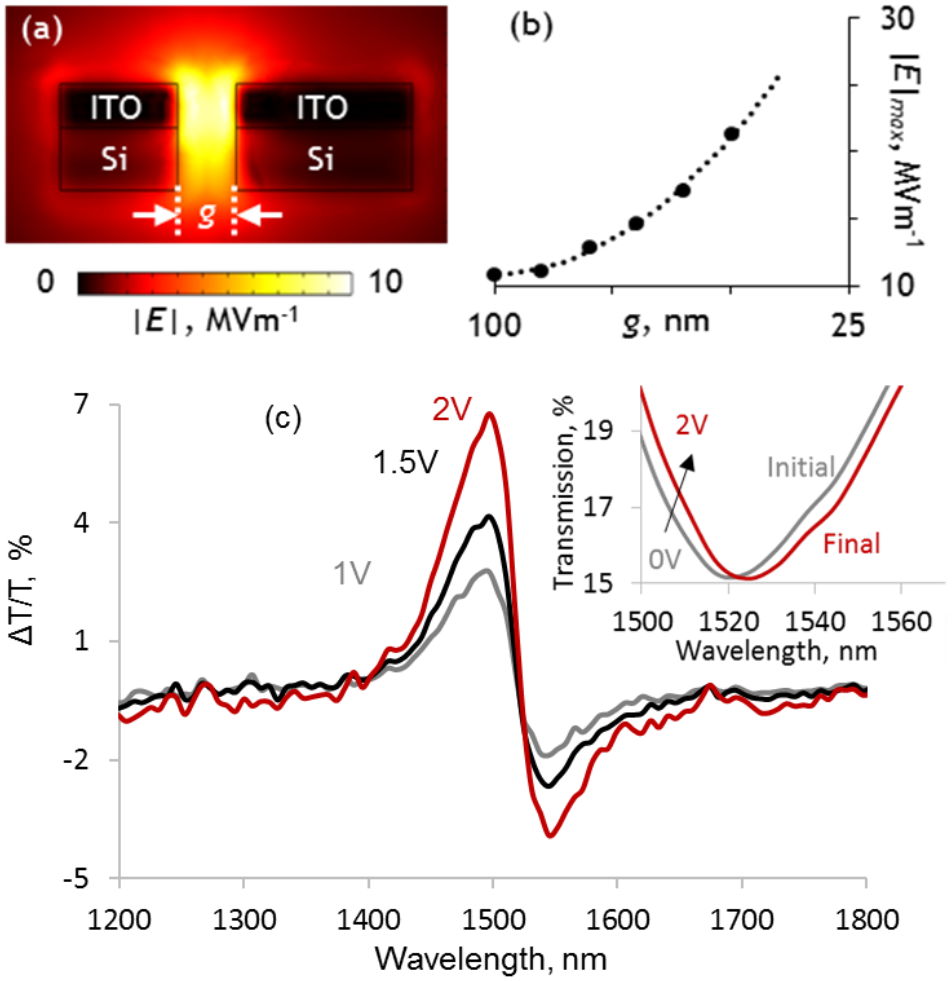

Figure 3.5 DC electro-optic modulation of Si/ITO metasurface optical properties. (a) Numerically simulated cross-sectional map in the *xz* plane of the static electric field amplitude over a single period of the metasurface array for a gap sizes g = 80 nm and an applied bias of 1V between the ITO sections of the two nanowires. (b) Maximum electric field amplitude [at the midpoint of the gap between the nanowires] as a function of gap size, for a fixed 1V bias. (c) Experimentally measured dispersion of relative transmittivity change for the Si/ITO nanowire metasurface under a selection of applied bias levels [as labelled]. The inset shows the absolute Transmission change for the initial and final state, shaded according to applied electrical bias.

with discrepancies in center wavelength and reduced resonance quality ($Q_{experiment}$ ~35) being attributed to manufacturing imperfections associated with the FIB milling process (deviations from the perfect rectilinear model geometry, such as rounding of edges; and implantation of gallium ions), inhomogeneous broadening, and surface roughness (scattering). For the TM mode an opposite behaviour is recorded, where light penetrates the metasurface with more than 80% Transmission across the measured wavelengths. As near field maps reveal in TM mode electric field is mostly concentrated within the gaps of the nano-wires, lead to a broadband high

transmission.

Electronically actuated tuning of metasurface optical properties was subsequently studied, the transmission spectra of the reconfigurable metamaterial were recorded using a microspectrophotometer (CRAIC Technologies) while applying various DC voltages (via the source measurement unit) to tune the mechanical configuration of the nanostructure . Under an applied bias the two Si/ITO nanowires in each asymmetric pair are subject to electrostatic forces of mutual attraction and (more weakly by virtue of greater separation) of repulsion from the nearest neighboring wires of the adjacent pairs. In consequence, the two nanowires in each pair bend towards one another, decreasing the gap size g (non-uniformly along the nanowire length as the ends are fixed). While the elastic restoring force on a given nanowire increases linearly with displacement from its equilibrium position (i.e. with decreasing gap size), the field strength in the gap (Figure 3.5a) and thereby the electrostatic force of attraction grows as $1/g$. When the electrostatic force exceeds the elastic restoring force the gap between the nanowires will abruptly close, at which point Van der Waals forces will likely ensure that it remains closed even when the applied bias is removed or reversed. The metasurface modulator is therefore operated below this ~3V irreversible switching threshold[12]. In the low frequency limit, power consumption is dominated by leakage resistance of 75 kΩ and amounts to only 3.3 μW at a bias of 0.5V (120 μW at 2V).

Electrostatic tuning of the nanowire separation brings about a continuous and reversible change in metasurface TE transmission consistent with expectation based upon the above numerical simulations. The resonance is blue-shifted with increasing applied bias (i.e. decreasing gap size) but also broadened as a result of the fact that the change in gap size is non-uniform over the nanowire length. We evaluate the relative induced change in reflectivity as $(T_x-T_0)/T_0$, where T_x is the absolute transmission at an applied bias of x Volts and T_0 is the zero-bias level (Figure 3.5c). The change most pronounced, reaching almost 7% at 3V, in the wavelength around the trapped mode at 1500nm. (Refractive index change due to carrier accumulation in the ITO is excluded as a mechanism for the induced metasurface transmission change as capacitive electron accumulation layers, having a thickness of only ~1 nm from Thomas-Fermi screening theory, [121] comprise a negligible volume fraction of the structure.)

We further assess dynamic response characteristics as part of the present study. The Si/ITO modulator should be driven up to the nanowires' fundamental mechanical resonance frequency. This is estimated from classical beam theory as $(1/2\pi)\sqrt{32E/\rho}\,(w/L^2)$ ~5 and 7 MHz (where E and ρ are respectively Young's Modulus and density, taken as averages of silicon and

ITO values weighted for their relative thickness; *w* is the average width and *L* the length of the nanowires). In Figure 3.6 is presented the fast electro/optical response of the metamaterial.

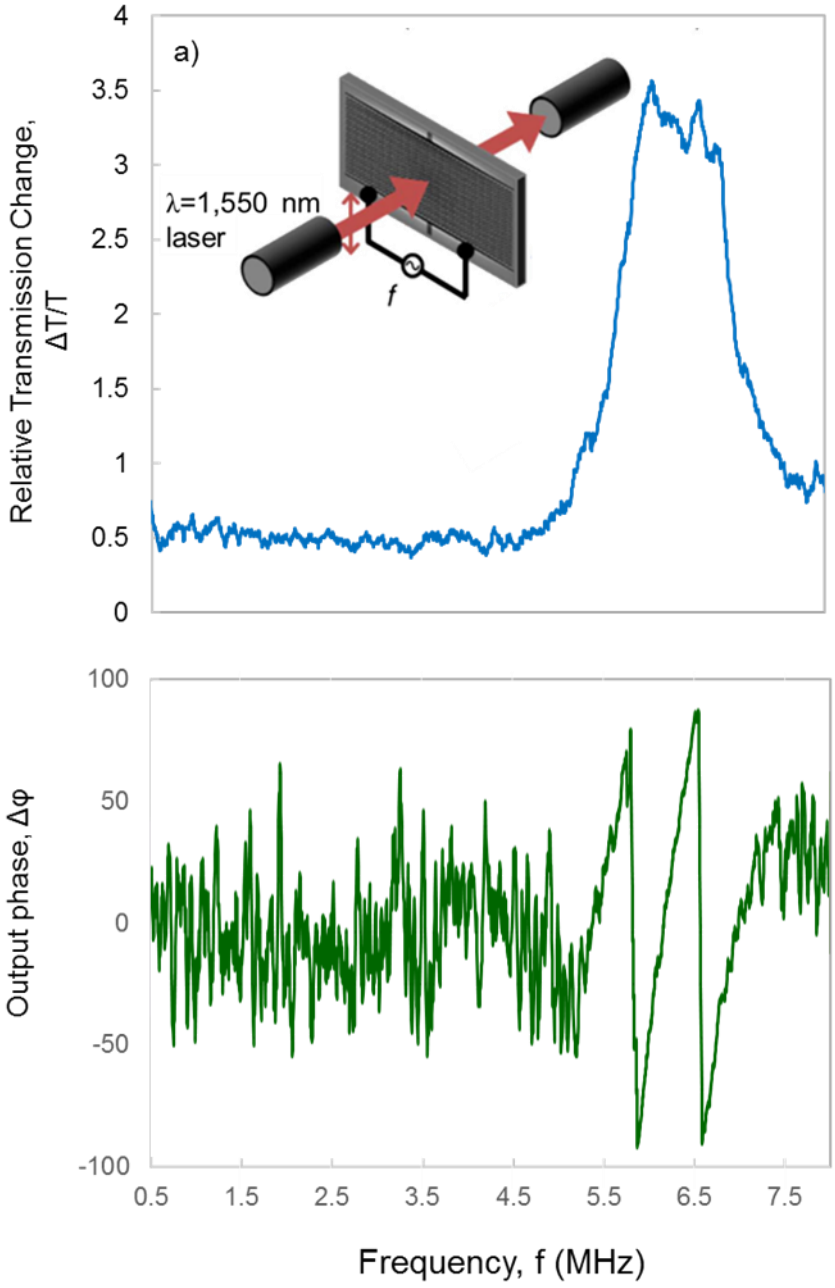

Figure 3.6 AC electro-optical modulation of Si/ITO metamaterial optical properties. a) Modulation of transmission with an external electrical control signal of amplitude A at different frequencies f. Transmission modulation is detected on the fundamental mechanical eigenfrequencies of Si/ITO nanowires. b) output phase change. Maximum amplitude of electrical input was 300mV.

Measurements realized in a Linkam stage with controllable pressure, around of few mbar. The metamaterial was driven electrically from the 1 port of a Vector Network Analyzer, while in the 2nd port was connected a fast photodetector to capture intensity changes of transmitted light. The peak in Figure 3.6a is quite broad, having a FWHM equal to 1 MHz. this is generally explained by two factors, 1st the mechanical eigenfrequency of its nano-beam is given from its

geometrical features. Due to fabrication imperfection, width of the beams varies by 10% for the smaller beams and less than 5% for the wider. 2nd due to moderate vaccum nano-mechanical resonantors should a damped harmonic oscillation. Futhermore heating or mechanical coupling might lead to out of plane displacement as well, with immediate results in the bandwidth of the mechanical resonance. The interesting features result from the phase difference recorder in the VNA. As any forced oscillator at the frequency of maximum amplitude is recorded as a phase shift. This is the case here, where phase shifts accur between 5.7 and 6.55 MHz close to mechanical eigenfrequencies of the Si/ITO nanobeams.

In summary, we have demonstrated a free-standing, all-dielectric metasurface electro-optic modulator of substantially sub-wavelength thickness ($<\lambda/10$), manufactured from CMOS-compatible (high-index low-loss semiconductor and transparent conductive oxide) materials, that provides continuous and reversible electrically-actuated nano-mechanical tuning of near-infrared reflectivity and transmission, in a wavelength band selected by design, at microwatt power levels. Electrostatic forces are harnessed to control the separation between elements of a non-diffractive Si/ITO nanowire array and so to deliver a transmission change of almost 10% at 1500-1600 nm under an applied bias of few volts and dynamic modulation of light up to 7MHz.

In facilitating electronic control over the spatial (re)configuration of all-dielectric metamaterials without detriment to the resonant optical properties or the intrinsic advantages over most plasmonic counterparts (i.e. in terms of absorption losses, operability in transmission mode and optical damage threshold), transparent conductive oxides open a path towards a variety of ultra-compact, active optoelectronic metadevices including tuneable filters, nonlinear elements, and adaptive ‘flat optical’ components.

3.2 Fiber-coupled nano-membrane electro-optical metamaterials

Optoelectronic integrated components that permit the electrical manipulation of light are of high interest. Several architectures have been proposed and used for this, such as Silicon photonic devices, [122] and VSCEL lasers [123] they have the potential to create compact fiber integrated, photonic micro-devices that benefit from fabrication experience developed across past years in CMOS (complementary metal-oxide semiconductor) electronics. Ultimately, the goal is the development of low-cost high-volume photonic integrated circuits (PICs) with integrated electronics, to simultaneously access the full potential of the silicon platform—i.e., Si-photonics for high-speed signaling and sensing, and CMOS-electronics for subsequent logical operations and computations.

Photonic nano-membrane metamaterials benefit from the fact that they can provide extreme nonlinearities in a subwavelength scale. Furthermore, it has been shown (in the previous chapter) that nano-mechanical electro/optical modulators can be made out of CMOS compatible media to achieve strong nonlinear responses. Here we present for first time a fiber integrated metasurface on fully encapsulated in a fiber environment, providing electro-optical modulation at the telecommunication wavelengths, 1310nm. Firstly the optical response of the all-dielectric nano-grating is tested both experimentally and with 3D finite element method numerical analysis. Then, we provide a general method for the encapsulation process with specific characteristics such as optical losses, beam diameter/profile and in the last part we

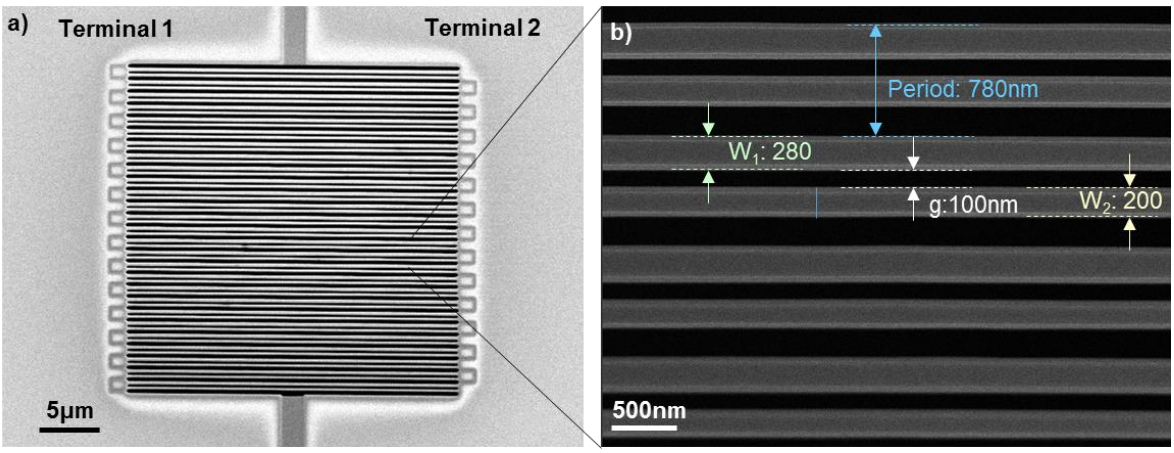

Figure 3.7 All-dielectric nano-mechanical metasurface. (a) Scanning electron microscope image of a free-standing nanowire array [top view] manufactured in a silicon/ITO bilayer membrane. (b) Close view, SEM image showing detail of the periodic arrangement of asymmetric nanowire pairs and the structure imposed at each end of the array where the ITO layer is selectively etched to electrically isolate pairs of nanowires. Dimensional schematic of the asymmetric Si/ITO nanowire pair within each period of the metasurface array [by design, P = 780,, w1 = 200, w2 = 280, g = 100 nm].

record around 0.25 dB contrast ratio between the voltage ON/OFF states actuated by a few volts, due to electrostatic actuation.

The metamaterial has been fabricated as described in Section 3.1. Here the difference in the thickness of the Silicon layer, is 140nm. This results in different optical response. The dimension of the metamaterial is explained in Figure 3.7.

Furthermore, the transmission spectrum is measured experimentally with a CraiC microspectrometer, (see appendix C for methods) and the optical response matches excellent with simulated spectra using a finite element method solver, COMSOL, (see Appendix D), and presented in figure 3.8.

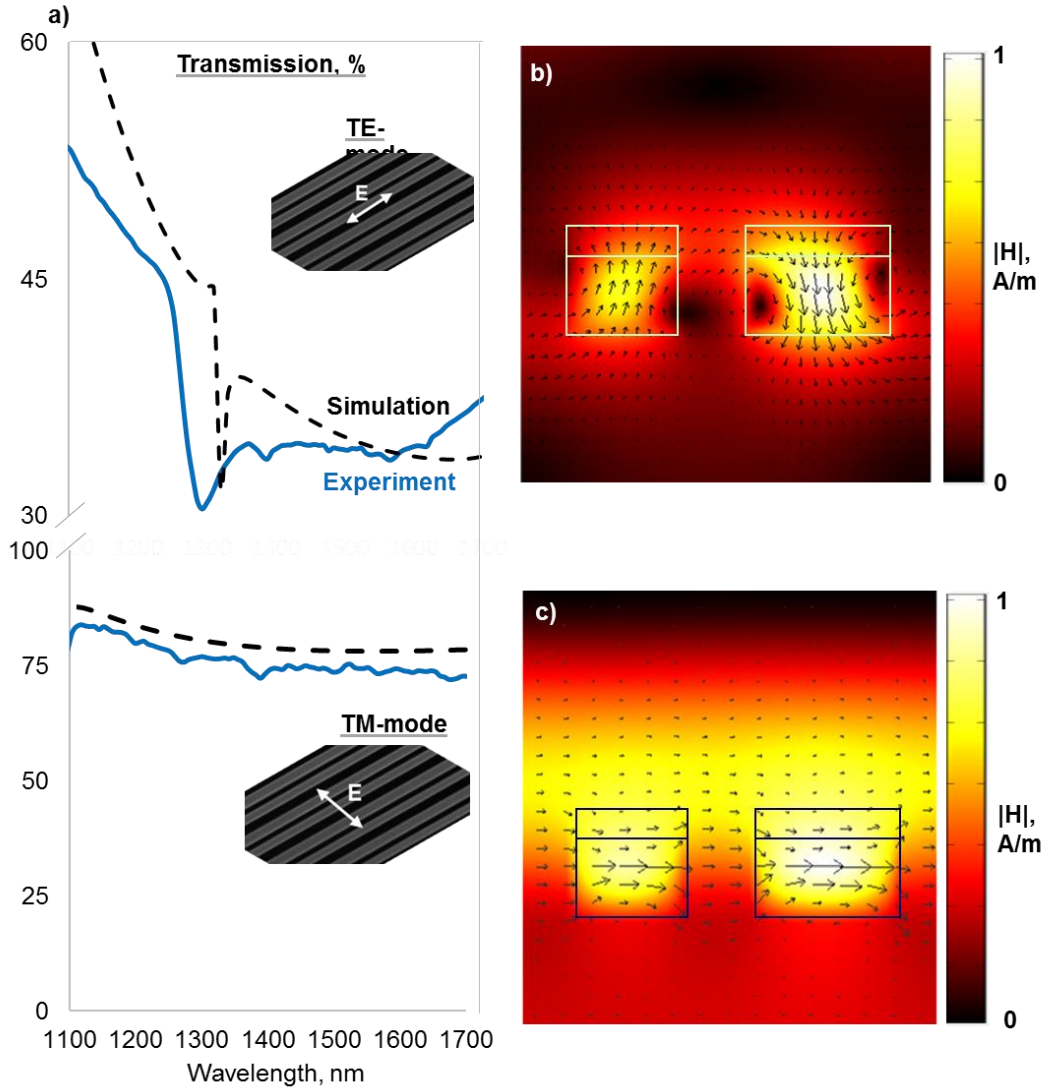

Figure 3.8 Si/ITO nanowire metasurface optical characterization. Microspectrophotometrically measured reflection and transmission spectra for the Si/ITO nanowire array shown in (a) for TE- and TM-polarized light, with corresponding Electric field maps for a single pair of wires, for TE (b) and TM (c), respectively. Simulated spectra, dashed black curves of the proposed structure have been plotted for comparison.

For the TE-mode, as defined in the inset of Figure 3.8 a) the resonant features in transmission spectra are recorded at the telecommunication wavelength of 1310nm. In this wavelength, the magnetic field circulation across every pair of this assymetric width grating result in a transmition dip. For the other polarization, TM-mode, magnetic field is trapped uniformly in both nano-wires, as a result a broad transmission is recorder in the whole NIR regime.

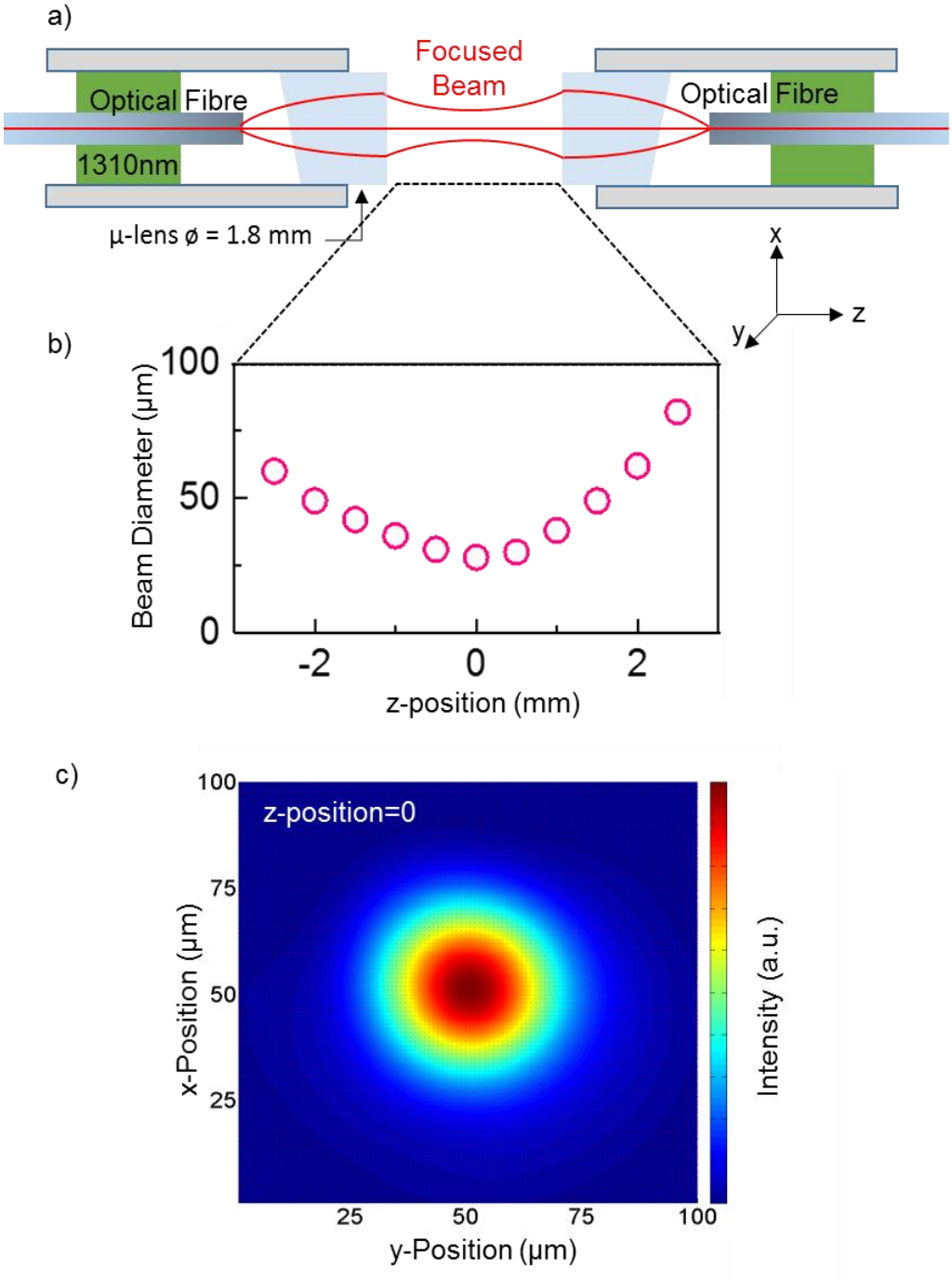

Figure 3.9 Light beam profile across two optical fibers. a) Skematic sketch of the alignment set-up. Two single mode, PM fibers used with a pair of microcollimators in order to focus and collect light, respectively. b) the beam diameter between the to collimators, which can reach 30μm. c) the intensity profile of the light beam at the position z=0, where the beam diameter is minimum.

We prepare an optical setup in collaboration with Dr. Yongmin Jung, where the nano-membrane can be embedded and aligned with the light beam. For this reason, we use a piezo stage to align to single mode fibres operating at 1310nm. They maintain polarization of the out- put laser source, panda style. In order to create a focused beam between the two fibers, we position a μ-lens which dependently on the distance from the facet of the fiber can either create a focused or collimated beam. The alignment setup is presented in Figure 3.9. by positioning a CMOS camera between the two fibers we record the position of the minimum beam spot and define this as zero position. Then for the position we use a piezo stage and we record the power recorded for several position of the single mode fiber in order to reproduce the optical profile of the light beam as presented in figure 3.9c.

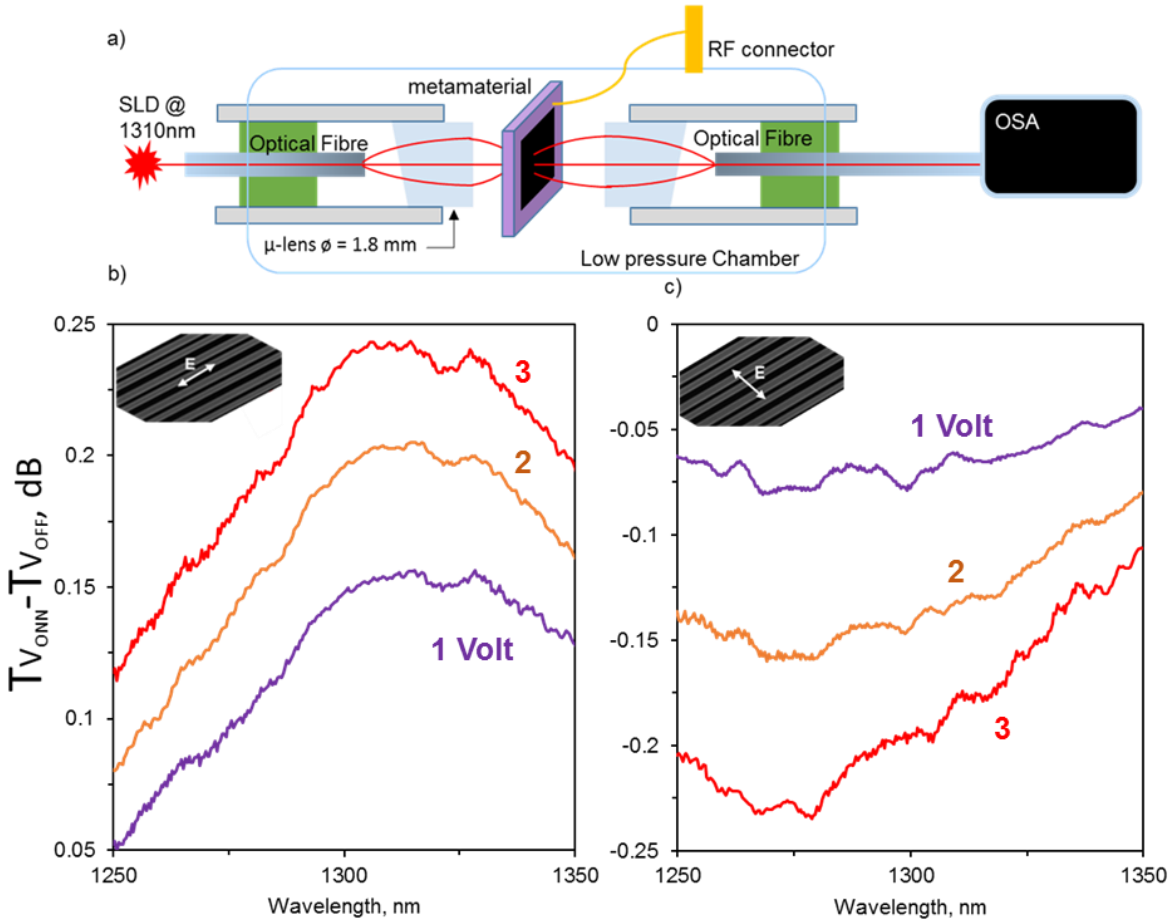

Figure 3.10 DC electro-optical modulation of a Si/ITO nanowire metasurface. a) Skematic sketch of the experimental setup used to control optical properties of a dielectric metamaterial electrically. transmission difference for voltage ON and OFF state, for b) TE and c) TM mode of a laser at 1310nm.

Next we test the electro-optic response of the encapsulated metamaterial. For this we use the setup described in figure 3.9 and intersect the silicon/ITO metamaterial described previously. An RF connector is used to electrically actuate the two terminals. The response recorded is illustrated in figure 3.10. a superluminescent diode laser, (SLD) was used with central

wavelength of 1310nm and bandwidth of 80nm. We align our polarization and we test first the TE-mode were a maximum of 0.25dB is measured. The positive sign of the difference reveals that transmission is getting larger after the application of a few volts. This can be understood from the fact that as the nano-beams bend towards each other the uniformity of the sample breaks so the resonant deep no longer exists. In the other polarization an opposite change is recorded where we have a negative change in transmission after application of electric signal. This means that as the beams bend they destroy the characteristic plateau formed in the Figure 3.8 a). The changes in the output light have been recorded in an optical spectrum analyzer.

Overall the performance of an all-dielectric electro-optical nano-mechanical metamaterial has been tested. A new method has been proposed for the integration of nano-membrane metamaterials in a fiber environment, while this work opens the way for the integration of the general family of structurally reconfigurable metamaterials in fiber platforms.

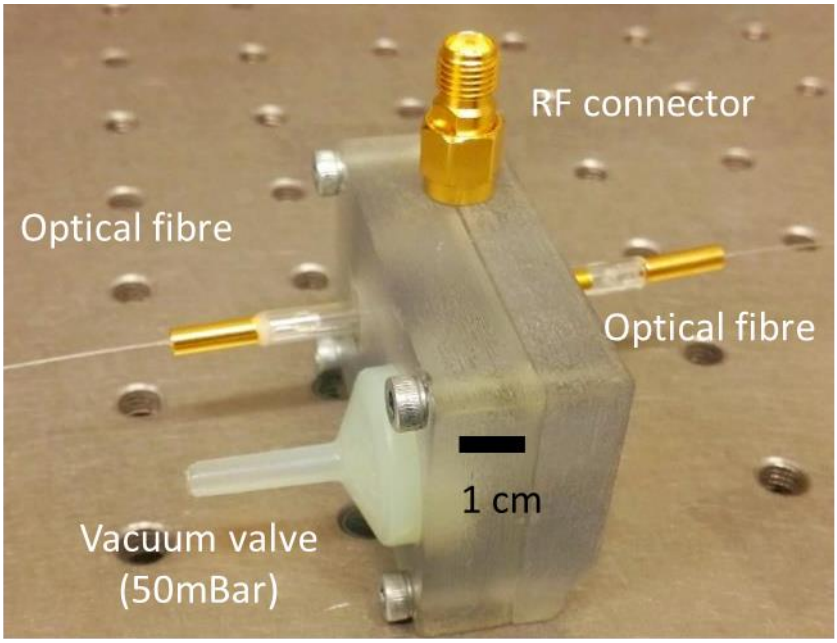

Figure 3.11 Fiber-coupled nano-membrane electro-optical metamaterial.
Final device with electric contacts for electro-optical modulation, vaccum sealed for avoid contamination and increase performance of device.

Chapter 4

Reconfigurable Phase Change Metamaterials

Phase-change materials exhibit fast and reversible transitions between an amorphous and a crystalline state. The two states display resistivity and refractive index contrast, which is exploited in phase-change optoelectronic memory devices.[74], [124] The most important family of phase-change materials consists of Ge-Sb-Te alloys, given their high melting temperature (600^{o}C) and phase transition temperature around 160^{o}C. Depending on the regime of excitation, one can obtain either reversible or irreversible phase changes. Continuous and reversible changes occur through the intermediate coexistence of phases, and are suitable for controlling light with light. An example of this physical mechanism is explained in Figure 4.1, adopted from [124].

In the rest of this chapter I benefit from this mechanism to provide reconfigurable phase change metamaterials, operating in visible and near infrared regime, with strong

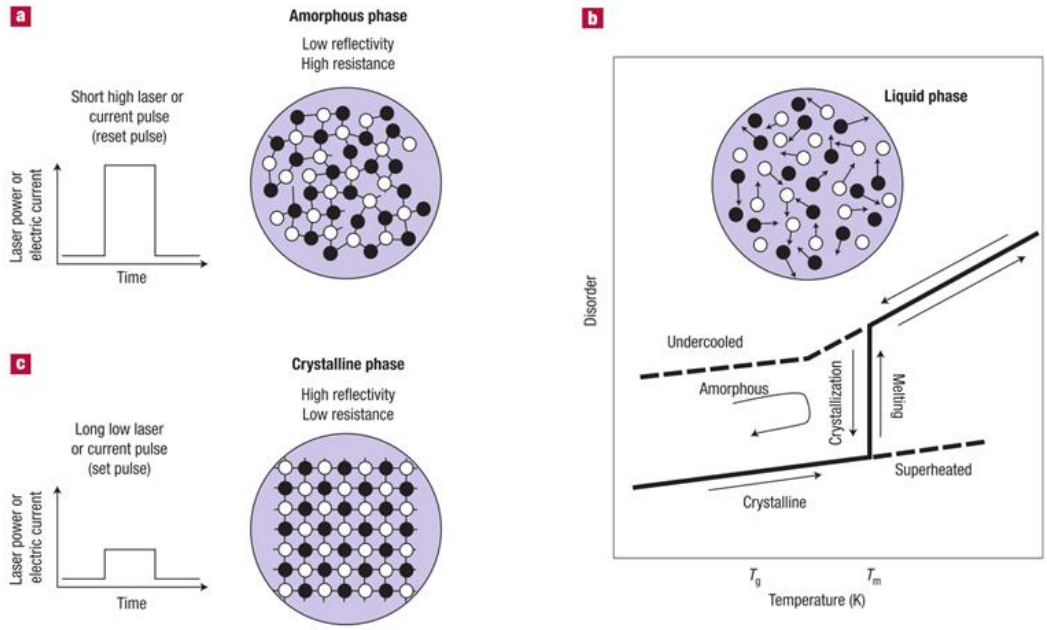

Figure 4.1 Rewriteable optical data storage using phase-change materials. a, A short pulse of a focused, high-intensity laser beam locally heats the phase-change material above its melting temperature. b, Rapidly cooling the alloy at rates higher than 109 K s^{-1} quenches the liquid-like state into a disordered, amorphous phase. This amorphous state has different optical properties from the surrounding crystalline state, so detecting amorphous regions is straightforward with a low-intensity laser beam. c, To erase the stored information a laser pulse with intermediate power is used. The laser locally heats the phase-change film above the crystallization temperature. At temperatures above T_g the atoms become increasingly mobile and can revert to the energetically favourable crystalline state, erasing the recorded information. [124]

Transmission/Reflection contrast between amorphous and crystalline states of chalcogenide metamaterials. Reversibility of switching of the proposed devices was feasible only after the use of a capping layer, which is appropriate to protect the metamaterials' shape during the quenching process. The thin film deposition of the chalcogenide glasses have been performed by Dr Behrad Gholipour as well as the ultrafast reversible switching.

4.1 All-dielectric phase-change reconfigurable metasurfaces

From their emergence as a paradigm for engineering new passive electromagnetic properties such as negative refractive index or perfect absorption, metamaterial concepts have extended rapidly to include a wealth of dynamic - switchable, tunable, reconfigurable, and nonlinear optical functionalities, typically through the hybridization of plasmonic (noble metal) metamaterials/surfaces with active media. [62] Phase-change materials, including chalcogenides,[113], [125]–[127] vanadium dioxide, [73], [114], [128] gallium, [115] and liquid crystals [116], [129], [130] have featured prominently in this evolution. We now show that the chalcogenides offer a uniquely flexible platform for the realization of non-volatile, optically-switchable all-dielectric metamaterials. Subwavelength-thickness germanium antimony telluride (GST) nano-grating metasurfaces provide high-quality ($Q \geq 20$) near-infrared resonances that can be spectrally shifted by optically-induced crystallization to deliver reflection and transmission switching contrast ratios up to 5:1 (7 dB).

To mitigate the substantial Ohmic losses encountered in plasmonic metamaterials at optical frequencies, which compromise many applications, while also improving manufacturing process practicality and compatibility with established (opto)electronic technologies, considerable effort has been devoted of late to the realization of 'all-dielectric' metamaterials, presenting resonances based upon the excitation of Mie as opposed to plasmonic (displacement as opposed to conduction current) modes in high-index, low-loss dielectric as opposed to noble metal nanostructures. A wide range of passive all-dielectric metasurface planar optical elements for steering, splitting, filtering, focusing and variously manipulating beams have been demonstrated, very typically using silicon for visible to near-IR wavelengths.[36], [37], [39], [41], [93]Active functionalities have been demonstrated on the basis of hybridization of a silicon metasurface with a liquid crystal, [82] two photon absorption on silicon metasurfaces [43], [117] and nonlinear optomechanical reconfiguration in a free-standing silicon membrane metasurface. [118]

By virtue of their compositionally-controlled high-index, low-loss characteristics, which extend over a broad spectral range from the visible to long-wave infrared, and which moreover can be reversibly switched (electrically or optically) in a non-volatile fashion, the chalcogenides (binary and ternary sulphides, selenides and tellurides) provide an exceptionally adaptable material base for the realization of optically reconfigurable meta-devices. Their phase-change properties – reversible transitions between amorphous and crystalline states with markedly different optical and electronic properties – have been utilized for decades in optical data storage and more recently in electronic phase-change RAM. [124] The crystalline-to-amorphous transition is a melt-quenching process initiated by a short (few ns or less), intense excitation that momentarily raises the local temperature above the melting point T_m; the amorphous-to-crystalline transition is an annealing process requiring a longer (sub-μs), lower intensity excitation to hold the material above its glass transition temperature T_g (but below

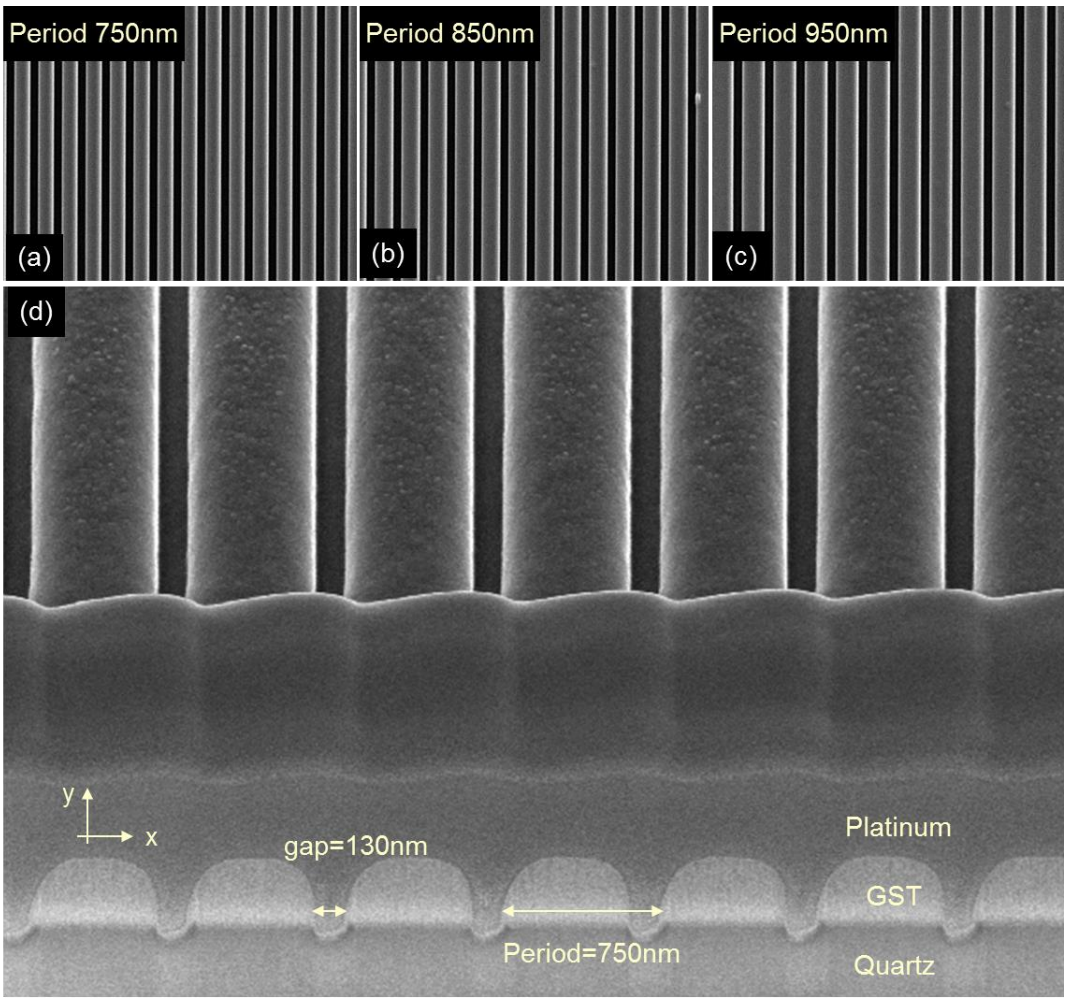

Figure 4.2 All-chalcogenide nano-grating metasurfaces. (a,b,c) Oblique incidence SEM image of the proposed samples for 3 different periods and (d) cross-sectional scanning electron microscope images of a 750 nm period grating fabricated by focused ion beam milling in a 300 nm thick amorphous GST film on silica.

Tm) for a short time. The latter can also be achieved through an accumulation of sub-threshold (including fs laser pulse) excitations, facilitating reproducible ‘greyscale’ and neuromorphic switching modes of interest for all-optical data and image processing, and harnessed recently for direct, reversible laser writing of planar optical elements and short/mid-wave IR metamaterials in a chalcogenide thin film. [55], [131]–[133]

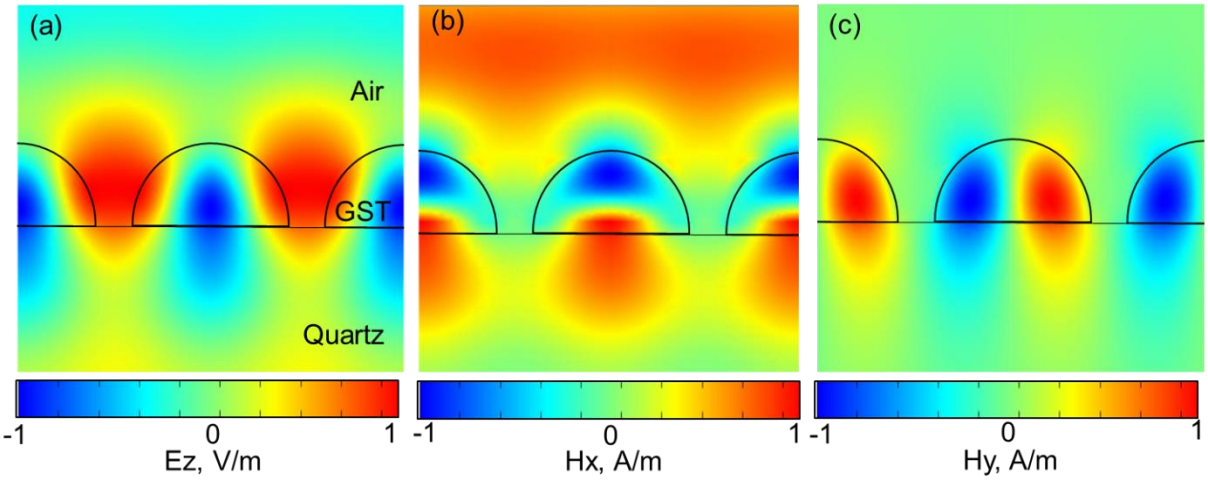

Figure 4.3 All-chalcogenide nano-grating metasurfaces optical response. Simulated response of the near electric (a) and magnetic (b,c) field distribution for the resonant wavelength for linearly polarized light parallel to the nanowires, TE mode. On resonance, antiparrallel displacement currents within the centre and peripheral of each nano-wires run while for the magnetic component a circulation within each nanowire takes place.

Here, we demonstrate structurally engineered high-quality near-infrared transmission and reflection resonances in planar (300 nm thick) dielectric nano-grating metasurfaces of amorphous germanium antimony telluride (Ge2Sb2Te5 or GST - a widely used composition in data storage applications), and the non-volatile switching of these resonances via laser-induced crystallization of the chalcogenide. We employ nano-grating array metasurface patterns of subwavelength periodicity (Figure 4.2), similar to those used, for example, in demonstrations of active nanophotonic photodetectors and tunable filters. [134]–[136] A thin (subwavelength) film of a transparent medium at normal incidence has properties of reflection and transmission dependent on its thickness and complex refractive index. Periodically structuring such a film on the subwavelength scale has the effect of introducing narrow reflection/transmission resonances via the interaction between thin film interference and grating mode. [137], [138] Such structures are non-diffractive and thus behave in the far field as homogenous layers. [139] In the case of anisotropic structuring, the resultant optical properties are dependent on the polarization of incident light.

GST films with a thickness of 300 nm were deposited on optically flat quartz substrates by RF sputtering (Kurt J. Lesker Nano 38). A base pressure of 5×10-5 mbar is achieved prior to deposition and high-purity argon is used as the sputtering gas (70 ccpm to strike, 37 ccpm to maintain the plasma). The substrate is held within 10K of room temperature on a rotating platen 150 mm from the target to produce low-stress amorphous films. Nano-grating metasurface patterns, with a fixed slot width s ~130 nm and periods P from 750 to 950 nm, each covering

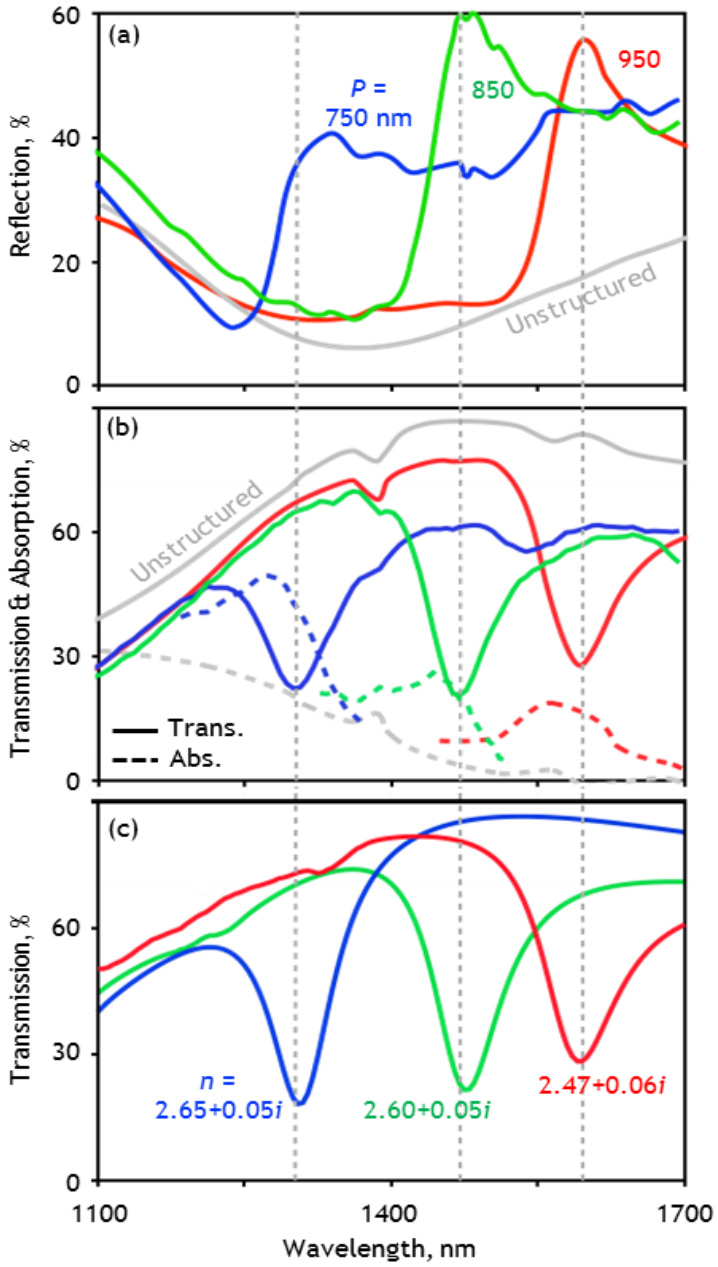

Figure 4.4 GST nano-grating optical spectra. (a, b) Microspectrophotometrically measured Reflection *R*, transmission *T* and absorption *A* [*=1-{R+T}*] spectra for 300 nm thick amorphous GST nano-grating metamaterials with a selection of periods *P* [as labelled; slot width *s* = 130 nm], under TE-polarized illumination, alongside spectra for the unstructured amorphous GST film. (c) Numerically simulated transmission spectra calculated using a non-dispersive GST refractive index value for each grating period [as labelled] selected to reproduce experimental resonance positions and widths.

an area of approximately 20 μm × 20 μm, were etched through the GST layer by focused ion beam (FIB) milling (Fig. 1). The normal-incidence transmission and reflection characteristics of these GST nano-grating metasurfaces were subsequently quantified, for incident polarizations parallel and perpendicular to the grating lines (along the y and x directions defined in Figure 4.4 (a) and (b), or TE and TM orientations of the grating, respectively). This measurement performed by a microspectrophotometer (CRAIC QDI2010) with a sampling domain size of 15 μm × 15 μm, (see Appendix C for more details).

Unstructured, amorphous GST is broadly transparent in the near-IR range, with measured transmission at a thickness of 300 nm >70% between 1300 and 1800 nm (Figure 4.3); absorption being <20% in this spectral range (<1% above 1500 nm). Nano-grating metasurface structures introduce pronounced resonances, with quality factors Q more than 20 ($Q = \lambda r/\Delta\lambda$ where λr is the resonance frequency and $\Delta\lambda$ is the half-maximum linewidth), for TE polarized light, as shown in Figures 4.4a and 4.4b, at spectral positions directly proportional to the nano-grating period P.

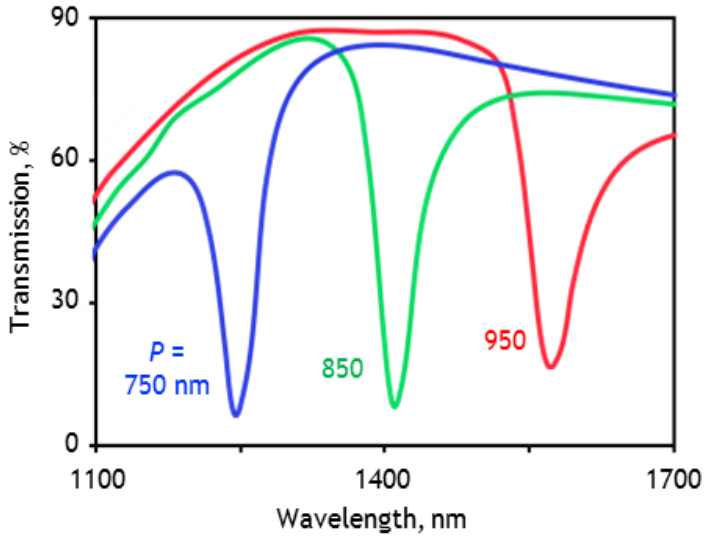

Figure 4.5 Numerically simulated transmission spectra for 300 nm thick amorphous GST nano-grating metamaterials with a selection of periods [as labelled; slot width *s* = 130 nm], under TE-polarized illumination, calculated using ellipsometircally measured values for the [weakly dispersive] complex refractive index of unstructured amorphous GST.

This behavior is replicated in three-dimensional finite element (Comsol MultiPhysics) numerical simulations. These assume in all cases a lossless non-dispersive refractive index of 1.46 for the silica substrate, normally incident narrowband plane wave illumination and, by virtue of periodic boundary conditions, a grating pattern of infinite extent in the x-y plane. Using in the first instance ellipsometrically obtained values for the complex refractive index of the unstructured amorphous GST film (Figure 4.6), which has a weakly dispersive real part

~2.5 (decreasing slowly with increasing wavelength from 2.6 to 2.4 between 1000 and 1700 nm) and a loss coefficient <0.045 across most of the near-IR spectral range (rising below 1130 nm to reach 0.09 at 1000 nm), a good qualitative match is obtained, albeit with values of Q >30, (Figure 4.5.)

Using instead the real and imaginary parts of GST refractive index as free parameters in the model, an improved match to the experimentally observed spectral positions and widths of nano-grating resonances is achieved with non-dispersive refractive index values for each grating period (as shown in Fig. 4.4c) that are marginally higher in both the real and imaginary part than the ellipsometry values at the corresponding resonant wavelength. The discrepancies between ellipsometry and experimental/fitted spectra are related to manufacturing imperfections, i.e. deviations from the ideal model geometry such as slight over-milling of grating lines into the substrate, and to contamination / stoichiometric change in the GST during FIB milling, which effects some change in refractive index.

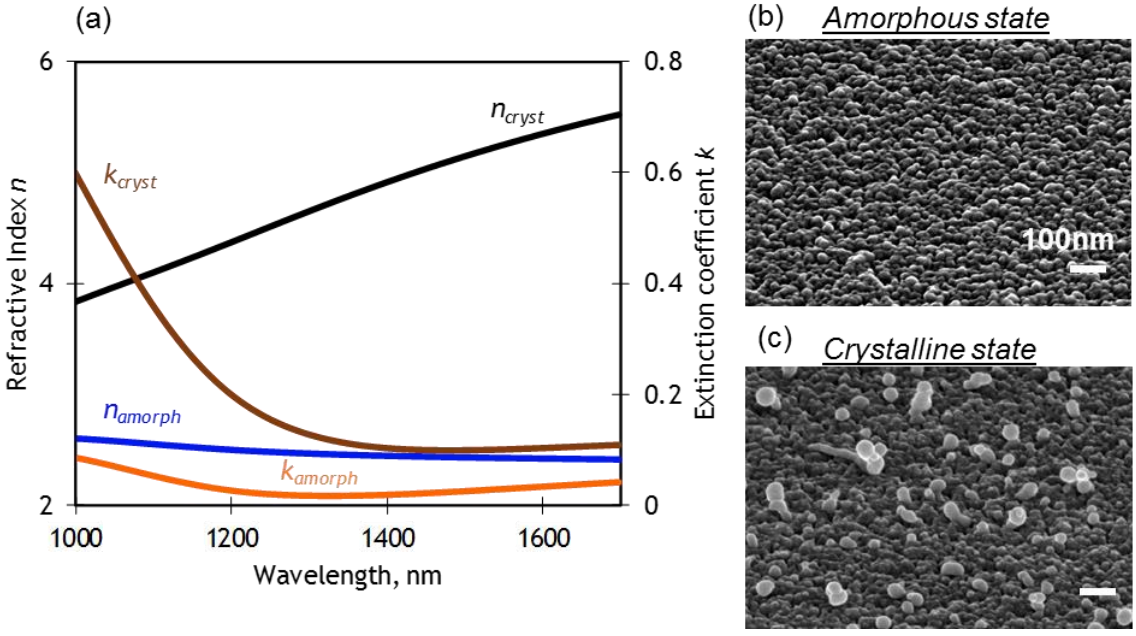

Figure 4.6 Near-IR dispersion of complex refractive indices of GST. from spectroscopic ellipsometry. of the as-deposited amorphous and laser-annealed crystalline phases of a 300 nm thick unstructured Ge:Sb:Te film on silica.

The simulations show that the TE resonance is associated with the excitation of anti-phased displacement currents (in the ±y direction) along the core and sides of each GST 'nanowire', and a circulating pattern of magnetic field centered within the wire as illustrated in Fig. 4.3. For the orthogonal TM polarization, the spectral dispersion of reflectivity and transmission (as measured by the microspectrophotometer, which employs an objective of numerical aperture

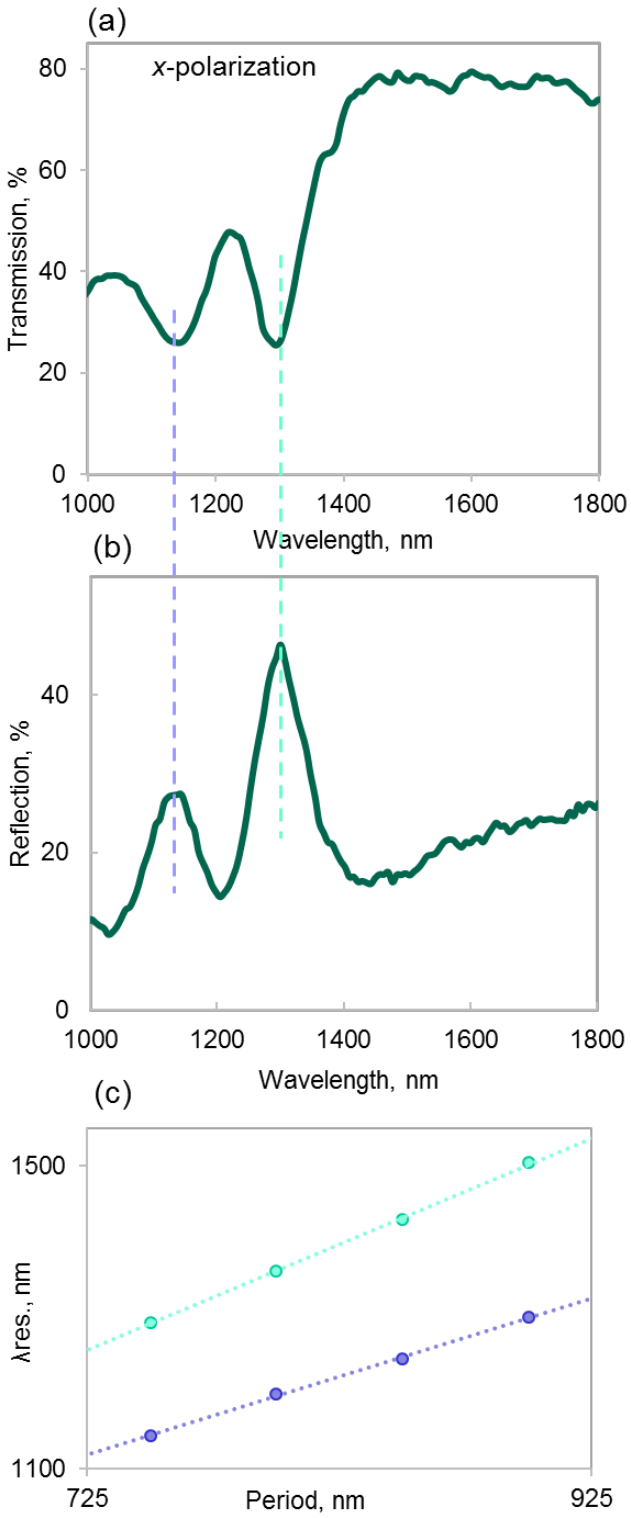

Figure 4.7 Effect of near normal incident light in a nano-grating.a) Microspectrophotometrically measured reflection and transmission spectra for a 300 nm thick amorphous GST nano-grating metamaterial with a period P = 750 nm [slot width s = 130 nm], under TM-polarized illumination.

0.28) is more complex. Resonances, again at wavelengths proportional to P, are split as a result of the structures' sensitivity in this orientation to the incident angle of light (see Figure 4.7). Under TM-polarized illumination nano-grating resonances are split as a result of the structures' strong sensitivity in this orientation to the incident angle of light: The microspectrophotometer

employs an objective with a numerical aperture of 0.28, thereby illuminating samples at incident angles θ ranging from zero to ~16°. This is of little consequence to the TE mode (experimental data are reproduced well by numerical simulations assuming ideally normal incidence), but for the TM polarization spatial symmetry is broken by the slightest deviation from normal incidence, leading to the observed resonance splitting. [134], [140] The TM resonances are characterized by displacement currents circulating in the xz plane (forming magnetic dipoles oriented along y) – a single symmetric loop centered within each nanowire at singularly normal incidence, θ = 0°; more complex asymmetric double-circulated distributions at off-normal angles (see Figure 4.8).

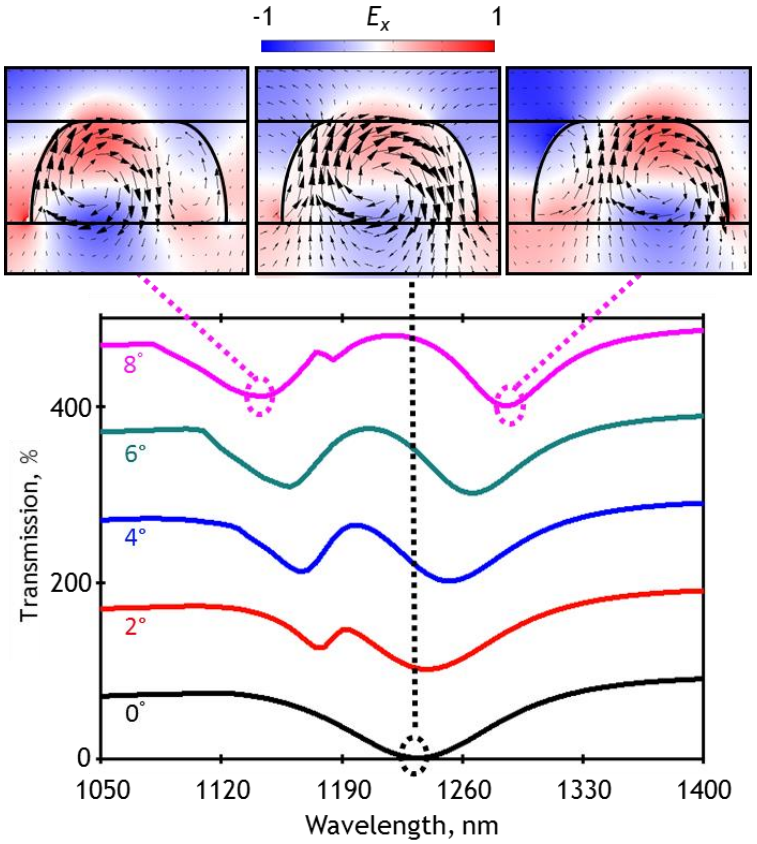

Figure 4.8 Effect of near normal incident light in a nano-grating.a) Microspectrophotometrically measured reflection and transmission spectra for a 300 nm thick amorphous GST nano-grating metamaterial with a period P = 750 nm [slot width s = 130 nm], under TM-polarized illumination. b) Numerically simulated TM-mode transmission spectra for a 300 nm thick GST nano-grating metamaterial, with a period P = 750 nm and slot width at the lower and upper surfaces of the GST layer of 130 and 450 nm respectively, for incident angles between 0º and 8º [as labelled; vertically offset for clarity]. Field maps above show the distribution of the x-component of electric field in the *xz* plane for a unit cell of the metasurface at the singular normal incidence resonance [λ = 1235 nm] and the two minima [= 1145 and 1285 nm] of the split resonance for an incident angle of 8º.

By engaging the phase-change properties of GST, [124] the resonances of all-chalcogenide metasurfaces can be optically switched in a non-volatile fashion. In the present case, GST nano-gratings are converted from the as-deposited amorphous phase to a crystalline state by laser

excitation at a wavelength of 532 nm (selected for its strong absorption in GST). This annealing is achieved by raster-scanning the beam, with a spot diameter of ~5 μm and continuous wave intensity of ~3 mW/μm2, over the sample to bring the GST momentarily to a temperature above its glass-transition point Tg but below its melting point Tm (around 110 and 630°C respectively, [141], [142] though exact values will vary with factors including film thickness, composition and density). The resultant change in GST's complex refractive index produces a change in the spectral dispersion of the nano-grating resonances, bringing about substantial changes in the metasurface transmission and reflection, especially at wavelengths close to the resonance – absolute levels are seen to increase/decrease by as much as a factor of five (Figure

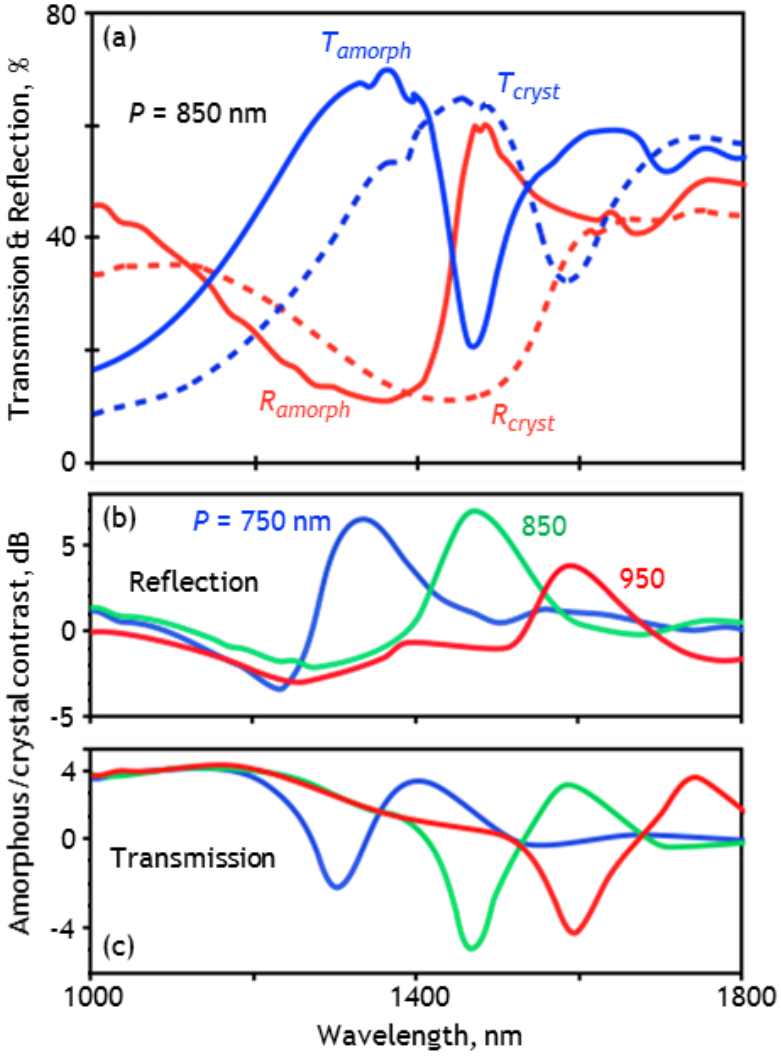

Figure 4.9 Reconfigurable optical response of GST nano-gratings. (a) Microspectrophotometrically measured TE-mode reflectivity and transmission spectra for the as-deposited amorphous and laser-annealed [partially] crystalline phases of a 300 nm thick GST nano-grating metamaterial with a period P = 850 nm [slot width s = 130 nm]. (b, c) Spectral dispersion of TE-mode reflection (b) and transmission (c) switching contrast, evaluated as $10log(A/C)$ where A and C are respectively the amorphous and crystalline levels, for a selection of GST nano-grating periods [as labelled].

4.9). An increase in the real part of the GST refractive index red-shifts metasurface resonances by approximately 150 nm, while the concomitant increase in the imaginary part of the index is primarily responsible for increasing the resonance linewidth and broadband (non-resonant) absorption, particularly at shorter wavelengths.

Repeating the above process of matching numerically modelled spectra to experimentally observed nano-grating resonance positions and widths yields (for all three grating periods, again under the non-dispersive approximation) a refractive index value of 2.85 + 0.09i for the laser-annealed GST in the nano-gratings (see Figure 4.10). The induced index change of ~10% is substantial but yet smaller and less wavelength-dependent than may be expected on the basis of ellipsometric data for unstructured crystalline GST, see Figure 4.6. This indicates strongly that the nanostructured GST is stoichiometrically modified and/or only partially crystallized, [127], [143], [144] which is to be anticipated primarily as a consequence of the FIB milling process (reduction of refractive index due to irradiation, [145] creation of defects and gallium implantation) and because nanostructuring unavoidably modifies the thermal properties of the film (i.e. the energy absorbed from the laser beam at a given point; the temperature achieved; and the rates of temperature increase/decrease). Nonetheless, the refractive index change (resonance spectral shift) achieved experimentally may be considered close to optimal in that it maximizes transmission and reflectivity contrast. For example, the 1470 nm reflectivity maximum of the amorphous 850 nm period grating becomes a reflectivity minimum in the (partially) crystalline state, giving a contrast ratio (Ramorphous:Rcrystalline) of 5:1 (7 dB).

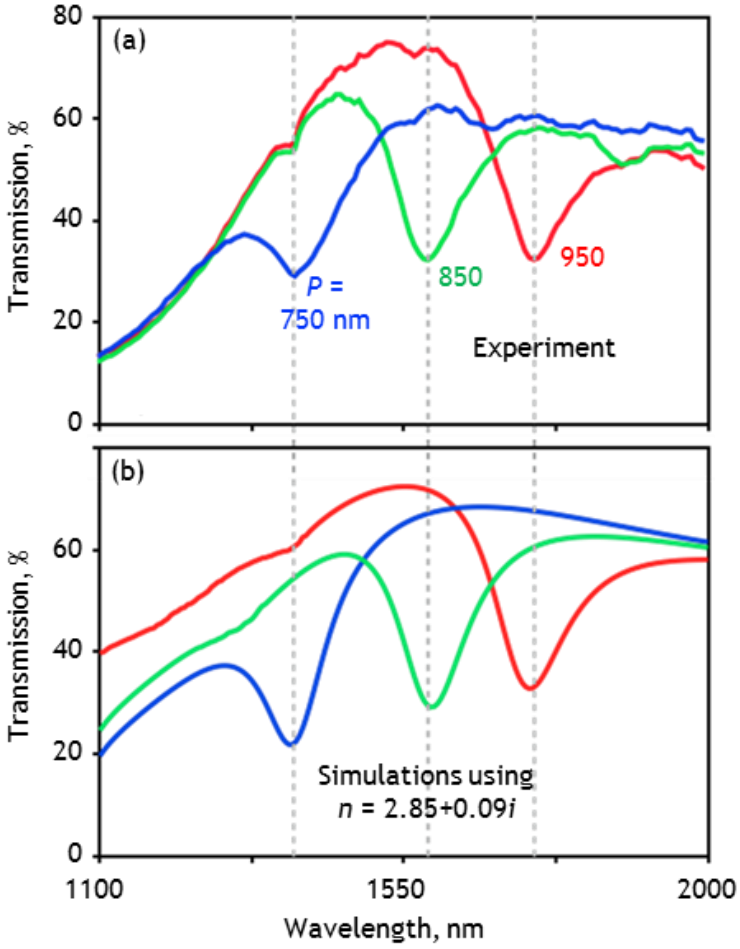

Figure 4.10 Crystalline GST nanoo-grating spectra & simulation. (a) Microspectrophotometrically measured transmission spectra for 300 nm thick laser-annealed [partially] crystalline GST nano-grating metamaterials with a selection of periods *P* [as labelled; slot width *s* = 130 nm], under TE-polarized illumination. (b) Corresponding numerically simulated transmission spectra calculated using a non-dispersive GST refractive index value of 2.85 + 0.09*i* that reproduces the experimental resonance positions and widths for all grating periods.

The reverse crystalline-to-amorphous transition is not demonstrated as part of the present study: This melt-quench process would require transient heating of the GST to a temperature above Tm, which would lead to geometric deformation and chemical degradation of the samples. Robust metasurfaces supporting reversible switching over many cycles may be realized by encapsulating the GST nanostructure in the manner of the functional chalcogenide layers within rewritable optical discs, which are located between protective layers of ZnS:SiO_2. In this regard, all-chalcogenide metasurfaces hold a notable advantage over hybrid plasmonic-metal/chalcogenide metamaterials,[113], [125]–[127] which ultimately require similar passivation layers (and thereby inevitably sacrifice switching contrast due the separation necessarily introduced between the active chalcogenide component and the surface, i.e. optical near-field, of the plasmonic metal). All-chalcogenide metasurfaces can also offer lower

insertion losses and greater ease of fabrication (via a single lithographic step in a single layer of CMOS-compatible material) than plasmonic hybrid structures.

In summary, we have realized all-dielectric photonic metasurfaces using a chalcogenide phase-change material platform, and demonstrated high-contrast, non-volatile, optically-induced switching of their near-infrared resonant reflectivity and transmission characteristics. Subwavelength (300 nm; $<\lambda/5$) films of germanium antimony telluride (GST) structured with non-diffractive sub-wavelength grating patterns, present high-quality resonances that are spectrally shifted by as much as 10% as a consequence of a laser-induced (amorphous-crystalline) structural transitions in the GST, providing switching contrast ratios of up to 5:1 (7 dB) in reflection and 1:3 (-5 dB) in transmission.

Within the transparency range of the (unstructured) host medium, high switching contrast wavebands can be engineered by design, i.e. appropriate selection of metasurface pattern geometry and dimensions. GST – a material with an established industrial footprint in optical and electronic data storage, can readily be structured for telecommunications applications at 1550 nm, while other members of the extensive (sulphide, selenide and telluride) chalcogenide family may also provide similar active, all-dielectric metasurface functionality in the visible range and at infrared wavelengths out to 20 μm.

Among material platforms for all-dielectric metamaterials, chalcogenides offer a unique compositional variety (i.e. range and variability of material parameters) and non-volatile (including binary [124] as well as incremental 'greyscale' [131]) switching functionality. A wealth of reconfigurable and self-adaptive subwavelength-thickness 'flat-optic' applications may be envisaged, including switchable/tunable bandpass filter, lens, beam deflection and optical limiting components. It is interesting to note that the GST metasurfaces' resonant reflectivity and transmission changes occur in the opposite direction to those in the unstructured chalcogenide (e.g. crystallization increases the reflectivity of an unstructured film but decreases that of a nano-grating at resonance). The ability of a single medium to provide both high and low reflectivity/transmission (signal on and off) levels in the same phase state, such that they can be simultaneously inverted via a homogenous, sample-wide structural transition, may be of interest in image processing as well as the above metasurface optics applications.

4.2 Phase-Change-Driven Plasmonic-Dielectric Transitions in Colour tunable Chalcogenide Metasurfaces

Chalcogenides – alloys based upon group-16 'chalcogen' elements (sulfur, selenium and tellurium) covalently bound to 'network formers' such as arsenic, germanium, antimony and gallium – present a variety of technologically useful properties, from infrared transparency and high optical nonlinearity to photorefractivity and readily-induced, reversible non-volatile structural phase switching. It has gone largely unnoticed however, that some chalcogenides accrue plasmonic properties in the transition from an amorphous to a crystalline state, i.e. the real part of their relative permittivity becomes negative. Indeed, one of the most commercially important chalcogenide compounds, germanium antimony telluride (Ge:Sb:Te or GST), which is widely used in rewritable optical and electronic data storage technologies, presents exactly this behavior at wavelengths in the near-ultraviolet to visible spectral range. In this work we show that the phase transition-induced emergence of plasmonic properties in the crystalline state can markedly change the optical properties of subwavelength-thickness nanostructured GST films, providing for the realization of non-volatile, reconfigurable (e.g. color-tunable) chalcogenide metasurfaces operating at visible frequencies, and thus creating opportunities for developments in non-volatile optical memory, solid state displays and all-optical switching devices.

Phase-change materials have played a significant role in the evolution of active plasmonic and photonic metamaterial technologies, delivering a variety of switchable, tunable, and reconfigurable optical functionalities through hybridization with plasmonic metal nanostructures [73], [113], [114], [146]–[149]. Chalcogenides in particular, which can be electrically and optically switched between amorphous and crystalline states with markedly different electronic and photonic properties, have facilitated the realization of active plasmonic metamaterial devices for a variety of applications including electro- and all-optical signal switching, polarization modulation, beam steering, and multispectral imaging [125]–[127], [150], [151]. Moreover, the near-infrared high refractive index and index contrast between phase states on GST have recently been harnessed in the demonstration of laser-rewritable and optically switchable nanostructured 'all-dielectric' (i.e. all-chalcogenide) metasurfaces. [55], [119]

Here we show that thin film GST can be optically switched between amorphous and polycrystalline states which, at UV/VIS wavelengths, are respectively dielectric and metallic (i.e. plasmonic), and demonstrate this in the context of switchable photonic metasurfaces. The

real part ε_1 of relative permittivity (Figure 4.11a) for polycrystalline GST has a negative value, as is required for a medium in air/vacuum to support surface plasmons [18], at wavelengths λ below 660 nm, and a positive value at longer wavelengths. In contrast, amorphous GST is a dielectric, with a positive value of $\varepsilon 1$, across the entire ultraviolet to near-infrared spectral range. Figure 4.11b presents the plasmonic figure of merit $Re\{k_{SPP}\}/2\pi Im\{k_{SPP}\}$– the surface plasmon polartiton (SPP) propagation decay length in units of SPP wavelength [152] – for polycrystalline GST alongside a number of other, noble metal and recently-proposed alternative[24], plasmonic media. $k_{SPP} = k_{spp} = k_0\sqrt{\varepsilon_m\varepsilon_d/(\varepsilon_m + \varepsilon_d)}$ being the wavevector of surface plasmon polaritons on a planar interface between metallic and dielectric media with complex relative permittivities εm and εd respectively; The latter is taken to be air in the present case; k_0 is the free space wavevector.) On this basis, GST is comparable to most other materials in the UV-to-blue/green visible wavelength range, and almost as good a plasmonic medium in this spectral band as highly-doped transparent conductive oxides are at near-infrared wavelengths.

Here, we show that the chalcogenide alloy germanium antimony telluride (GST) – which has been widely used as the functional basis of rewritable optical disk and electronic phase-change RAM technologies over many decades – can be converted between amorphous and crystalline states that are respectively, at UV/VIS frequencies, dielectric and metallic (i.e. plasmonic). The amorphous-to-crystalline transition, which changes the sign of the real part of the material's relative permittivity (ε_1) from positive to negative (Fig. 4.11a), is an annealing process. This process may be initiated either by heating or by pulsed laser or electronic excitation, bringing the chalcogenide to a temperature above its glass-transition point T_g (around 160°C) but below

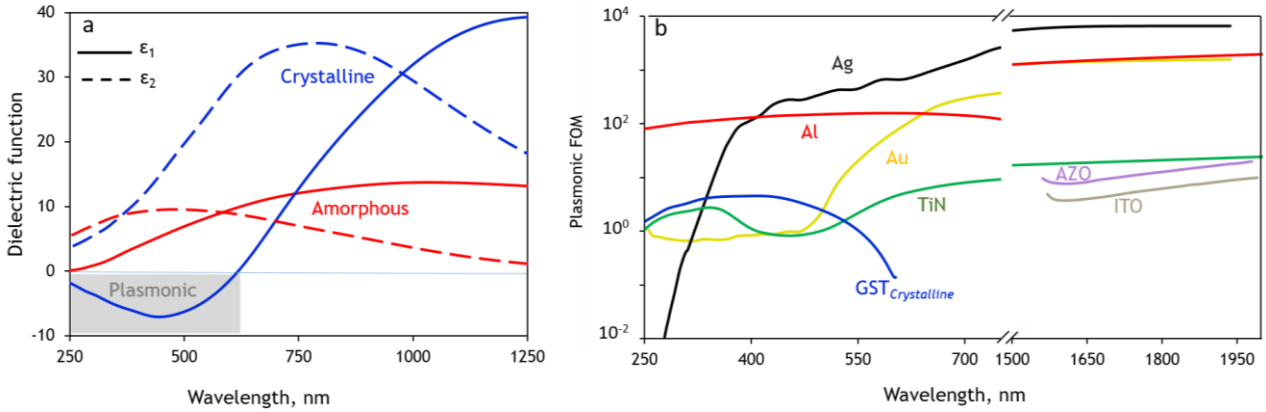

Figure 4.11. Chalcogenide plasmonics. (a) Spectral dispersion [from variable angle ellipsometric measurements] of the real ε_1 and imaginary ε_2 parts of the relative permittivity of sputtered germanium antimony telluride [GST] in its amorphous and polycrystalline phases. (b) Spectral dispersion of plasmonic figure of merit for polycrystalline GST and a selection of other plasmonic materials [as labelled; calculated using material parameters from.

its melting point T_m (600°C). The reverse transition – a melt-quenching process – can be driven by shorter, higher energy pulsed excitations that bring the material momentarily to a temperature above T_m.

This work employs nanoscale thin films of the chalcogenide phase-change medium $Ge_2Sb_2Te_5$ (GST). 500 nm thick amorphous films deposited under high vacuum are structured by focused ion beam milling with non-diffracting, sub-wavelength grating metasurface patterns having periods in the 300-400 nm range (Fig. 4.12). Unstructured, amorphous GST is a transparent absorbing dielectric at ultra-violet/visible wavelengths, with a reflectivity (of 15-30% in the present case) that is not substantially modified in this spectral range by the nano-grating structures. In stark contrast however, the crystalline phase has a negative value of ε_1 in the wavelength range from 200-615 nm and may thus support surface plasmon resonance modes that dramatically change the optical response of nanostructured surfaces.

This is illustrated by the vibrant colours produced in reflection imaging of the crystalline GST nano-gratings (Fig. 4.12b) under TM polarized light, which vary as a function of grating period. The spectral dispersion of normal-incidence reflectivity for a 300 nm period grating in amorphous (dielectric) and crystalline (plasmonic) phases is presented in Figure 4.13. For incident light polarized perpendicular to the grating lines (along the *x* direction defined in Figure 4.12b - the TM grating orientation) there is a significant change in this dispersion associated with the crystallization of the GST (Fig. 4.13a), with a pronounced reflection resonance centered at 535 nm, giving rise to the vivid green color shown in Figure 4.12b. Finite

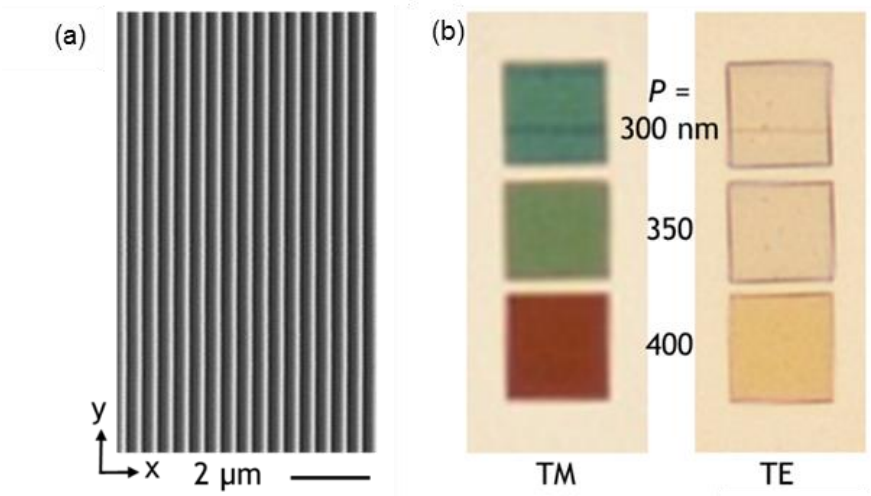

Figure 4.12. Colour tunable crystalline chalcogenide metasurfaces, (a) Spectral dispersion (from variable angle ellipsometric measurements) of the real and imaginary parts of the relative permittivity of a 500 nm thick germanium antimony telluride film in its amorphous and crystalline phases. (b). Scanning electron microscope image of a section of a GST nano-grating fabricated by focused ion beam milling. (c) Reflection optical microscopy images of crystalline phase GST nano-gratings [20 µm × 20 µm square domains surrounded by unstructured crystalline GST] of varying period [as labelled], for TM and TE polarized incident light.

element method simulations utilizing material parameters from Fig. 4.11a reproduce the experimentally observed reflection resonance at 535nm for TM-polarized light and reveal the nature of the plasmonic mode excited in the nanostructure at this wavelength (see field map inset to Fig. 4.13a). For TE-polarized light, no resonances are observed; the amorphous-

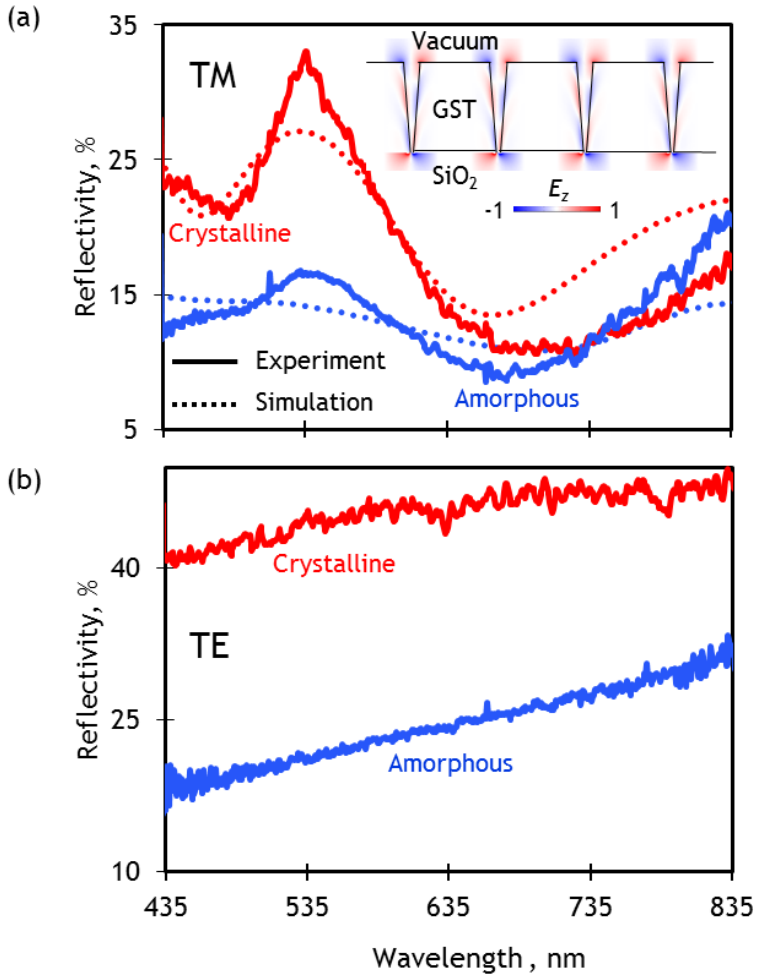

Figure 4.13. Spectral dispersion of normal incidence reflectivity for a 300 nm period grating in a 500 nm thick GST film for (a) TM- and (b) TE-polarized light and for the amorphous and crystalline phases of GST [as labelled]. Dotted lines in (a) are numerically simulated TM spectra for the nanograting structure. The inset to (a) shows the numerically simulated distribution of the *z*-component of electric field in the *xz*-plane for the crystalline phase of GST at the 535 nm resonance wavelength.

crystalline transition produces only a broadband change in the level of reflectivity (Fig. 4.13b): In this orientation the nano-grating behaves as a linear medium with a non-dispersive effective refractive index related to that of the GST and its fill fraction within the grating structure.

In order to achieve reversible optical switching in practical devices, the film needs to be thin (semi-transparent) and encapsulated between transparent protective layers to prevent degradation of the chalcogenide in air, especially at elevated phase transition temperatures. For this reason we thin out the previous sample with total thickness of 70 nm (GST) and deposited it between 70 nm protective layers of ZnS/SiO_2 on optically flat quartz substrates by RF sputtering (Kurt J. Lesker Nano 38) from $Ge_2Sb_2Te_5$ and $ZnS:SiO_2$ (1:9) alloy targets. A base pressure of 5×10^{-7} mbar was achieved prior to deposition and high-purity argon was used as the sputtering gas. The substrate was held within 10K of room temperature on a rotating platen 150 mm from the target to produce low-stress amorphous films. Nano-grating metasurface arrays were subsequently milled though the ZnS/SiO2 – GST – ZnS/SiO2 tri-layer using a focused (gallium) ion beam (FEI Helios NanoLab 600), at a beam currents ⩽28 pA to prevent crystallization of GST (via ion beam-induced heating) during the milling process. Metasurface domains, each measuring 20 × 20 μm in the sample plane, were fabricated with a range of periods P from 250nm to 400 nm, with a fixed milled linewidth W of 100 nm (Fig. 4.14).

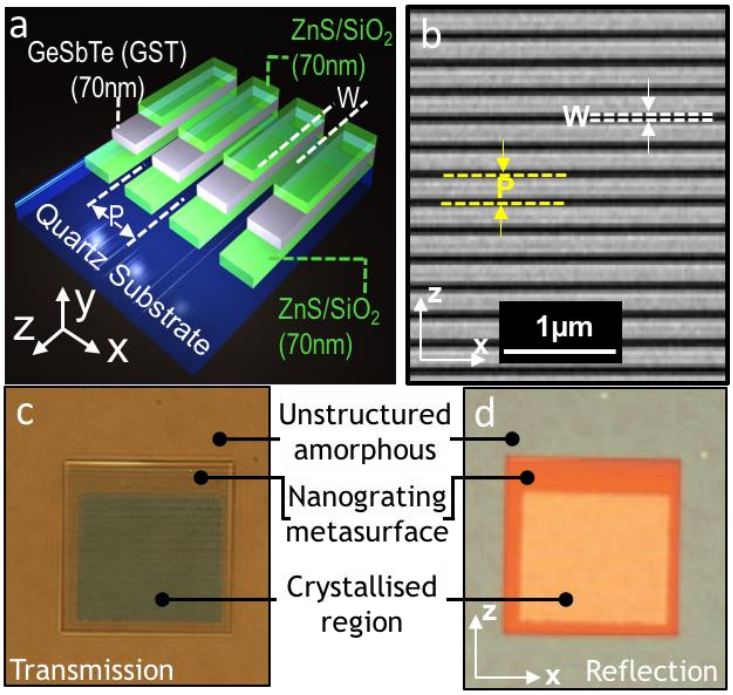

Figure 4.14 GST switchable plasmonic metasurfaces. (a) Artistic cut-away section of nano-grating metasurface structures fabricated for the present study in a 70 nm film of GST between two layers [70 nm each] of ZnS/SiO_2. (b) Scanning electron microscope image of a section of a ZnS/SiO_2–GST–ZnS/SiO_2 tri-layer metasurface [dark areas being the quartz substrate exposed by focused ion beam milling, i.e. removal of the tri-layer]. (c) Transmission and (d) reflection TM-polarized, normal incidence reflection images of a 20 × 20 μm, *P* = 400 nm, amorphous phase GST tri-layer metasurface domain [surrounded by unstructured amorphous phase GST tri-layer], part of which – the central 12 × 12 μm region appearing green in transmission, pale orange in reflection – has been selectively crystallized by fs-pulsed laser illumination.

The amorphous-to-crystalline transition in chalcogenides is an annealing process that may be initiated globally by ambient, or locally by laser- or electrical current-induced heating to a temperature above the material's glass-transition point Tg (~160°C for GST) but below its melting point Tm (~600°C). [141] The reverse transition – a melt-quenching process – can be driven by shorter, higher energy pulsed excitations that bring the material momentarily to a temperature above Tm [153]. In this work, structural transitions in the GST layer are excited using 85 fs laser pulses at a wavelength of 730 nm in a beam focused to a diffraction-limited spot and raster-scanned over the sample using a spatial light modulator, as described in Ref [131]. By varying the number, repetition rate and energy of pulses delivered at a given point, one may accurately control the temporal profile of optically-induced temperature change in the GST. Here, we employed trains of 50 ~140 $mJcm^{-2}$ pulses at a repletion rate of 1 MHz for crystallization.

The normal-incidence transmission and reflection characteristics of the GST nano-grating metasurfaces, in amorphous and crystalline states, were quantified, for incident polarizations perpendicular and parallel to the grating lines (along the x and z directions defined in Fig. 4.14 or TM and TE orientations of the grating, respectively), using a microspectrophotometer (CRAIC QDI2010). A sampling domain size of 15 μm x 15 μm and numerical aperture of 0.28 with GST in its amorphous phase measured first. The transmission of the unstructured ZnS/SiO_2–GST–ZnS/SiO_2 tri-layer increases monotonically with wavelength across the UV to near-IR spectral range, from 5% to 35% (Fig. 4.15a). For the polycrystalline phase, levels of transmission are suppressed across the entire range but follow essentially the same trend, reaching approximately 12% at 900 nm (Fig. 4.15b). The sub-wavelength period (and therefore non-diffractive) nano-grating metasurface structures introduce resonances for TM-polarized light (incident electric field perpendicular to the grating lines), at visible wavelengths

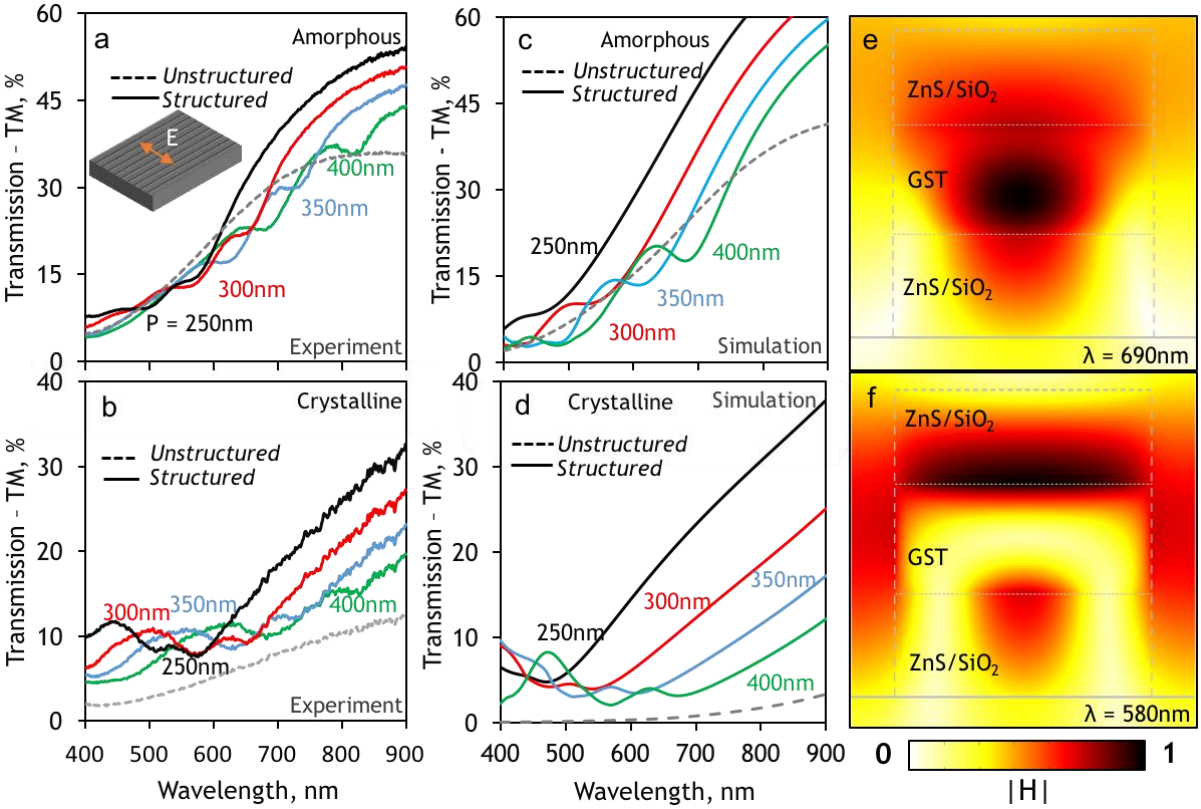

Figure 4.15 Optical properties of amorphous [dielectric] and polycrystalline [plasmonic] GST metasurfaces. (a, b) Measured spectral dispersion of ZnS/SiO_2–GST–ZnS/SiO_2 nano-grating metasurface TM transmission for a selection of grating periods *P* [as labelled], for the amorphous (a) and polycrystalline (b) states of the GST layer, overlaid with spectra for the unstructured tri-layer [dashed lines]. Corresponding numerically simulated transmission spectra (c, d). Distributions of the normalized magnetic field, H in the *xz*-plane for a unit cell of a *P* = 400 nm nano-grating (e, f) for transmission resonance wavelength at λ = 580nm for amorphous and 690nm for the respective crystalline phase.

dependent on period P, for both phase states of GST, which manifest themselves in the transmitted and reflected colors of the metamaterial domains (Figures 4.15c-d). For TE-polarized light, the observed optical response in either amorphous or polycrystalline GST is largely invariant with nano-grating period and almost identical to the unstructured tri-layer transmission spectrum for the corresponding phase state. (Corresponding reflection spectra, and TE polarized spectra are presented in Fig. 4.16.)

It should be noted that the observed TM resonances are of markedly different nature for the two phase states of GST – in the amorphous case they are displacement current resonances reliant upon the high refractive index contrast between the dielectric GST and surrounding media, while for the crystalline phase the resonances are plasmonic, i.e. based upon the opposing signs of ε1 at interfaces between the GST and surrounding media. Numerical simulations clearly illustrate this difference: Figures 4.15c-f show results of a 3D finite-element Maxwell solver model, which employs ellipsometrically measured values for the complex permittivity of GST as presented in Fig. 4.11a. It assumes lossless non-dispersive refractive indices of 1.46 and 1.80 for the semi-infinite quartz substrate and the ZnS/SiO_2 layers

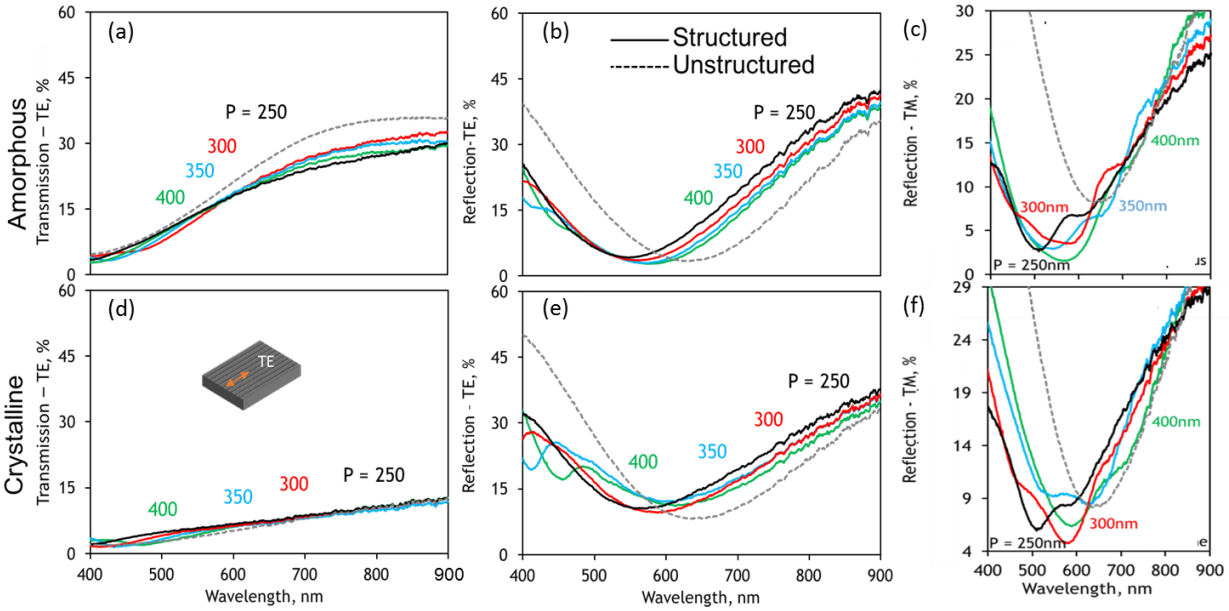

Figure 4.16 Transmission/Reflection spectra of GST metasurfaces. Amorphous (a-c) and Crystalline (d-f) nano-gratings spectra for period P=250nm up to 400nm as annotated. Non-resonant TE-mode exist in both amorphous and crystalline states. Dielectric resonances become stronger close to near-infrared as the extinction ratio of Chalcogenide glasses decreases, see Chapter 4.1. Reflection spectra hold resonances in both Amorphous (c) and crystalline state (f) as it can be seen in Fig. 4.15 are related with mie and plasmonic resonances, respectively.

respectively; normally-incident narrowband plane wave illumination; and, by virtue of periodic boundary conditions, a nano-grating pattern of infinite extent in the x-y plane. There is good qualitative and quantitative agreement between experimentally measured (Figs. 4.15a, b) and numerically simulated (Figs. 4.15 c, d) transmission spectra for the GST metasurfaces in both amorphous and crystalline states. Discrepancies are attributed to manufacturing imperfections (the computational model assumes ideal rectilinear nano-grating geometry as illustrated schematically in Fig. 4.14a) and contamination of the ZnS/SiO_2 and GST layers (gallium ion implantation) during FIB milling, which has the effect of modifying refractive index. The cross-sectional distributions of magnetic field in Figs. 4.15e and f, reveal essential differences between the resonant modes for amorphous and crystalline phase GST. In the former case the field is stronger within the (higher index dielectric) GST layer than in the ZnS/SiO_2 layers above and below, while in the latter the field is 'expelled' from the body of the metallic GST layer and is stronger at the interfaces with ZnS/SiO_2.

Non-volatile, light-induced structural transitions between amorphous and crystalline phases of GST, i.e. its conversion between dielectric and plasmonic states, thereby changes the transmission and reflection characteristics of the metamaterial, manifested in the visible spectral range as changes in color. We define the transmission and reflection switching contrast

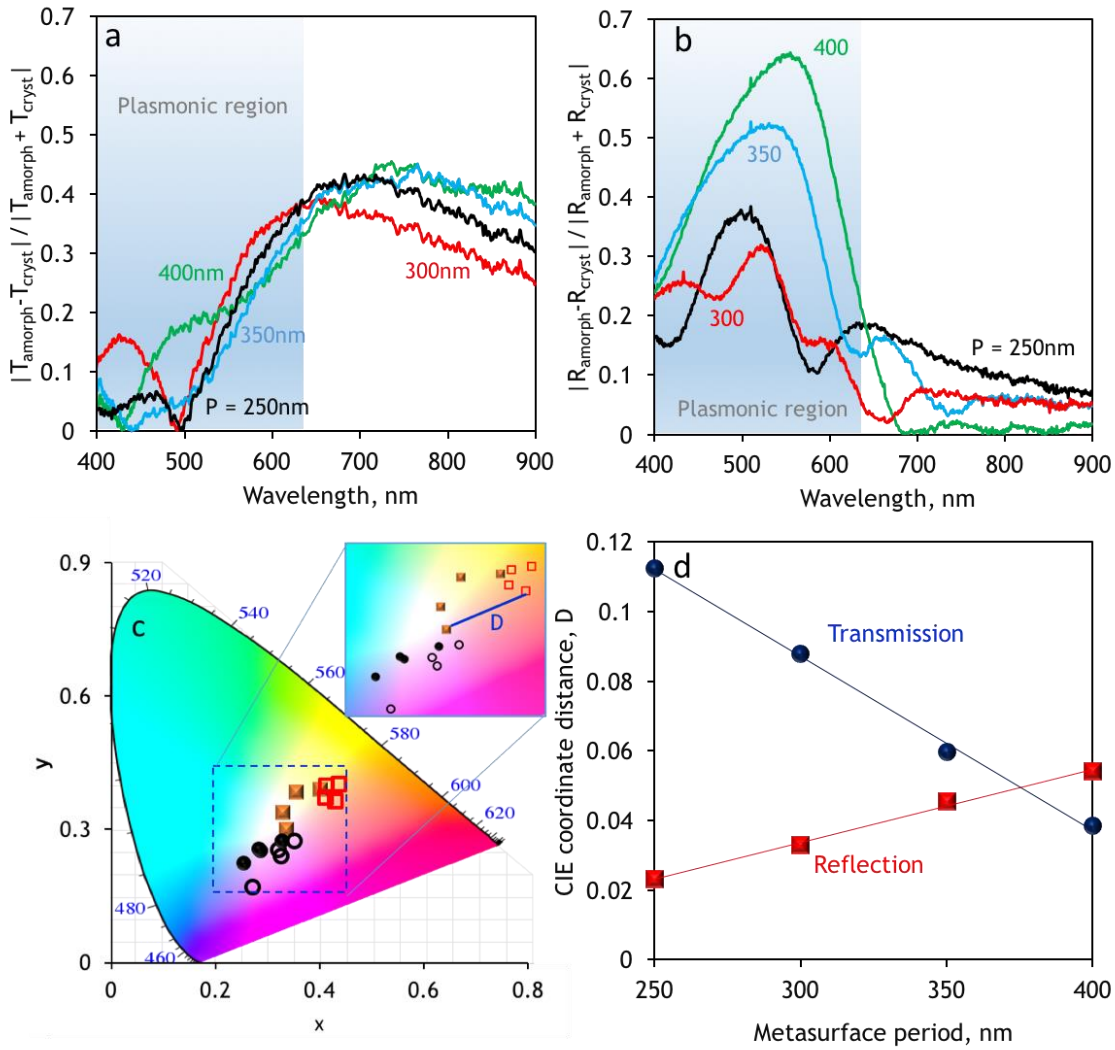

Figure 4.17 Switching contrast and color change. Relative (a) transmission and (b) reflection change induced by (upon) structural change between amorphous and crystalline phases of the GST metasurfaces with different periods (as labeled). (c) Corresponding reflection (circles) and transmission (squares) CIE colour palette with marked points indicating the metasurfaces [P = 250 – 400 nm] shown for both amorphous (unfilled) and crystalline (filled) phases. (d) Colour change resulting from phase transition quantified as the euclidean distance [D] in CIE colour plot between corresponding amorphous and crystalline points, given as a function of metamaterial period.

as a ratio of the difference between levels for the amorphous and crystalline phases of the GST layer to the sum of said levels (Figs. 4.17a, b). In the present case, greatest contrast is achieved in reflection, at grating period-dependent wavelengths in the spectral band where GST is converted between dielectric and plasmonic forms. The associated changes in color can be quantified through observing the CIE 1931 color space. Perceived color coordinates for GST tri-layer metasurfaces in their amorphous and crystalline phases, derived directly from reflection and transmission spectra. It is used Judd-Vos-modified CIE 2-deg color matching functions [154], assuming in all cases an illuminating light source with the spectral radiant power distribution of a 6500 K black body and a normalized observational brightness level. Every sample is plotted in a two-dimensional representation of the CIE1931 space in Fig. 4.17c.

The change in color given by the structural transition in GST can be quantified as the Euclidean distance between corresponding points in CIE space (Fig. 4.17d).

In summary, we show that the chalcogenide phase-change medium, germanium antimony telluride (GST), can be switched in a non-volatile fashion between amorphous and crystalline phases of respectively dielectric (positive real part of relative permittivity ε) and metallic (negative real part of ε) character in the UV-visible spectral range. This behavior enables switching between plasmonic and all-dielectric resonances in nanostructured GST, in a sub-wavelength optically switchable device geometry. Phase change chalcogenides have been touted as a potential candidate for future solid-state displays. To obtain the colour gamut required for these applications, research has focused on complex multilayer deposition or nanofabrication procedures or hybridisation with metallic back reflectors [60], [155], [156]. In the metal-free phase change metasurfaces demonstrated here, the magnitude of the colour change is not a direct function of switching contrast, as a change in colour involves an overall redistribution of the spectral response. However, plasmonic-to-dielectric transitions in such metasurfaces allow engineering controlled spectral redistributions that rely on the linear dependence of metasurface period to magnitude of colour change in both reflection and transmission. The parameter space for metasurface design is large and different structural designs can extend the accessible color range beyond those demonstrated here, and may include color that is dependent or not on polarization (depending on design symmetry). Consequently, such color tunable metasurfaces offer a robust CMOS-compatible material platform for active and reconfigurable metadevices such as thin solid state displays, data storage, switchable/tunable filters, beam shapers and optical limiting components.

Chapter 5

Ultrafast Coherent Control of Dielectric Metamaterials

Recently, 'coherent control' of absorption has emerged as a new mechanism for controlling light-with-light, [157] with potential applications ranging from signal processing in coherent information networks [158]–[162] to excitation-selective spectroscopy. [163] It allows for the implementation of various all-optical analogue logical functions in four-port devices (with two inputs and two outputs) [158] and can function at very low intensities, down to the single photon level [106] and in the quantum regime. [164] In the simplest case, such devices may comprise a thin (sub-wavelength thickness) layer of absorbing material illuminated from both sides by two mutually coherent light waves, which represent the two input signals, while the two reflected/transmitted waves constitute the output channels. The coherent redistribution of energy among the four channels and coherently-controlled level of dissipation in the absorber

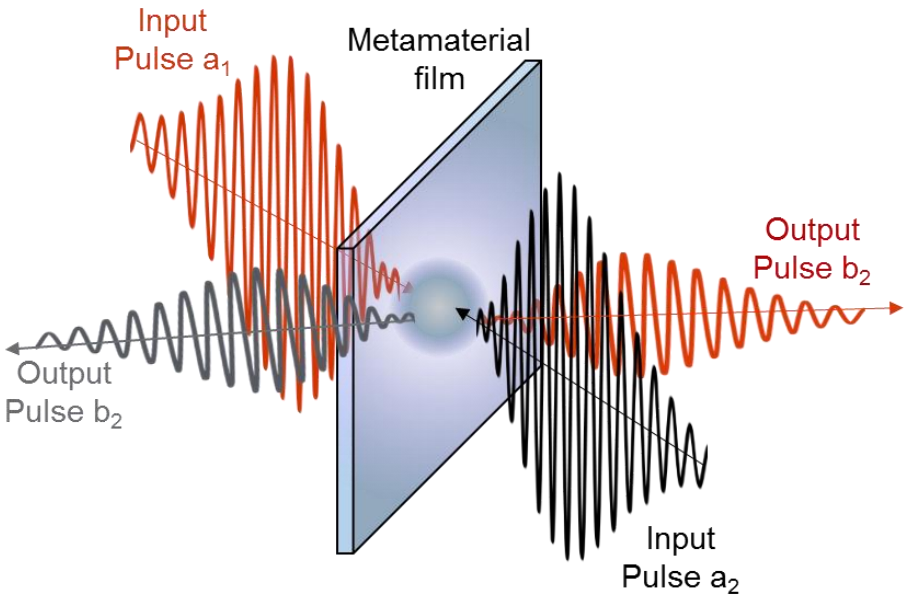

Figure 5.1 Ultrafast Coherent Control in a thin film metamaterial. Schematic image presenting the concept of Coherent ''control of light by light without nonlinearity''. Two counter-propagating optical pulses of the same central wavelength can form a standing wave. This standing wave with finite dimensions forms nodes and anti-nodes, where a metamaterial film interacts either weakly, or strongly, respectively. Output light pulses can be modulated either by the position of the metamaterial film or from the phase difference of the input pulses.

underpin the functionality of such devices. The speed of response of coherent signal processing devices is limited only by width of the absorption line, so for optimal switching speed and contrast the thin film should ideally absorb 50% of traveling wave power across the entire spectrum of the signals involved, upon which basis it may coherently absorb anywhere between 0 and 100% of incident light (depending on the relative phase and intensity of the two inputs at the absorber plane).

Assuming a linear, time-independent and passive system, the output fields, b_1 and b_2 are fully determined by the input fields a_1, a_2 and the S matrix, which can describe any optical system*:*

$$\begin{pmatrix} b_1 \\ b_2 \end{pmatrix} = \begin{pmatrix} s_{11} & s_{12} \\ s_{21} & s_{22} \end{pmatrix} \begin{pmatrix} a_1 \\ a_2 \end{pmatrix} \tag{1}$$

in order to identify the conditions (input relative intensities and phase shifts) under which coherent perfect absorption, CPA occurs, we need to solve this 2x2 system, for $b_1=b_2=0$, corresponding to zero output fields. For an ideal lossless system, CPA is not possible. [165] For this reason we define output powers $P_{out1,2}=\left|b_{1,2}\right|^2$ and identify the parameters which can control (modulate) the output intensity. Here, we need to specify some general properties of matrix **S**, in the current study we consider reciprocal medium, transmission is same for each side illumination, as a result $s_{11}=s_{22}$, while we keep the general condition of assymetric structures were reflective waves can be different from each other, $s_{21} \neq s_{12}$. So the matrix **S** can be written as:

$$\mathbf{S}=\begin{pmatrix} \tau & \rho_1 \\ \rho_2 & \tau \end{pmatrix} \tag{2}$$

The element of the scattering matrix are the following: $\rho_1 = |\rho_1|e^{i\varphi_{\rho 1}}$ and $\tau = |\tau|e^{i\varphi_\tau}$ are the reflection and transmission coefficients, respectively, of the incident field E_1, while $\rho_2 = |\rho_2|e^{i\varphi_{\rho 2}}$ and $\tau = |\tau|e^{i\varphi_\tau}$ of the incident field E_2, respectively. The reflection phases are $\varphi_{\rho 1}$ and $\varphi_{\rho 2}$, and the transmission phases are φ_τ. CPA occurs when det**S**=0, as a result $\tau^2 = \rho_1\rho_2$ and the relative phase $\left|\varphi_{\rho 1} - \varphi_\tau\right| = (2m+1)\pi$. [160], [166]–[168] In other words, the CPA results of an extremely delicate balance where the interfering waves have the same modulus

and differ by a phase of π. Next, we will benefit from this mechanism to provide a coherent all-optical modulator of ultrafast pulses.

5.1 Ultrafast coherent absorption in Diamond metamaterials

We present the first experimental demonstration of coherent light-by-light modulation at few-optical-cycle (6 fs) pulse durations, enabled by a nanostructured polycrystalline diamond broadband metamaterial absorber only 170 nm thick. Coherent optical gating on thin, resonant plasmonic metamaterial absorbers with continuous wave [168] and 130 fs pulsed [163] beams has previously been demonstrated. However, to exploit the coherent dissipative process for controlling even shorter pulses a material providing strong, spectrally flat absorption over a very broad wavelength range, while being capable of withstanding high peak optical intensities, is required. Moreover, for efficient all-optical gating the absorbing film shall be of subwavelength thickness and a balance among transmission, absorption and reflection with ideal proportions of 1:2:1. Here we report that a nanostructured, free-standing diamond membrane exhibits the characteristics necessary for high contrast coherent control of ultrashort (6 fs) optical pulses comprising only a few oscillations of electromagnetic field. . By positioning the subwavelength thickness nanostructured membrane between nodes and anti-nodes formed in the experimental setup described in Figure 5.4, we can modulate coherent absorption that experiences the metamaterial. This is a common technique presented in several works. [106], [158], [163], [168], [169]

Diamond, in the form of single-crystal plates, individual micro/nano-crystals and polycrystalline films, has attracted increasing attention as a photonic material over the past decade, [170], [171] for optical waveguide and photonic crystal structures, for its nitrogen-vacancy color centers (which can be harnessed for quantum, sensing and labelling applications), and recently as a platform for mid-infrared ‘all-dielectric’ metamaterials. Here, we introduce a nanostructured diamond optical range metamaterial fabricated from a free-standing polycrystalline membrane. We show that focused gallium ion beam milling of the membrane, with a sub-wavelength nano-hole pattern, delivers an elevated level absorption over a VIS-NIR band broad enough to facilitate coherent modulation of few-femtosecond optical pulses. For the present study, a metamaterial comprising 280 nm diameter nano-holes in a square array of 500 nm period, covering a total area of approximately 100 μm × 100 μm, was fabricated by focused ion beam (FIB) milling in a 170 nm thick polycrystalline diamond membranes (on silicon frames, with a clear aperture of 300 μm diameter) by Applied Diamond

Inc. (Figure 5.2a). The ion beam was raster scanned with a step of 500nm, dwell time of 600msec, the ion density used was $15x10^{17}$ Ga^{+}/cm^{2}, the acceleration voltage was 30 keV, with the FIB milling rate being 0.021 μm^{3}/nC. Tapered hole profiles (off-vertical side walls) are an inevitable consequence of the FIB milling process, and the effect is exaggerated here by the necessity of employing a relatively high ion beam current [15] (0.66 nA), giving an angle of ~20o. There is also, inevitably, some implantation of gallium from the ion source, which is known to cause stoichiometric changes in a diamond lattice, thereby modifying the mass density, strain and optical properties of ion-implanted films. [172], [173] The structural dimensions employed in numerically modelling the optical properties of the diamond metamaterial are presented in the cross-sectional schematic of Figure 5.2b. Polycrystalline diamond has a refractive index (evaluated by variable angle spectroscopic ellipsometry) of 2.4 across the 600-950 nm spectral range of interest, while gallium-doped diamond in an assumed 50 nm wide ring around each nano-hole is taken to have a refractive index 3.45 + 0.6i and is responsible for the nanostructured membrane's increased VIS-NIR absorption. With a unit cell size of 500 nm the metasurface is non-diffracting throughout the experimental wavelength range; It has four-fold rotational symmetry and so its properties do not depend on the polarization state of incident light; But they are directionally asymmetric in consequence of the tapered hole profile, as illustrated by the spectra in Figure 5.2c and 5.2d. Figure 5.2e and f present the distributions of normalized out-of-plane electric field and in-plane displacement currents for the two directions of illumination ('front' and 'back' as denoted in Figure 5.2b) at 780 nm - the central wavelength of the fs-pulsed laser source employed in experiments.

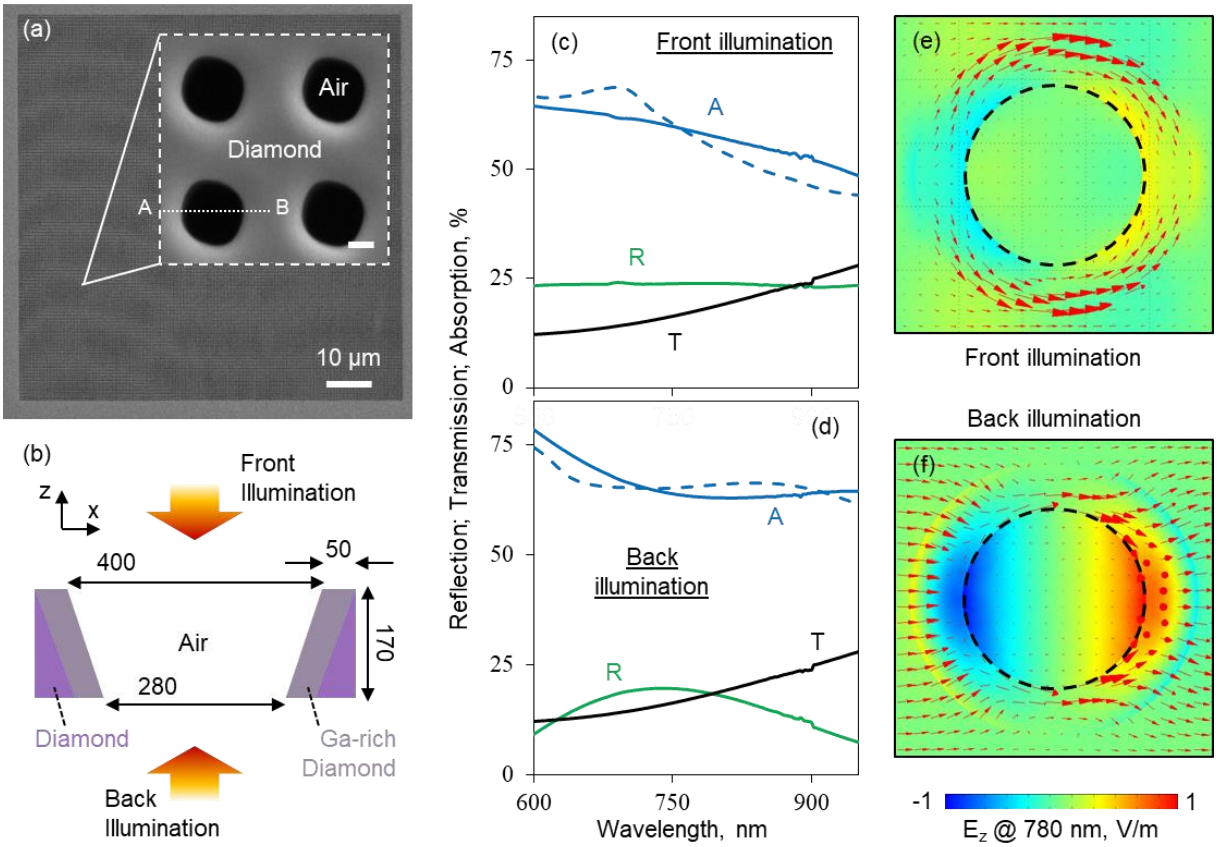

Figure 5.2 Diamond membrane metamaterial. (a) Scanning electron microscope image of nano-hole array metamaterial, viewed from the front/back side as defined in panel (b). The inset shows four unit cells of the array at higher magnification [100 nm scale bar]. (b) Schematic cross-section of a metamaterial unit cell [period 500 nm], nominally along line AB in panel (a), with dimensions annotated in nanometers. (c, d) Solid lines - spectral dispersion of normal incidence reflection, transmission and absorption [=1−{R + T}] for the diamond metamaterial measured using a microspectrophotometer for (c) front and (d) back illumination as defined in panel (b); Dashed lines – numerically simulated absorption spectra. (e, f) Numerically simulated field maps showing the distribution of the *x*-component of electric field in the *xy* plane at the midpoint of the membrane in the *z* direction, at a wavelength of 780 nm. Overlaid arrows indicate the direction and magnitude of electric displacement.

At this wavelength, transmission T is 18% (in both propagation directions, as must be the case in a linear reciprocal medium), reflection R is 18% for front illumination versus 24% from the back, and absorption levels (evaluated as 1-{T+R}) correspondingly differ by 6% for the two directions. Back illumination excites an electric dipole parallel to the incident polarization direction in the plane of the membrane, leading to a characteristic broad reflection resonance, with a peak in this case at a wavelength of 740nm (Figure 5.2d). In contrast, no resonant features are apparent for front illumination and the reflection spectrum is almost flat (Figure 5.2c). For both directions of propagation the proportionality among transmission, reflection and absorption is less than ideal, but it is of greater importance in the present case that the diamond metasurface maintains an elevated and weakly-dispersive level of absorption over a

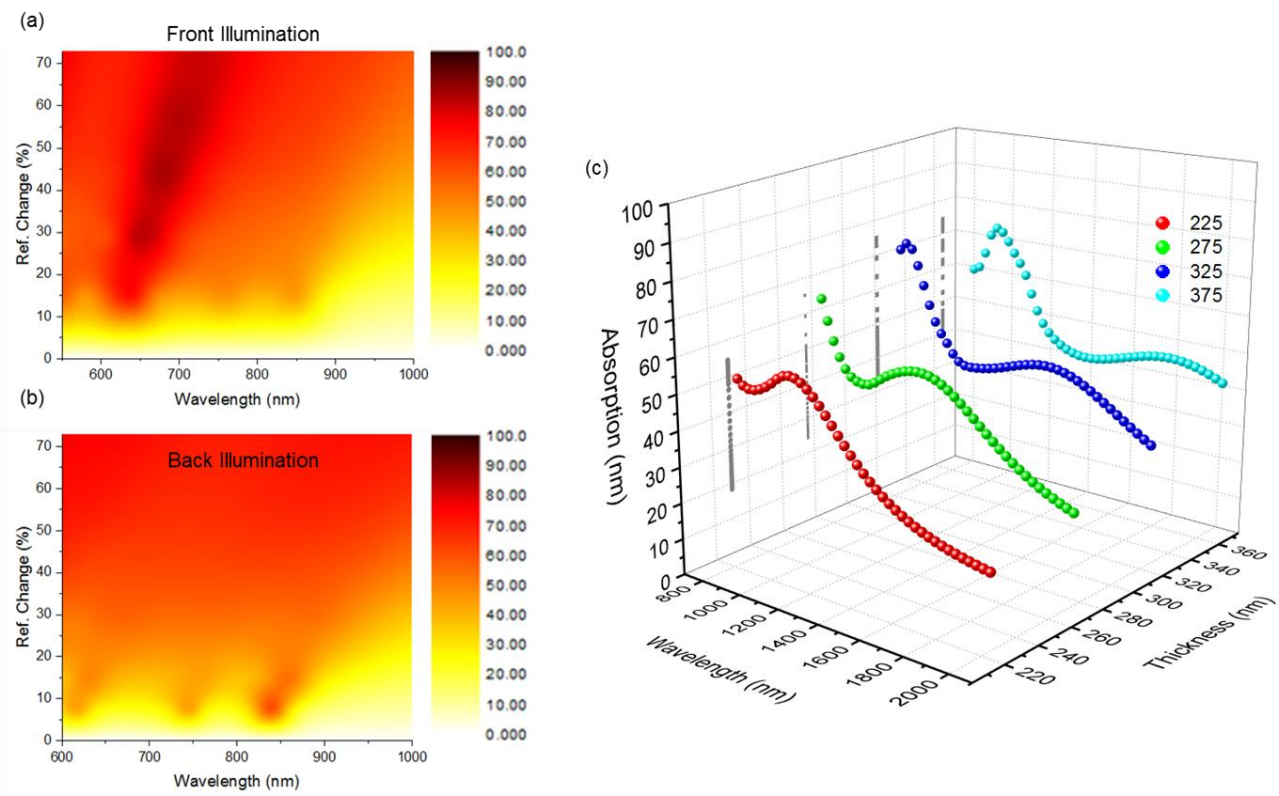

Figure 5.3 Broadband Absorption of Diamond metamaterials. Dependence of absorption on diamond metamaterial to relative refractive index change and wavelength λ based on numerical modelling of the front (a) and back (b) illumination. Relative index change is directly related with Ga implanted depth and concentration. (c) Dependence of metametarial absorption across several thicknesses, as annotated, can extend absorption window further in NIR spectrum.

spectral range greater than the ~100 nm bandwidth of ultra-short (few-fs) laser pulses (and greater than the typical linewidth of plasmonic metasurface resonances. [3,8,9,11,12]).

We have also explicitly verified numerically (commercial software, COMSOL) that for wavelengths with around 50% loss and equal reflection and transmission, R_i=T, i=1,2, the diamond metamaterial induces an absolute phase shift on the reflected and transmitted beams of 0 and π, respectively, while unstructured diamond causes 0 and π/2, respectively. As described in the previous section this makes these diamond metamaterials ideal to perform coherent absorption, over the corresponding wavelengths.

We furthermore assess the change occurred in diamond refractive index after ion implantation and extend the applicability of this metamaterial in the NIR regime as well. The refractive index of diamond can be changed from the ion concetration of implantated Ga^+, as stated in [173] thus provide a parameter to control refractive index change across the NIR and visible spectrum. The depth that ions penetrated the diamond sample and the concetration of ions can be controlled experimentally by the acceleration voltage and the ion current used during fib

milling, respectively. The gallium content around the holes can be estimated based on SRIM calculations (a program for calculating the stopping ranges of atoms in matter). [174] We calculate that ions of Ga^+ at normal incidence and acceleration voltage of 30keV on diamond substrate create an implanted layer extended from 10nm-50nm thickness with a peak of ion concetration at 25nm and ion concetration of the order of 10^{22} for ion current of 0.66pA. The correlation between the refractive index change occurs in our sample is an estimation based on the agreement between the absorption measured experimentally and the absorption calculated with COMSOL for several changes of the refractive index. Previous works [10], [11] estimate the change of refractive index by 20% for the real part of refractive index and the extinction coefficient raise up to 0.2. In these studies, they do not perform physical sputtering of the target (Diamond), instead only ion implantation takes place. In our case, we provide simulated data of absorption in the colour maps of Figure 5.3 a and b, for front and back illumination of the proposed metamaterial. Best fitting between the experimental absorption spectra and those provided in Colour maps, 5.3 (a) and (b) correspond to a refractive index change by 40%: refractive index of n=3.45 and extinction ratio of k=0.6. This refractive index change is almost double than previous works, [87], [173] as expected due to the much higher ion current applied in these samples. However, for the sake of clarity, we present also the absorption spectra result of 0 to 70% refractive index change an effect which can be adjusted by the acceleration voltage of ions. Furthermore, we suggest that extention of the flat absorption is feasible after the increase of thickness of the sample. 4 cases are studied for thicknes of 225,275,325 and 375nm as presented in Figure 5.3c. The sample with thickness of 325nm operate as an ideal coherent absorber with 50 absorption and 25% Transmission and reflection across the telecommunication wavelength of 1550nm.

The experimental short-pulse coherent modulator configuration is illustrated schematically in Figure 5.4. The ultrafast measurements have been performed by Dr. Venkatram Nalla at the Nanyang Technological University, in Singapore. A train of femtosecond laser pulses (with a durations adjustable down to ~6 fs and a center wavelength tunable from 650 to 975 nm, is divided by a pellicle into two (collinearly polarized) 'input' beams focused at normal incidence from opposite sides onto the diamond metamaterial by a pair of focusing mirrors. The metamaterial is mounted on a piezoelectric translation to facilitate the setting/tuning of the relative time delay, and thus the relative phase difference, between corresponding pulses from the two input channels. The two output beams (transmitted and reflected from both sides of the metamaterial) are directed via pellicle beam splitters to a pair of identical photodiodes. In

keeping with the behavior reported in Ref. [12] for a plasmonic metasurface illuminated probed using much longer 130 fs pulses, the output signal here is seen to oscillate between coherently-suppressed and -enhanced levels as a function of the time/phase delay between the incident 6 fs pulses in the diamond metamaterial plane, within an envelope defined by their temporal overlap (Figure 5.5a). The signal is high (coherent absorption low) when the metamaterial is located at the nodes of the electric field standing wave formed by the input beams, and vice-versa at the anti-nodes. The zero-delay position is taken to be the point at which magnitude of coherent absorption is maximized (i.e. output signal minimized); the oscillation period corresponds to a distance of half of the center wavelength of the incident pulses. At large positive and negative delays, when there is no overlap between incident pulses in channels 1 and 2, the output signal is constant at a level corresponding to the total incoherent absorption of the two input beams by the metamaterial. The discrepancy in the amplitude of coherent modulation between the two output channels is a consequence of the directional asymmetry of the metamaterial discussed above.

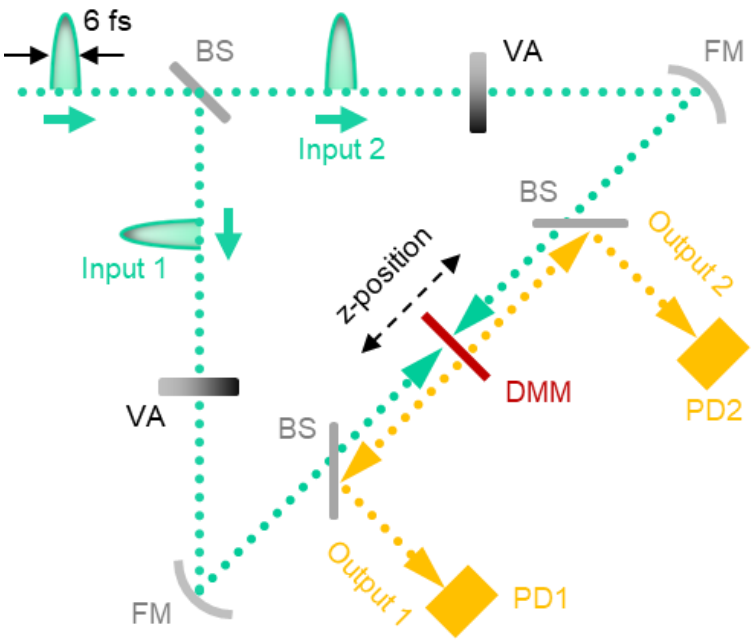

Figure 5.4 Experimental arrangement for measurement of short-pulse coherent absorption modulation in a diamond membrane metamaterial. The input beam is provided by a 6 fs Ti:sapphire oscillator via a pulse shaping system, which is employed to tune the duration and center wavelength of pulses. (BS = pellicle beam-splitter; VA = variable attenuator; FM = focusing mirror; DMM = diamond metamaterial; PD = photodiode).

We define the coherent modulation depth as: $\frac{P_{max}-P_{min}}{P_{max}+P_{min}}$, where P_{max} and P_{min} are respectively the highest and lowest output signal levels (averaged over the two output channels) achieved around the zero-delay point (as annotated in Figure 5.5a). A modulation depth of between 0.34

and 0.41 is maintained by the diamond metasurface for pulse durations ranging all the way from 185 fs down to 6 fs (Figure 5.5b), in contrast to the unstructured diamond membrane which is to all intents and purposes is non-absorbing. There is zero phase difference between the two output channels across the entire range of pulse durations. This behavior is markedly different from that observed with plasmonic metamaterial coherent absorbers, where the output channels shift increasingly out of phase as the pulse duration falls below ten femtoseconds, [175] thereby limiting the modulation bandwidth.

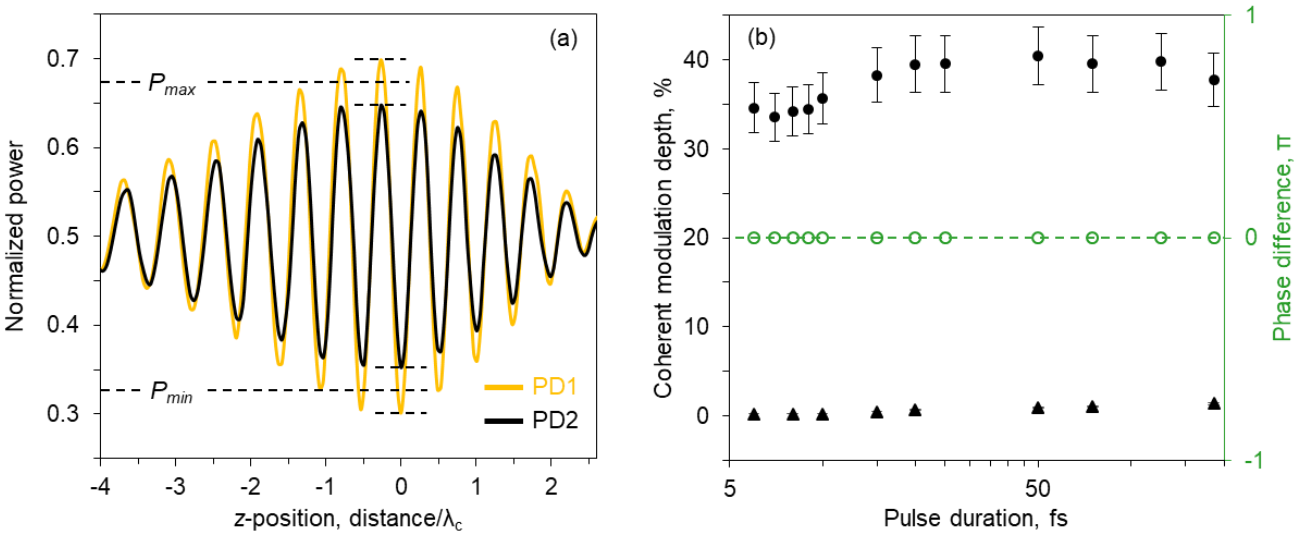

Figure 5.5 Ultrashort pulse modulation using a diamond metamaterial. (a) Dependence of output power in channels 1 and 2 [yellow and black lines respectively, relative to input power per channel] on the z-position [as defined in Figure 2] of the metamaterial, i.e. on the temporal delay between counter-propagating incident 6 fs pulses at a center wavelength λ_c = 780 nm. (b) Coherent modulation depth as a function of pulse duration for the diamond metamaterial [filled circles] and for the unstructured diamond membrane [triangles], and for the former the phase difference between output channels 1 and 2 [open circles].

Moreover, the coherent modulation depth achieved with the diamond metamaterial remains approximately constant, with again zero phase difference between the two output channels, while the short-pulse center wavelength is tuned all the way from 650 to 975 nm (the entire tuning range of the laser source), as shown in Figure 5.6 for pulse durations of 50 fs (19 nm bandwidth) and 6 fs (157 nm bandwidth). The only perturbation over this spectral range is a small dip in the magnitude of coherent absorption modulation at around 700 nm, corresponding to a dip in the single-beam absorption spectrum overlaid in Figure 5.6. Once more, this performance stands in marked contrast to that of plasmonic metasurfaces, for which the amplitude of coherent absorption modulation is strongly dispersive by virtue of their relatively narrow absorption resonances.[3,8,9,11,12]

We further study the power-dependent of this novel metamaterial, and data are presented in Figure 5.7 for coherent illumination (a) and single beam illumination (b). For low input power

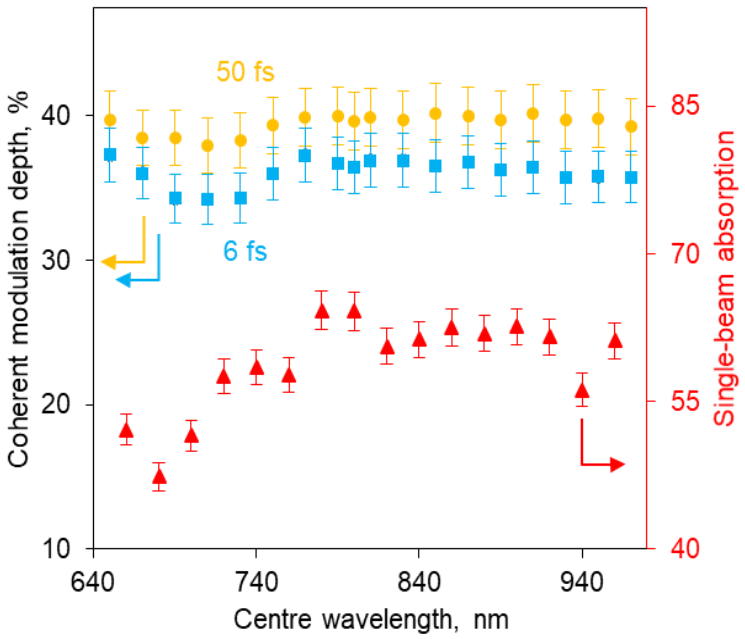

Figure 5.6 Ultrashort pulse modulation using a diamond metamaterial – spectral dispersion. Dependence of coherent modulation depth on center wavelength for pulse durations of 6 fs [square symbols] and 50 fs, at a fixed fluence of 0.4 nJ/cm^2, overlaid with the single-beam absorption spectrum for 50 fs pulses illuminated from front, evaluated as $1-\{R+T\}$ when blocking one of the two pulsed input beams [whereby one of the output channels records reflection and the other transmission].

the diamond metamaterial operate as expected, while for fluxes higher than a few nJ/cm^2 nonlinear response occurs. This is explained based on the theory of doped semiconductors. In our case Ga ions are implanted around the diamond nano-holes. As a result, coherent plasmon-phonon effects occurs which have been also observed n-doped GaAs crystals when they are pumped close to the their optical bandgap. So as long as we remain in low power illumination this effect remains non-dominant and the photo-excited carrier density remains lower than doping levels.[176], [177]

In conclusion, we have experimentally demonstrated a free-standing diamond membrane metamaterial as a broadband, polarization-independent absorber for the visible to near-infrared wavelength range, serving as the functional element of a coherent optical modulator providing modulation contrast up to 4 dB with a bandwidth of 160 THz. The underlying control mechanism is a strictly linear interference effect and as such may be implemented at arbitrarily low intensities, and does not induce harmonic distortion of signals. Ultrafast coherent modulation functionality is demonstrated here over the 650–975 nm wavelength range of the experimental short-pulse laser platform, but the device concept can be implemented across a broader VIS-NIR range with appropriate variation of the metamaterial design and/or dimensions. Modulation contrast may be enhanced with design optimization to achieve identical levels of absorption nearer 50% for both directions of light propagation through the

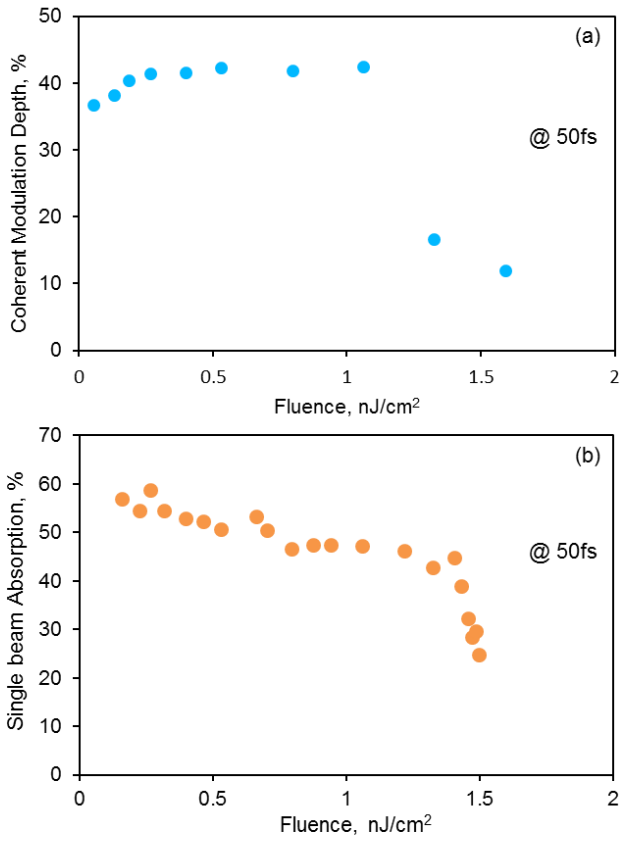

Figure 5.7 Power dependent coherent modulation of Diamond metamaterials. (a) Coherent modulation depth with variable fluence of the input pulse with duration of 50fs.(b) Absorption of diamond metamaterial under single beam illumination for the shape pulse.

metamaterial, though 4 dB may be adequate for some optical interconnect applications. [58] The upper limit on coherent modulation bandwidth for the diamond metasurface is considerably higher than the ~100 THz level observed for plasmonic metasurfaces, and indeed lies beyond the measurable range in the present study (where the shortest available pulse duration is ~6 fs). Diamond membrane metamaterials may also present advantages (over plasmonic counterparts) in terms of physical/chemical robustness and optical power handling, thereby enabling a variety of otherwise impractical ultra-short pulse, high-intensity

Chapter 6

Conclusions & Outlook

Nanostructured Photonic Metamaterials have been in the frontier of nanotechnology research for the last few years. The conclusion out of this Thesis is that there is still many exciting opportunities for technological improvement from the application point of view. All-optical modulators, electro-optical modulators, optical switches, colour-tunable displays, ultrafast switches are examples within this Thesis of the revolution that Nanostructured media, with subwavelength thickness can achieve. Particularly, throughout this Thesis, semiconductors (optically dielectric media) have been used, which provide an alternative to plasmonic counterparts, disassociated from joule heating and compatible with CMOs fabrication methods can be adopted from the photonic industry for the next generation photonic devices.

Optomechanical dielectric metamaterials have been presented for first time to operate at the sub-GHz scale, based on the actuation of opto-mechanical individual nano-resonators. Through their common optical response nano-resonators with different oscillation frequencies is shown that they can get synchronized, driven by a common light source. New opportunities are open now as these type of metamaterials can eventually result in randomly addressable individual resonators provide optical properties on demand and provide nano-devices with dynamic focusing or even memory functionalities. Further optimization of the fabrication techniques should lead to improvement of the performance of resonators, e.g. larger modulation depth, or higher mechanical q-factors can result in longer decoherence times. Furthermore, is an open question how thin can dielectric nanomembrane metamaterials eventually become and what is going to be their performance then?

Electro-optical reconfigurable metamaterials, has been demonstrated as a valuable platform to provide electrical control over the optical properties of a dielectric metamaterial. Based on structural reconfiguration this method can appear as an alternative platform from carrier injection or electro-optic Pockels effect, to control electrically optical responses at the nanoscale. Even more complicate applications than intensity modulation can be possible with modulation frequencies of a few MHz. Further optimization of the design of these devices could result in higher mechanical eigenfrequencies. On top of this, the encapsulation of those

devices in a fiber-based setup can become the answer on how to apply electrical connections on a fiber tip, leading potentially to many electrically actuated fiber devices.

Phase change materials like chalcogenides, are well establish materials in electronic industry. Recent efforts have revealed that those materials can be adopted in the photonic industry as well. Here is presented for first time that a single layer of GST only, without the use of noble metals can be a photonic switch with the flick of a light. Further work should be done on the electrical actuation of those devices and also the optimization of the number of the amorphous-crystalline cycles. GST has now been set as a new material for dielectric metamaterials and could create a strong impact in nonlinear functionalities based on its refractive index difference between amorphous and crystalline state. Furthermore, plasmonic behavior of these type of materials in visible regime could be of high interest from companies working on plasmonic applications or as optical switches in visible/ NIR with reflection contrast ratios up to 5, controlled by films thickness and period of the nano-gratings.

Diamond metamaterials are presented here for first time as coherent absorbers. Due to high doping with gallium ions these novel nanostructures present a broad absorption across the entire visible-NIR spectrum. The coherent modulation of optical-cycle (6 fs) pulse durations by 40% has been demonstrated here. Furthermore, this concept could be extended in atto-second responses for doped semiconductors. Apart from that, doping of Diamond with other elements of the periodic table can lead to a variation of the refractive index of the undoped material, and moreover other properties like photoluminescnse with most prominent those of nitrogen vacancies could lead to the engage of metamaterials with quantum applications.

Overall this Thesis was a 4-year effort towards nonlinear and switchable nanophotonic devices. Experimental techniques like thin film deposition, nanostructuring by Focused Ion Beam, numerical modelling of optical responses, electrical characterization and pump-probe measurements have been used to provide novel nonlinear switchable nanophotonic responses. So far two scientific papers have been published [118], [119], one more is under review entitled: "*Ultrafast coherent absorption in Diamond metamaterials"* while another two papers are submitted with title *"An near-infrared electro-optical dielectric nano-mechanical metamaterial fiber coupled modulator"* and "*Phase-Change-Driven Plasmonic-Dielectric Transitions in Colour tunable Chalcogenide Metasurfaces"*, see Appendix E.

Appendix

A. Focused Ion Beam Milling

Focused ion beam milling is a prototype lithographic technique where a strong electromagnetic field causes the emission of positively charged ions which sputter the target material. The FIB system has found extensive use in the last decade, especially in various aspects of integrated circuit fabrication processes. The aspects of the FIB which are important are its ability to remove via sputtering and add via ion induced deposition materials at sub-micron dimensions. FIB systems are now used to perform a variety of critical tasks such as design modification, failure analysis, defect characterization, and process control functions. [178]

Focused ion beam (FIB) systems have been produced commercially for approximately thirty years by Escovitz, Levi-Setti, Orloff, Swanson, primarily for large semiconductor manufacturers. FIB systems are available from ZEISS, ThermoFischer Scientific, Hitachi, Raith. Mainly developed in 1970's and 80's with sources usually used made by Liquid Metal Ion Sources (LMIS), e.g.: Ga, Au, Be, Si, Pd, B, P, As, Ni, Sb, alloys. Gas Ion Field sources used as well, with light elements like H^+, H_2^+, He^+, Ne^+…

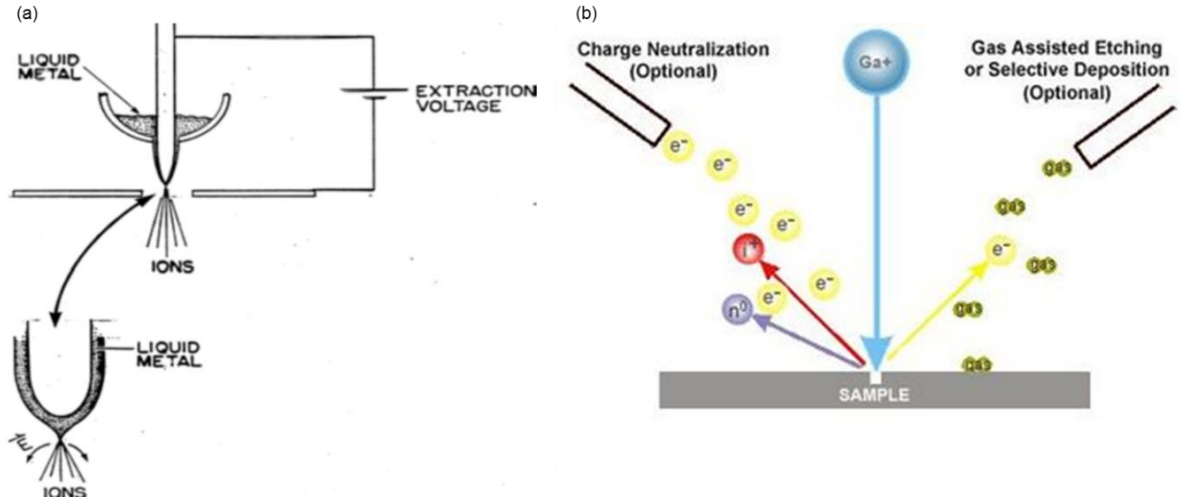

Figure A.1 Shematic sketch of Focused Ion Beam principle. (a) Acceleration scheme of LMIS, typical potential difference, from 1 to 30keV. (b) Highly accelerated ions sputter material from sample

As the diagram on figure A. 1, the gallium (Ga^+) primary ion beam hits the sample surface and sputters a small amount of material, which leaves the surface as either secondary ions (i^+ or i^-) or neutral atoms (n^0). The primary beam also produces secondary electrons (e^-). As the primary beam rasters on the sample surface, the signal from the sputtered ions or secondary electrons

is collected to form an image. Long life of the Ga source up to 1500 h, makes it more preferable than other ion sources.

At low primary beam currents, very little material is sputtered and modern FIB systems can easily achieve 5 nm imaging resolution (imaging resolution with Ga ions is limited to ~5 nm by sputtering [178]and detector efficiency). At higher primary currents, a great deal of material can be removed by sputtering, allowing precision milling of the specimen down to a sub-micrometer or even to nano-scale.

If the sample is non-conductive, a low energy electron flood gun can be used to provide charge neutralization. Alternative a thin metallic film can be used as a mask to avoid the charging effect.

The FIB system used for the completion of this Thesis was a dual system FEI Helios NanoLab600 contain both an Ion gun and and electron gun to perform imaging,scanning electron microscopy, SEM.

B. Reflection ellipsometry

Ellipsometry is an optical technique for investigating the dielectric properties (complex refractive index or dielectric function) of thin films. Ellipsometry measures the change of polarization upon reflection or transmission and compares it to a model.

It can be used to characterize composition, roughness, thickness (depth), crystalline nature, doping concentration, electrical conductivity and other material properties. It is very sensitive to the change in the optical response of incident radiation that interacts with the material being investigated.

The measured signal is the change in polarization as the incident radiation (in a known state) interacts with the material structure of interest (reflected, absorbed, scattered, or transmitted). The polarization change is quantified by the amplitude ratio, Ψ, and the phase difference, Δ (defined below). Because the signal depends on the thickness as well as the material properties, ellipsometry can be a universal tool for contact free determination of thickness and optical constants of films of all kinds. [179]

Upon the analysis of the change of polarization of light, ellipsometry can yield information about layers that are thinner than the wavelength of the probing light itself, even down to a single atomic layer. Ellipsometry can probe the complex refractive index or dielectric function tensor, which gives access to fundamental physical parameters like those listed above. It is commonly used to characterize film thickness for single layers or complex multilayer stacks ranging from a few angstroms or tenths of a nanometer to several micrometers with an excellent accuracy.

Upon the analysis of the change of polarization of light, ellipsometry can yield information about layers that are thinner than the wavelength of the probing light itself, even down to a

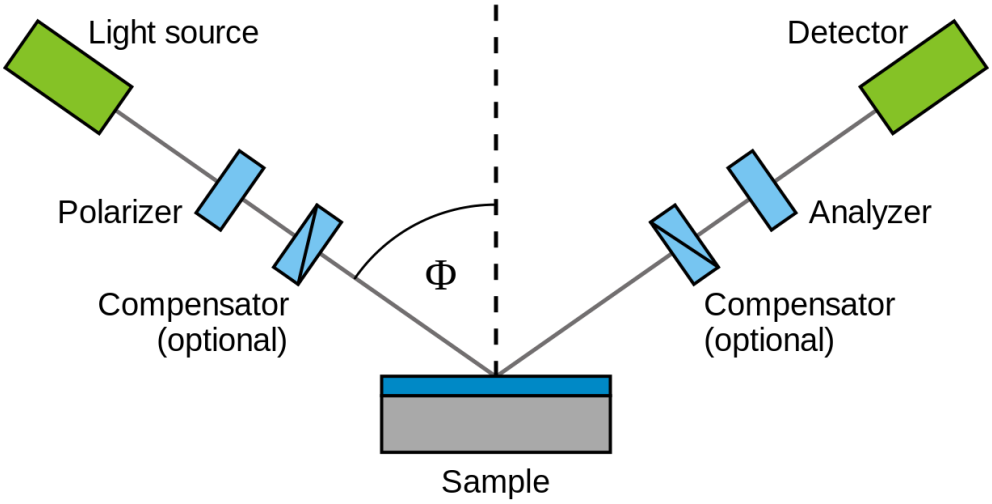

Figure B.1 Schematic setup of an ellipsometry experiment.

single atomic layer. Electromagnetic radiation is emitted by a light source and linearly polarized by a polarizer. It can pass through an optional compensator (retarder, quarter wave plate) and falls onto the sample. After reflection the radiation passes a compensator (optional) and a second polarizer, which is called an analyzer, and falls into the detector. Instead of the compensators, some ellipsometers use a phase-modulator in the path of the incident light beam. Ellipsometry is a specular optical technique (the angle of incidence equals the angle of reflection). The incident and the reflected beam span the plane of incidence. Light which is polarized parallel to this plane is named p-polarized (p-polarised). A polarization direction perpendicular is called s-polarized (s-polarised), accordingly. [180]

Throughout this thesis optical constants of samples have been measured with spectroscopic ellipsometry (J. A. Woollam 4000).

C. Microspectroscopy

The visible-NIR microspectrophotometer is used to obtain the spectrum of metallic or dialectric samples. It can measure transmittance, reflectance, with linear polarized or no-polarized light in areas of several sizes from few up to tens of micrometers.

The microspectrophotometer combines an optical microscope and a highly sensitive spectrophotometer. In figures C.1 and C.2 schematic sketch of the optical path under reflection or transmission measurements, respectively. All the samples characterized experimentaly within this |Thesis have been characterized by such device, with Transmission measurements I obtain reference the air, while for reflection measurements a silver mirror is used with Reflectivity higher than 98%. Afterwards, Absorption of the samples is calculated based on the relation A=1-T-R.

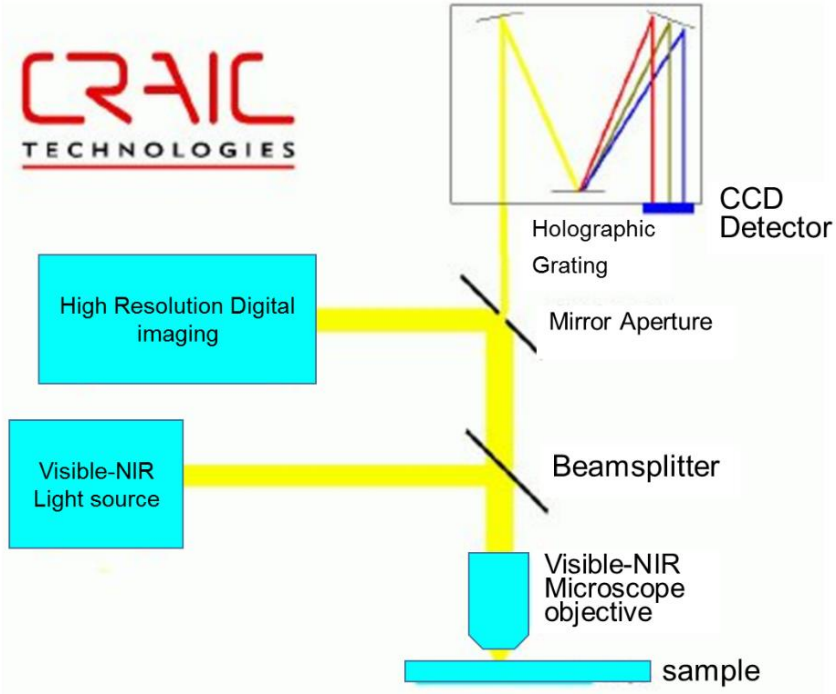

Figure C.1 General diagram of a Reflection microspectrophotometer.

In a microspectrophotometer, such as those made by CRAIC Technologies, the spectrophotometer is integrated with a specially designed microscope. The microscope optics and light sources are able to operate in the visible and near infrared regions, with the use of two photodetectors 400-900nm and 900-2000nm. As such, microspectrophotometers are very

flexible instruments able to measure absorbance, transmittance, reflectance spectra of even sub-micron sized samples. [181]

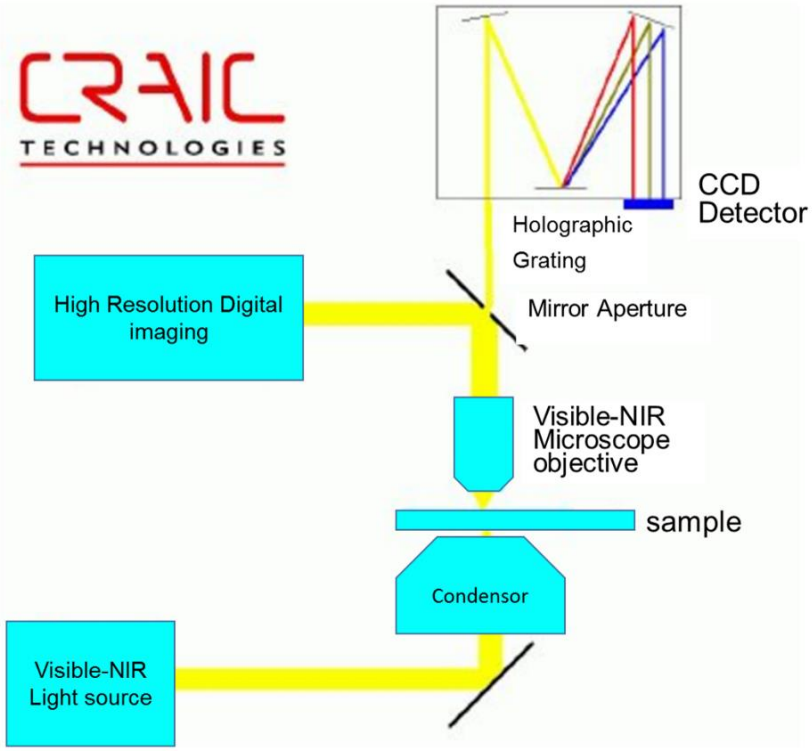

Figure C.2 General diagram of a Transmission microspectrophotometer.

D. Comsol MultiPhysics

Throughout this Thesis numerical simulations conducted with 3.5a.Comsol Multiphysics, and specifically with the use of the following modules: RF, structural and AC/DC. The first module has been used to model either 3D or 2D periodic structures and their optical response. Photonic metamaterials optical behaviour at wavelengths similar or larger than the period of the structure are modelled either with three dimensional or two dimensional numerical simulations, depending the symmetry of the structure. COMSOL Multiphysics is a finite element analysis, solver and simulation software package for various physics and engineering applications.

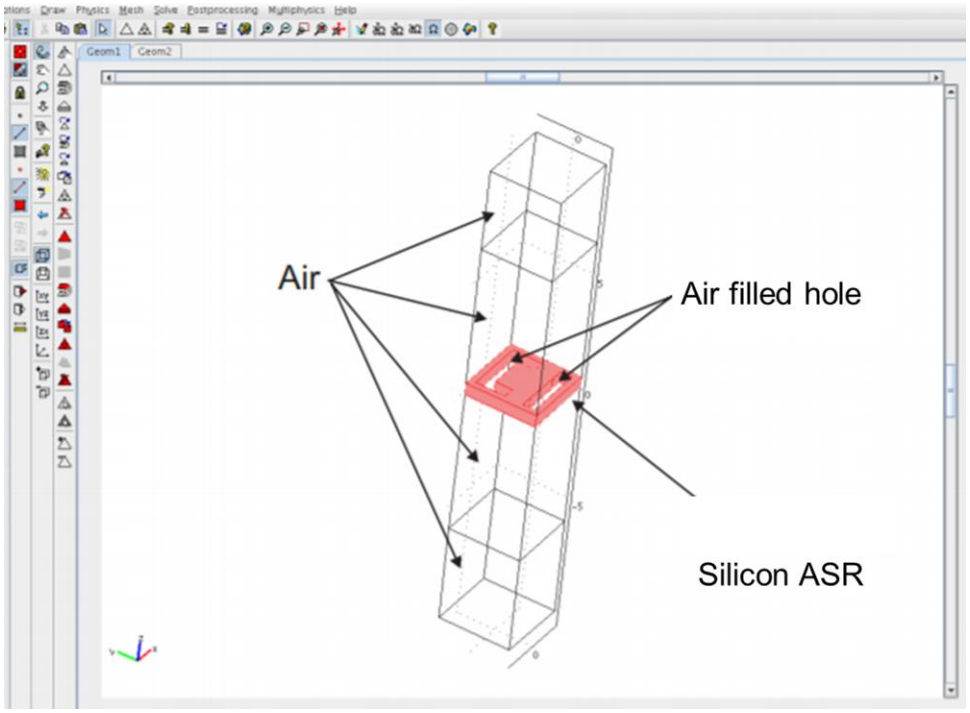

Figure D.1 Geometry of metamaterials unit cell in Comsol. Typical Comsol model of a free-standing ASR design as calculated in Chapter 2, for dielectric optomechanical metamaterials.

RF module

For electromagnetic simulations, its RF Module is employed. First, in order to model a metamaterial in COMSOL is to define the structure, based on obtained SEM images. Metamaterials studied in this thesis are periodic, planar array of ASR, holes or nanowires. As a result only one meta-molecule with periodical boundary conditions in the in-plane direction is needed to model its optical properties. Fig. D.1 is a characteristic example of a unit cell in COMSOL for a dielectric metamaterial, which optical spectra has been shown in Figure 2.9. The metamaterial consists of a 100nm thick nanostructure surrounded by air blocks on each side, each of 1050 × 1050 ‘nm’ in cross-section. Afterwards, material properties such as

refractive index (n) and extinction ratio (k) needs to be employed, while boundary conditions needs to be periodic for both x- and y- directions (for ‘type of periodicity’, ‘continuity’ is chose for radiation at normal incidence. In the out of plane direction, scattering boundary conditions or ports are employed. Internal boundary conditions are set to ‘continuity’ by default. An incident plane wave can be apply by defining an incident field at the scattering boundary, with certain polarization component.

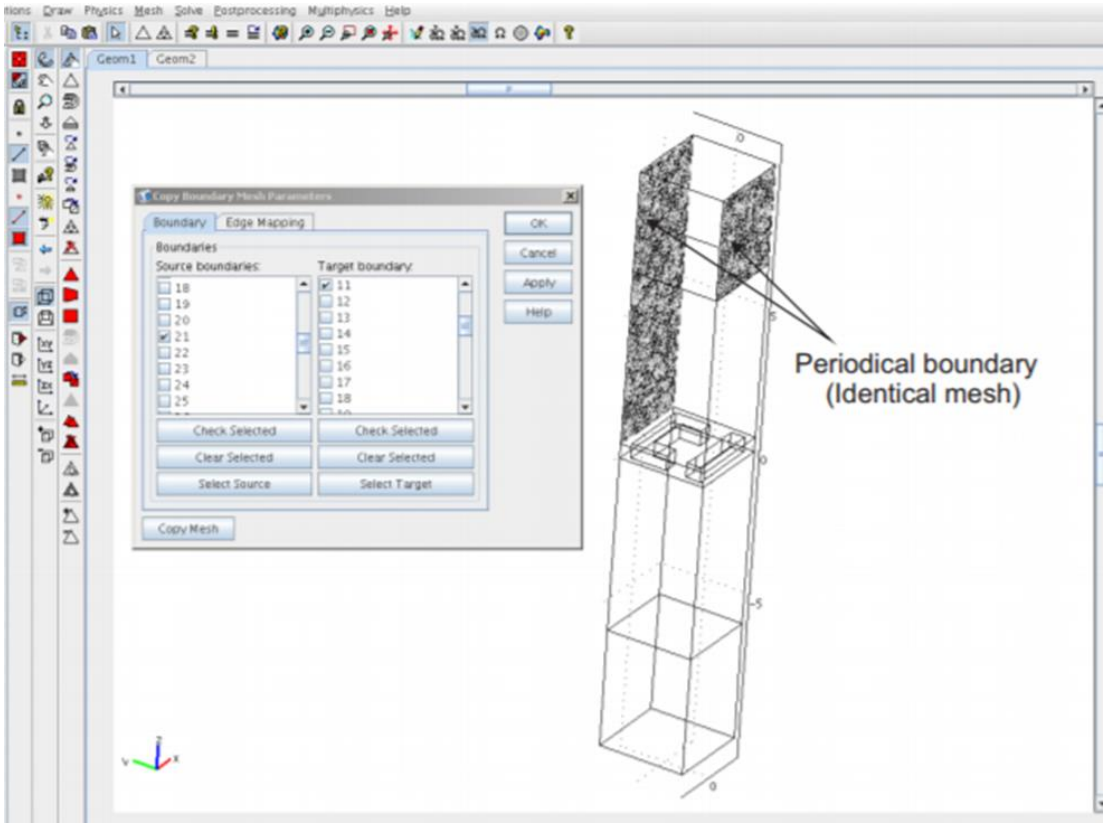

Figure D.2 Copied mesh for opposite (periodic) boundaries.

As long as the mesh properties, maximum element size in each domain should be one tenth of wavelength or smaller (this means mesh in domains with high refractive index should be finer than in the air, be meshed first). For dielectric areas, the mesh element size needs to be 4 times smaller than the smaller dimensions of the volume. Another check of the reliability of the simulated results can be obtained after perform the simulation of the same structure for two diferent messh sizes. If for both cases the simulated result deviates less than 1%, then the less dense mesh is still valid. The element size of mesh may be limited by the capability of simulation platforms (COMSOL simulations in this thesis are performed with a 16 processor, 64 bit, 128 GB linux workstation). For periodical boundary conditions, it must ensure that mesh nodes on each pair of periodical boundaries are copied, (see Fig. D.2). When the simulation

wavelength is set, all the materials properties in domains and boundary conditions are defined, and mesh have completed, one only needs to set suitable solver parameters and starts running the simulation, across the spectrum of interest. When the modelling completes, electromagnetic field distributions can be obtained directly by post-processing while transmission, reflection and absorption data can be calculated via data of power flow at the boundaries.

Structural mechanics

For mechanical simulations, the structural mechanics module is employed. First, in order to model a metamaterial in COMSOL is necessary to define the structure, based on obtained SEM images. Materials studied in this Thesis are considered stress free, and with uniform density with values for Young's modulus and density obtained from literature. For nano-mechanical metamaterials the study of a single mechanical resonator is enough to capture the mechanical response of the unit cell deformation. Mechanical coupling among unit cells is being ignored since every unit cell realizes forced harmonic oscillation driven by the same force (light). Figure D.3 is presented a characteristic example of a unit cell in COMSOL for a dielectric nano-wire, which mechanical properties are adjusted as it shown in Figure D.3b. The metamaterial consists of a 170nm thick nanowire. Afterwards, material properties such as Young modulus and density need to be employed, while boundary conditions need to be either fixed or free depending the case. Deformation of the beam can be calculated under the constant load acting on the nano-wire, or eigenfrequency solver can calculate the mechanical eigenfrequencies of the nano-structures.

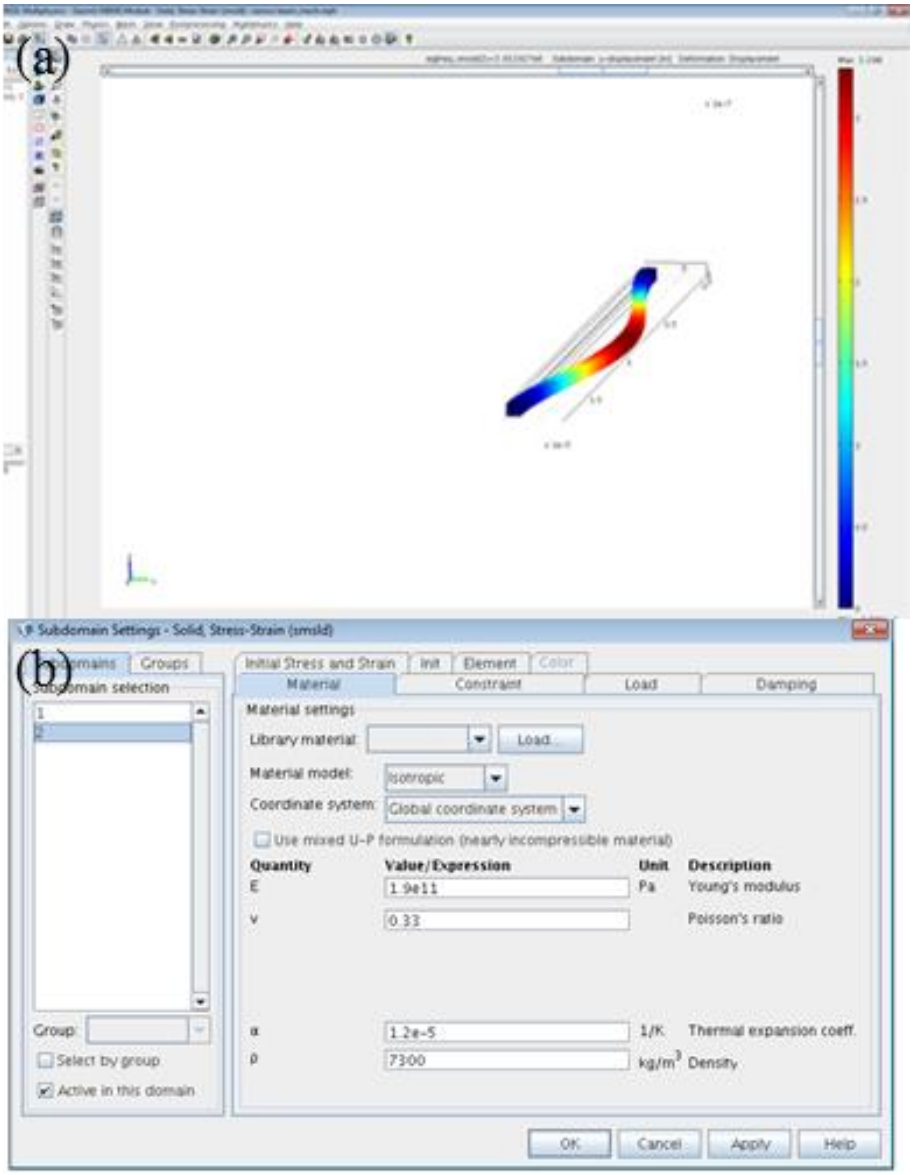

Figure D.3 Mechanical model of a signle nanowire. (a) 1 mechanical eigenmode displacement, (b) material properties introduced for every material used.

E. Publications

Articles:

1. All-dielectric phase-change reconfigurable metasurface
A. Karvounis, B. Gholipour, K. F. MacDonald, and N. I. Zheludev. Appl. Phys. Lett. 109, 051103 (2016).

2. Nano-optomechanical nonlinear dielectric metamaterials
A. Karvounis, J. Y. Ou, W. Wu, K. F. MacDonald, N. I. Zheludev. Appl. Phys. Lett. 107, 191110 (2015).

3. Ultrafast coherent absorption of Diamond metamaterials
A. Karvounis, V. Nalla, K. F. McDonald, N. I. Zheludev. Adv. Mater. 30, 1–6 (2018).

4. Phase-Change-Driven Plasmonic-Dielectric Transitions in Colour tunable Chalcogenide Metasurfaces
B. Gholipour, A. Karvounis, J. Yin, C. Soci, K. F. MacDonald and N. I. Zheludev
NPG Asia Mater. 0–6 (2018). doi:10.1038/s41427-018-0043-4

5. Large electro-optical effect through electrostriction in a nano-mechanical metamaterial
A. Karvounis, B. Gholipour, K. F. MacDonald, N. I. Zheludev, **(submitted)**

Conference Contributions:

(**invited**) *Coherent information processing on metasurfaces at 40 Gbit/s and beyond*. E. Plum, M. Papaioannou, A. Xomalis, A. Karvounis, V. Nalla, I. Demirtzioglou, Y. Jung, K. F. MacDonald, C. Lacava, P. Petropoulos, D. J. Richardson, and N. I. Zheludev. PIERS 2017, Singapore, Singapore, 19 - 22 Nov 2017

(**invited**) *Merging metamaterial and optical fiber technologies*. N. I. Zheludev, K. F. MacDonald, E. Plum, A. Karvounis, D. Piccinotti, A. Xomalis, I. Demirtzioglou, V. Savinov, B. Gholipour, Y. Jung, P. Petropoulos, and D. J. Richardson. META2017, Seoul, South Korea, 25 - 28 Jul 2017

(**invited**) *Merging photonic metamaterial and optical fiber technologies*. A. Xomalis, D. Piccinotti, A. Karvounis, I. Demirtzioglou, V. Savinov, B. Gholipour, J. Y. Ou, Y. Jung, E. Plum, P. Petropoulos, K. F. MacDonald, D. J. Richardson, and N. I. Zheludev. Integrated Photonics Research, Silicon, and Nano-Photonics, New Orleans, LA, USA, 24 - 27 Jul 2017

Optical bistability in optomechanical metamaterial at sub-milliwatt power levels. J. Y. Ou, A. Karvounis, K. F. MacDonald, and N. I. Zheludev. CLEO Europe - EQEC 2017 , Munich, Germany 25 - 29 Jun 2017

(**invited**) Optomechanical metasurfaces. E. Plum, J. Y. Ou, A. Karvounis, K. F. MacDonald, and N. I. Zheludev. OSA Incubator Meeting on Materials for Optomechanical Actuation, Washington DC, USA, 25-27 Jun 2017

Ultrafast Regimes of Coherent Absorption in Plasmonic and Dielectric Diamond-based Metasurfaces V. Nalla, A. Karvounis, J. Valente, H. D. Sun, and N. I. Zheludev. ICMAT2017, Singapore, 18 - 23 Jun 2017

(**invited**) Merging metamaterial and fiber technologies. J. Y. Ou, A. Karvounis, A. Xomalis, V. Savinov, E. Plum, K. F. MacDonald, and N. I. Zheludev. 8th International Conference on Surface Plasmon Photonics (SPP8), Taipei, Taiwan, 22-26 May 2017

(poster) 100 THz bandwidth optical modulators via cohorent absorption of metamaterial. V. Nalla, A. Karvounis, J. Valente, H. Sun, and N. I. Zheludev. IPS Meeting 2017, Singapore, 22 - 24 Feb 2017

Fibre-coupled photonic metadevices. A. Xomalis, D. Piccinotti, A. Karvounis, H. Zhang, V. Savinov, B. Gholipour, Y. Jung, A. C. Peacock, E. Plum, K. F. MacDonald, D. J. Richardson, and N. I. Zheludev Nanometa 2017, Seefeld, Austria, 4 - 7 Jan 2017

(poster) Plasmonic response of chalcogenides and switchable all-dielectric metamaterials. B. Gholipour, D. Piccinotti, J. Yao, A. Karvounis, J. Yin, C. Soci, B. E. Hayden, K. F. MacDonald, N. I. Zheludev. Nanometa 2017, Seefeld, Austria, 4 - 7 Jan 2017

(poster) Intrinsic optical bistability in nanomechanical metamaterials at milliwatt power levels
J. Y. Ou, A. Karvounis, K. F. MacDonald, N. I. Zheludev
Nanometa 2017, Seefeld, Austria, 4 - 7 Jan 2017

All-chalcogenide Phase-Change Plasmonics
B. Gholipour, A. Karvounis, J. Yin, C. Soci, K. F. MacDonald, and N. I. Zheludev
Metamaterials 2016, Crete, Greece, 17 - 22 Sep 2016

(poster) Nanomechanically Reconfigurable All-dielectric Metasurfaces for Sub-GHz Optical Modulation
A. Karvounis, J. Y. Ou, B. Gholipour, K. F. MacDonald, and N. I. Zheludev
Metamaterials 2016, Crete, Greece, 17 - 22 Sep 2016
[Awarded best poster by Metamaterials, Inc. (MTI)]

All-dielectric nanomechanical metamaterials for sub-GHz optical modulation
A.Karvounis, J. Y. Ou, B.Gholipour, K.F.MacDonald, and N.I.Zheludev
Photon '16, Leeds, 5-8 Sep 2016

(**invited**) Metamaterials reconfigurable with light
A. Karvounis, J. Y. Ou, E. Plum, K. F. MacDonald, and N. I. Zheludev
SPIE Optics & Photonics 2016, San Diego, USA, 28 Aug - 1 Sep 2016

(poster) Sub-GHz Modulation of Light with Dielectric Nanomechanical Metamaterials
A. Karvounis, J. Y. Ou, B. Gholipour, W. Wu, K. F. MacDonald, and N. I. Zheludev
CLEO 2016, San Jose, CA, USA, 5 - 10 June 2016

(poster) All-dielectric nanomechanical metamaterials
A. Karvounis, J. Y. Ou, B. Gholipour, K. F. MacDonald, and N. I. Zheludev

New Horizons in Nanophotonics, Chicheley, UK, 23 - 24 May 2016

(poster) All-chalcogenide phase-change metasurfaces
B. Gholipour, A. Karvounis, K. F. MacDonald, and N. I. Zheludev
New Horizons in Nanophotonics, Chicheley, UK, 23 - 24 May 2016

(**invited**) All-dielectric nano-optomechanical nonlinear metamaterials
A. Karvounis, J. Y. Ou, W. Wu, K. F. MacDonald, N. I. Zheludev
SPIE Photonics Europe 2016, Brussels, Belgium, 3 - 7 Apr 2016

(**invited**) Reconfigurable nanomembrane metadevices
E. Plum, J. Valente, J. Y. Ou, P. Cencillo-Abad, A. Karvounis, K. F. MacDonald, and N. I. Zheludev
9th International Conference on Nanophotonics (ICNP 2016), Taipei, Taiwan, 21 - 25 Mar 2016

(**invited**) Nano-optomechanical dielectric metasurfaces reconfigurable with light
A. Karvounis, J. Y. Ou, D. Piccinotti, W. Wu, E. Plum, K. F. MacDonald, and N. I. Zheludev
Materials Research Society MRS 2015 Fall Meeting & Exhibit, Boston, MA, USA, 29 Nov - 4 Dec 2015

Optically reconfigurable metadevices based on phase-change materials
Q. Wang, A. Karvounis, E. T. F. Rogers, B. Gholipour, Y. Guanghui, K. F. MacDonald, and N. I. Zheludev
Metamaterials 2015, Oxford, UK, 7 - 12 Sep 2015

All-dielectric nano-opto-mechanical metasurfaces
A. Karvounis, W. Wu, K. F. MacDonald, and N. I. Zheludev
Metamaterials 2015, Oxford, UK, 7 - 12 Sep 2015

(**invited**) Nanostructured photonic metamaterials reconfigurable with light, nanomechanical and electromagnetic forces
J. Y. Ou, J. Valente, A. Karvounis, W. Wu, E. Plum, K. F. MacDonald, and N. I. Zheludev
SPIE Optics & Photonics 2015, San Diego, CA, USA, 9 - 13 Aug 2015 - pdf

(**invited**) Optical forces in plasmonic and dielectric metamaterials
E. Plum, J. Y. Ou, A. Karvounis, W. Wu, K. F. MacDonald, and N. I. Zheludev
META2015, New York, NY, USA, 4 - 7 Aug 2015

Nano-opto-mechanical nonlinear dielectric metamaterials
A. Karvounis, W. Wu, K. F. MacDonald, and N. I. Zheludev
CLEO/Europe-EQEC 2015, Munich, Germany 21 - 25 Jun 2015

(**invited**) Optically switchable and rewritable phase-change (dielectric) metamaterials
Q. Wang, A. Karvounis, B. Gholipour, W. Wu, E. T. F. Rogers, K. F. MacDonald, and N. I. Zheludev
2015 MRS Spring Meeting, San Francisco, CA, USA Apr 6 - 10 2015

(**invited**) Giant nonlinearities in plasmonic and dielectric reconfigurable metamaterials
N. I. Zheludev, K. F. MacDonald, E. Plum, J.-Y. Ou, J. Valente, A. Karvounis, W. Wu

References

[1] M. I. Tribelsky, “Resonant scattering of light by small particles,” *Sov. Phys. JETP*, vol. 59 (3), no. March, pp. 534–536, 1984.

[2] M. I. Tribelsky and B. S. Luk’yanchuk, “Anomalous light scattering by small particles,” *Phys. Rev. Lett.*, vol. 97, no. 26, pp. 1–4, 2006.

[3] A. I. Kuznetsov, A. E. Miroshnichenko, Y. H. Fu, J. Zhang, and B. Luk’yanchuk, “Magnetic light,” *Sci. Rep.*, vol. 2, p. 492, 2012.

[4] Z. B. Wang, B. S. Luk’Yanchuk, M. H. Hong, Y. Lin, and T. C. Chong, “Energy flow around a small particle investigated by classical Mie theory,” *Phys. Rev. B - Condens. Matter Mater. Phys.*, vol. 70, no. 3, pp. 1–12, 2004.

[5] A. . Evlyukhin and S. I. Bozhevol’nyi, “Applicability conditions for the dipole approximation in the problems of scattering of surface plasmon polaritons,” *JETP Lett.*, vol. 81, no. 5, pp. 278–282, 2005.

[6] A. I. Kuznetsov, A. E. Miroshnichenko, M. L. Brongersma, Y. S. Kivshar, and B. Lukyanchuk, “Optically resonant dielectric nanostructures,” *Science (80-.).*, vol. 354, no. 6314, p. aag2472-aag2472, 2016.

[7] A. Ahmadi and H. Mosallaei, “Physical configuration and performance modeling of all-dielectric metamaterials,” *Phys. Rev. B - Condens. Matter Mater. Phys.*, vol. 77, no. 4, pp. 1–11, 2008.

[8] S. Liu *et al.*, “Realization of tellurium-based all dielectric optical metamaterials using a multi-cycle deposition-etch process,” *Appl. Phys. Lett.*, vol. 102, no. 16, 2013.

[9] J. A. Schuller, R. Zia, T. Taubner, and M. L. Brongersma, “Dielectric metamaterials based on electric and magnetic resonances of silicon carbide particles,” *Phys. Rev. Lett.*, vol. 99, no. 10, pp. 1–4, 2007.

[10] E. A. Semouchkina, G. B. Semouchkin, M. Lanagan, and C. A. Randall, “FDTD study of resonance processes in metamaterials,” *IEEE Trans. Microw. Theory Tech.*, vol. 53, no. 4 II, pp. 1477–1486, 2005.

[11] A. B. Evlyukhin *et al.*, “Demonstration of magnetic dipole resonances of dielectric nanospheres in the visible region,” *Nano Lett.*, vol. 12, no. 7, pp. 3749–3755, 2012.

[12] S. Jahani and Z. Jacob, “All-dielectric metamaterials,” *Nat. Publ. Gr.*, vol. 11, no. 1, pp. 23–36, 2016.

[13] V. Veselago, “Electrodynamics of Substances with Simultaneously Negative Values ε and μ,” *Sov. Phys. Usp. 10, 509*, 1968.

[14] J. B. Pendry, “Negative refraction makes a perfect lens,” *Phys. Rev. Lett.*, vol. 85, no. 18, pp. 3966–3969, 2000.

[15] R. Shelby, D. R. Smith, and S. Schultz, “Experimental verification of a negative index of refraction.,” *Science (80-.).*, vol. 292, no. 5514, pp. 77–9, 2001.

[16] B. Hecht, H. Bielefeldt, L. Novotny, Y. Inouye, and D. Pohl, “Local Excitation, Scattering, and Interference of Surface Plasmons,” *Phys. Rev. Lett.*, vol. 77, no. 9, pp. 1889–1892, 1996.

[17] S. A. Maier, M. L. Brongersma, P. G. Kik, S. Meltzer, A. A. G. Requicha, and H. A. Atwater, “Plasmonics - A route to nanoscale optical devices,” *Adv. Mater.*, vol. 13, no. 19, pp. 1501–1505, 2001.

[18] W. L. Barnes, A. Dereux, and T. W. Ebbesen, “Surface plasmon subwavelength optics,” *Nature*, vol. 424, no. 6950, pp. 824–30, 2003.

[19] S. Science, N. Series, and G. Crater, “Metamaterials and Negative Refractive Index Author (s): D . R .

Smith , J . B . Pendry and M . C . K . Wiltshire," vol. 305, no. 5685, pp. 788–792, 2015.

[20] V. A. Fedotov, P. L. Mladyonov, S. L. Prosvirnin, and N. I. Zheludev, "Planar electromagnetic metamaterial with a fish scale structure," *Phys. Rev. E - Stat. Nonlinear, Soft Matter Phys.*, vol. 72, no. 5, pp. 1–4, 2005.

[21] A. S. Schwanecke, V. A. Fedotov, V. V Khardikov, S. L. Prosvirnin, Y. Chen, and N. I. Zheludev, "Optical magnetic mirrors," *J. Opt. A Pure Appl. Opt.*, vol. 9, no. 1, pp. L1–L2, 2007.

[22] V. A. Fedotov, P. L. Mladyonov, S. L. Prosvirnin, A. V. Rogacheva, Y. Chen, and N. I. Zheludev, "Asymmetric propagation of electromagnetic waves through a planar chiral structure," *Phys. Rev. Lett.*, vol. 97, no. 16, pp. 1–4, 2006.

[23] V. A. Fedotov, M. Rose, S. L. Prosvirnin, N. Papasimakis, and N. I. Zheludev, "Sharp trapped-mode resonances in planar metamaterials with a broken structural symmetry," *Phys. Rev. Lett.*, vol. 99, no. 14, pp. 1–4, 2007.

[24] G. V. Naik, V. M. Shalaev, and A. Boltasseva, "Alternative plasmonic materials: Beyond gold and silver," *Adv. Mater.*, vol. 25, no. 24, pp. 3264–3294, 2013.

[25] A. Boltasseva and H. a Atwater, "Low-Loss Plasmonic Metamaterials," *Science (80-.).*, vol. 331, no. 6015, pp. 290–291, 2011.

[26] Y. Yang, I. I. Kravchenko, D. P. Briggs, and J. Valentine, "All-dielectric metasurface analogue of electromagnetically induced transparency.," *Nat. Commun.*, vol. 5, p. 5753, 2014.

[27] C. Wu *et al.*, "Spectrally selective chiral silicon metasurfaces based on infrared Fano resonances.," *Nat. Commun.*, vol. 5, no. May, p. 3892, 2014.

[28] K. Vynck, D. Felbacq, E. Centeno, A. I. Căbuz, D. Cassagne, and B. Guizal, "All-dielectric rod-type metamaterials at optical frequencies," *Phys. Rev. Lett.*, vol. 102, no. 13, pp. 1–4, 2009.

[29] a García-Etxarri *et al.*, "Strong magnetic response of submicron silicon particles in the infrared.," *Opt. Express*, vol. 19, no. 6, pp. 4815–4826, 2011.

[30] L. Shi, T. U. Tuzer, R. Fenollosa, and F. Meseguer, "A new dielectric metamaterial building block with a strong magnetic response in the sub-1.5-micrometer region: Silicon colloid nanocavities," *Adv. Mater.*, vol. 24, no. 44, pp. 5934–5938, 2012.

[31] L. Peng, L. Ran, H. Chen, H. Zhang, J. A. Kong, and T. M. Grzegorczyk, "Experimental observation of left-handed behavior in an array of standard dielectric resonators," *Phys. Rev. Lett.*, vol. 98, no. 15, pp. 1–4, 2007.

[32] B. I. Popa and S. A. Cummer, "Compact dielectric particles as a building block for low-loss magnetic metamaterials," *Phys. Rev. Lett.*, vol. 100, no. 20, pp. 1–4, 2008.

[33] Q. Zhao, J. Zhou, F. Zhang, and D. Lippens, "Mie resonance-based dielectric metamaterials," *Mater. Today*, vol. 12, no. 12, pp. 60–69, 2009.

[34] J. C. Ginn *et al.*, "Realizing optical magnetism from dielectric metamaterials," *Phys. Rev. Lett.*, vol. 108, no. 9, pp. 1–5, 2012.

[35] L. Shi *et al.*, "Monodisperse silicon nanocavities and photonic crystals with magnetic response in the optical region.," *Nat. Commun.*, vol. 4, no. May, p. 1904, 2013.

[36] J. Zhang, K. F. MacDonald, and N. I. Zheludev, "Near-infrared trapped mode magnetic resonance in an all-dielectric metamaterial," *Opt. Express*, vol. 21, no. 22, p. 26721, 2013.

[37] P. Moitra, Y. Yang, Z. Anderson, I. I. Kravchenko, D. P. Briggs, and J. Valentine, "Realization of an

all-dielectric zero-index optical metamaterial," *Nat. Photonics*, vol. 7, no. August, pp. 1–5, 2013.

[38] M. I. Shalaev, J. Sun, A. Tsukernik, A. Pandey, K. Nikolskiy, and N. M. Litchinitser, "High-Efficiency All-Dielectric Metasurfaces for Ultracompact Beam Manipulation in Transmission Mode," *Nano Lett.*, vol. 15, no. 9, pp. 6261–6266, 2015.

[39] A. Arbabi, Y. Horie, M. Bagheri, and A. Faraon, "Dielectric metasurfaces for complete control of phase and polarization with subwavelength spatial resolution and high transmission," *Nat. Nanotechnol.*, vol. 10, no. 11, pp. 937–943, 2015.

[40] M. Decker *et al.*, "High-Efficiency Dielectric Huygens' Surfaces," *Adv. Opt. Mater.*, vol. 3, no. 6, pp. 813–820, 2015.

[41] D. Lin, P. Fan, E. Hasman, and M. L. Brongersma, "Dielectric gradient metasurface optical elements," *Science (80-.).*, vol. 345, no. 6194, pp. 298–302, 2014.

[42] M. Khorasaninejad *et al.*, "Metalenses at visible wavelengths: Diffraction-limited focusing and subwavelength resolution imaging.," *Science*, vol. 352, no. 6290, pp. 1190–4, 2016.

[43] Y. Yang *et al.*, "Nonlinear Fano-Resonant Dielectric Metasurfaces," *Nano Lett.*, vol. 15, no. 11, pp. 7388–7393, 2015.

[44] S. Liu *et al.*, "Resonantly Enhanced Second-Harmonic Generation Using III-V Semiconductor All-Dielectric Metasurfaces," *Nano Lett.*, vol. 16, no. 9, pp. 5426–5432, 2016.

[45] L. Huang, Y. Yu, and L. Cao, "General modal properties of optical resonances in subwavelength nonspherical dielectric structures," *Nano Lett.*, vol. 13, no. 8, pp. 3559–3565, 2013.

[46] S. Campione *et al.*, "Broken Symmetry Dielectric Resonators for High Quality Factor Fano Metasurfaces," *ACS Photonics*, vol. 3, no. 12, pp. 2362–2367, 2016.

[47] V. A. Fedotov *et al.*, "Spectral collapse in ensembles of metamolecules," *Phys. Rev. Lett.*, vol. 104, no. 22, pp. 1–4, 2010.

[48] Y. H. Fu, A. I. Kuznetsov, A. E. Miroshnichenko, Y. F. Yu, and B. Luk'yanchuk, "Directional visible light scattering by silicon nanoparticles," *Nat. Commun.*, vol. 4, p. 1527, 2013.

[49] I. Staude and J. Schilling, "Metamaterial-inspired silicon nanophotonics," *Nat. Photonics*, vol. 11, no. 5, pp. 274–284, 2017.

[50] A. Zhan, S. Colburn, R. Trivedi, T. K. Fryett, C. M. Dodson, and A. Majumdar, "Low-Contrast Dielectric Metasurface Optics," *ACS Photonics*, vol. 3, no. 2, pp. 209–214, 2016.

[51] M. Khorasaninejad *et al.*, "Visible Wavelength Planar Metalenses Based on Titanium Dioxide," *IEEE J. Sel. Top. Quantum Electron.*, vol. 23, no. 3, 2017.

[52] P. Gutruf, C. Zou, W. Withayachumnankul, M. Bhaskaran, S. Sriram, and C. Fumeaux, "Mechanically tunable dielectric resonator metasurfaces at visible frequencies," *ACS Nano*, vol. 10, no. 1, pp. 133–141, 2016.

[53] J.-Y. Ou, J.-K. So, G. Adamo, A. Sulaev, L. Wang, and N. I. Zheludev, "Ultraviolet and visible range plasmonics in the topological insulator Bi1.5Sb0.5Te1.8Se1.2," *Nat. Commun.*, vol. 5, p. 5139, 2014.

[54] B. Gholipour *et al.*, "Organometallic Perovskite Metasurfaces," *Adv. Mater.*, vol. 29, no. 9, pp. 1–6, 2017.

[55] Q. Wang *et al.*, "Optically reconfigurable metasurfaces and photonic devices based on phase change materials," *Nat. Photonics*, vol. 10, no. 1, pp. 60–65, 2016.

[56] N. I. Zheludev, “Obtaining optical properties on demand,” *Science (80-.).*, vol. 348, no. 6238, pp. 973–974, 2015.

[57] M. Hochberg *et al.*, “Terahertz all-optical modulation in a silicon-polymer hybrid system.,” *Nat. Mater.*, vol. 5, no. 9, pp. 703–9, 2006.

[58] F. Y. and T. D. J. Reed G T, Mashanovich G, Gardes, “Silicon optical modulators,” *Nat. Photonics*, vol. 4, no. 8, p. 518, 2010.

[59] A. S. L. Gomes, C. B. de Araujo, A. Miliou, and R. Srivastava, “Multikilohertz all-optical modulator in semiconductor doped glass channel waveguide,” *Electron. Lett.*, vol. 29, no. 14, pp. 1246–1248, 1993.

[60] C. Rios, P. Hosseini, C. D. Wright, H. Bhaskaran, and W. H. P. Pernice, “On-chip photonic memory elements employing phase-change materials,” *Adv. Mater.*, vol. 26, no. 9, pp. 1372–1377, 2014.

[61] C. Ríos *et al.*, “Integrated all-photonic non-volatile multi-level memory,” *Nat. Photonics*, vol. 9, no. 11, pp. 725–732, 2015.

[62] N. I. Zheludev and Y. S. Kivshar, “From metamaterials to metadevices,” *Nat. Mater.*, vol. 11, no. 11, pp. 917–924, 2012.

[63] Z. So and Z. So, “Letters To Nature,” *October*, vol. 431, no. October, pp. 1081–1084, 2004.

[64] L. Ju *et al.*, “Graphene plasmonics for tunable terahertz metamaterials.,” *Nat. Nanotechnol.*, vol. 6, no. 10, pp. 630–4, 2011.

[65] W. Li *et al.*, “Ultrafast all-optical graphene modulator.,” *Nano Lett.*, vol. 14, no. 2, pp. 955–959, 2014.

[66] T. Graphene *et al.*, “Experimental Demonstration of >230 ° Phase Modulation in Gate- Tunable Graphene − Gold Recon fi gurable Mid-Infrared Metasurfaces,” 2017.

[67] J. J. Cha *et al.*, “Two-dimensional chalcogenide nanoplates as tunable metamaterials via chemical intercalation,” *Nano Lett.*, vol. 13, no. 12, pp. 5913–5918, 2013.

[68] D. H. Werner, D.-H. Kwon, I.-C. Khoo, A. V Kildishev, and V. M. Shalaev, “Liquid crystal clad near-infrared metamaterials with tunable negative-zero-positive refractive indices.,” *Opt. Express*, vol. 15, no. 6, pp. 3342–3347, 2007.

[69] J. A. Bossard *et al.*, “Tunable frequency selective surfaces and negative-zero-positive index metamaterials based on liquid crystals,” *IEEE Trans. Antennas Propag.*, vol. 56, no. 5, pp. 1308–1320, 2008.

[70] M. Kamenjicki, I. K. Lednev, and S. A. Asher, “Photoresponsive azobenzene photonic crystals,” *J. Phys. Chem. B*, vol. 108, no. 34, pp. 12637–12639, 2004.

[71] P. Kim, L. D. Zarzar, X. Zhao, A. Sidorenko, and J. Aizenberg, “Microbristle in gels: Toward all-polymer reconfigurable hybrid surfaces,” *Soft Matter*, vol. 6, no. 4, p. 750, 2010.

[72] B. F. Soares, F. Jonsson, and N. I. Zheludev, “All-optical phase-change memory in a single gallium nanoparticle,” *Phys. Rev. Lett.*, vol. 98, no. 15, pp. 1–4, 2007.

[73] T. Driscoll *et al.*, “Memory Metamaterials,” *Science (80-.).*, vol. 325, no. 5947, pp. 1518–1521, 2009.

[74] M. Wuttig, H. Bhaskaran, and T. Taubner, “Phase-change materials for non-volatile photonic applications,” *Nat. Photonics*, vol. 11, no. 8, pp. 465–476, 2017.

[75] N. I. Zheludev, “All change please!,” *Nat. Photonics*, vol. 1, no. October, p. 551, 2007.

[76] M. Aspelmeyer, T. J. Kippenberg, and F. Marquardt, “Cavity optomechanics,” *Rev. Mod. Phys.*, vol. 86,

no. 4, pp. 1391–1452, 2014.

[77] N. I. Zheludev and E. Plum, “Reconfigurable nanomechanical photonic metamaterials,” *Nat Nano*, vol. 11, no. 1, pp. 16–22, 2016.

[78] H. X. Tang, M. Li, W. H. P. Pernice, C. Xiong, T. Baehr-Jones, and M. Hochberg, “Harnessing optical forces in integrated photonic circuits,” *Nature*, vol. 456, no. 7221, pp. 480-U28, 2008.

[79] P. Rath, S. Khasminskaya, C. Nebel, C. Wild, and W. H. P. Pernice, “Diamond-integrated optomechanical circuits,” *Nat. Commun.*, vol. 4, p. 1690, 2013.

[80] L. Zhu, J. Kapraun, J. Ferrara, and C. J. Chang-Hasnain, “Flexible photonic metastructures for tunable coloration,” *Optica*, vol. 2, no. 3, pp. 255–258, 2015.

[81] A. Komar *et al.*, “Electrically tunable all-dielectric optical metasurfaces based on liquid crystals,” *Appl. Phys. Lett.*, vol. 110, no. 7, 2017.

[82] J. Sautter *et al.*, “Active tuning of all-dielectric metasurfaces,” *ACS Nano*, vol. 9, no. 4, pp. 4308–4315, 2015.

[83] R. Thijssen, E. Verhagen, T. J. Kippenberg, and A. Polman, “Plasmon nanomechanical coupling for nanoscale transduction,” *Nano Lett.*, vol. 13, no. 7, pp. 3293–3297, 2013.

[84] R. Thijssen, T. J. Kippenberg, A. Polman, and E. Verhagen, “Plasmomechanical Resonators Based on Dimer Nanoantennas,” *Nano Lett.*, vol. 15, no. 6, pp. 3971–3976, 2015.

[85] B. M. Zwickl *et al.*, “High quality mechanical and optical properties of commercial silicon nitride membranes High quality mechanical and optical properties of commercial silicon nitride membranes,” vol. 103125, no. 2008, pp. 1–4, 2013.

[86] K. E. Petersen, “Silicon as a Mechanical Material,” vol. 70, no. 5, 1982.

[87] B. B. A. Fairchild *et al.*, “Fabrication of Ultrathin Single-Crystal Diamond Membranes **,” pp. 4793–4798, 2008.

[88] V. Ginis, P. Tassin, C. M. Soukoulis, and I. Veretennicoff, “Enhancing Optical Gradient Forces with Metamaterials,” *Phys. Rev. Lett.*, vol. 110, no. 5, p. 57401, 2013.

[89] J. Zhang, K. F. MacDonald, and N. I. Zheludev, “Nonlinear dielectric optomechanical metamaterials,” *Light Sci. Appl.*, vol. 2, no. April, p. e96, 2013.

[90] J. Zhang, K. F. MacDonald, and N. I. Zheludev, “Giant optical forces in planar dielectric photonic metamaterials,” *Opt. Lett.*, vol. 39, no. 16, p. 4883, 2014.

[91] M. Liu, D. A. Powell, R. Guo, I. V. Shadrivov, and Y. S. Kivshar, “Polarization-Induced Chirality in Metamaterials via Optomechanical Interaction,” *Adv. Opt. Mater.*, pp. 1–8, 2016.

[92] S. Yun, J. A. Bossard, T. S. Mayer, and D. H. Werner, “Angle and polarization tolerant midinfrared dielectric filter designed by genetic algorithm optimization,” *Appl. Phys. Lett.*, vol. 96, no. 22, pp. 1–4, 2010.

[93] K. E. Chong *et al.*, “Observation of fano resonances in all-dielectric nanoparticle oligomers,” *Small*, vol. 10, no. 10, pp. 1985–1990, 2014.

[94] X. Meng *et al.*, “Experimental realization of all-dielectric planar chiral metamaterials with large optical activity in direct transmission,” *Thin Solid Films*, vol. 516, no. 23, pp. 8745–8748, 2008.

[95] U. Guler, a. Boltasseva, and V. M. Shalaev, “Refractory Plasmonics,” *Science (80-.).*, vol. 344, no. 6181, pp. 263–264, 2014.

[96] J. Y. Ou, E. Plum, L. Jiang, and N. I. Zheludev, “Reconfigurable photonic metamaterials,” *Nano Lett.*, vol. 11, no. 5, pp. 2142–2144, 2011.

[97] J.-Y. Ou, E. Plum, J. Zhang, and N. I. Zheludev, “An electromechanically reconfigurable plasmonic metamaterial operating in the near-infrared.,” *Nat. Nanotechnol.*, vol. 8, no. 4, pp. 252–5, 2013.

[98] J. Valente, J.-Y. Ou, E. Plum, I. J. Youngs, and N. I. Zheludev, “A magneto-electro-optical effect in a plasmonic nanowire material,” *Nat. Commun.*, vol. 6, p. 7021, 2015.

[99] Z. Liu *et al.*, “3D conductive coupling for efficient generation of prominent Fano resonances in metamaterials,” *Sci. Rep.*, vol. 6, no. April, p. 27817, 2016.

[100] N. Papasimakis *et al.*, “The magnetic response of graphene split-ring metamaterials,” *Light Sci. Appl.*, vol. 2, no. 7, p. e78, 2013.

[101] L. Lin *et al.*, “Dielectric nanoresonator based lossless optical perfect magnetic mirror with near-zero reflection phase,” *Appl. Phys. Lett.*, vol. 108, no. 17, 2016.

[102] A. E. Nikolaenko *et al.*, “Nonlinear graphene metamaterial,” *Appl. Phys. Lett.*, vol. 100, no. 18, pp. 4–6, 2012.

[103] A. E. Nikolaenko *et al.*, “Carbon nanotubes in a photonic metamaterial,” *Phys. Rev. Lett.*, vol. 104, no. 15, pp. 3–6, 2010.

[104] A. Minovich *et al.*, “Liquid crystal based nonlinear fishnet metamaterials,” *Appl. Phys. Lett.*, vol. 100, no. 12, 2012.

[105] D. J. Cho *et al.*, “Ultrafast modulation of optical metamaterials.,” *Opt. Express*, vol. 17, no. 20, pp. 17652–17657, 2009.

[106] T. Roger *et al.*, “Coherent perfect absorption in deeply subwavelength films in the single-photon regime,” *Nat. Commun.*, vol. 6, no. May, p. 7031, 2015.

[107] J. Y. Ou, E. Plum, J. Zhang, and N. I. Zheludev, “Giant Nonlinearity of an Optically Reconfigurable Plasmonic Metamaterial,” *Adv. Mater.*, vol. 28, no. 4, pp. 729–733, 2016.

[108] S. L. Prosvirnin, V. A. Dmitriev, Y. M. Kuleshov, and V. V. Khardikov, “Planar all-silicon metamaterial for terahertz applications,” *Appl. Opt.*, vol. 54, no. 13, p. 3986, 2015.

[109] D. Maier-Schneider, a Koprululu, S. Ballhausen Holm, and E. Obermeier, “Elastic properties and microstructure of LPCVD polysilicon films,” *J. Micromechanics*, vol. 6, pp. 436–446, 1996.

[110] J. D. Jackson, “Classical Electrodynamics.” pp. 209–215, 1962.

[111] J. Dual, G. Simons, J. Villain, J. Vollmann, and C. Weippert, “Mechanical Properties of MEMS Structures,” *ICEM 12 - 12th Int. Conf. Exp. Mech.*, no. March, p. 8, 2004.

[112] K. M. Dani, Z. Ku, P. C. Upadhya, R. P. Prasankumar, S. R. J. Brueck, and A. J. Taylor, “Subpicosecond optical switching with a negative index metamaterial,” *Nano Lett.*, vol. 9, no. 10, pp. 3565–3569, 2009.

[113] Z. L. Sámson *et al.*, “Metamaterial electro-optic switch of nanoscale thickness,” *Appl. Phys. Lett.*, vol. 96, no. 14, pp. 1–3, 2010.

[114] M. J. Dicken *et al.*, “Frequency tunable near-infrared metamaterials based on VO2 phase transition,” *Opt. Express*, vol. 17, no. 20, pp. 18330–18339, 2009.

[115] R. F. Waters, P. A. Hobson, K. F. MacDonald, and N. I. Zheludev, “Optically switchable photonic metasurfaces,” *Appl. Phys. Lett.*, vol. 107, no. 8, pp. 3–6, 2015.

[116] O. Buchnev, J. Y. Ou, M. Kaczmarek, N. I. Zheludev, and V. a Fedotov, “Electro-optical control in a plasmonic metamaterial hybridised with a liquid-crystal cell.,” *Opt. Express*, vol. 21, no. 2, pp. 1633–8, 2013.

[117] M. R. Shcherbakov *et al.*, “Ultrafast All-Optical Switching with Magnetic Resonances in Nonlinear Dielectric Nanostructures,” *Nano Lett.*, vol. 15, no. 10, pp. 6985–6990, 2015.

[118] A. Karvounis, J. Y. Ou, W. Wu, K. F. Macdonald, and N. I. Zheludev, “Nano-optomechanical nonlinear dielectric metamaterials,” *Appl. Phys. Lett.*, vol. 107, no. 19, pp. 17–20, 2015.

[119] A. Karvounis, B. Gholipour, K. F. Macdonald, and N. I. Zheludev, “All-dielectric phase-change reconfigurable metasurface: Supplemental Material,” vol. 51103, pp. 3–7, 2016.

[120] B. Zeng, A. Majumdar, and F. Wang, “Tunable dark modes in one-dimensional ‘diatomic’ dielectric gratings,” *Opt. Express*, vol. 23, no. 10, p. 12478, 2015.

[121] A. P. Vasudev, J.-H. Kang, J. Park, X. Liu, and M. L. Brongersma, “Electro-optical modulation of a silicon waveguide with an ‘epsilon-near-zero’ material,” *Opt. Express*, vol. 21, no. 22, p. 26387, 2013.

[122] L. Carroll *et al.*, “Photonic Packaging: Transforming Silicon Photonic Integrated Circuits into Photonic Devices,” *Appl. Sci.*, vol. 6, no. 12, p. 426, 2016.

[123] K. Ishikawa, J. Zhang, A. Tuantranont, V. M. Bright, and Y. C. Lee, “An integrated micro-optical system for VCSEL-to-fiber active alignment,” *Sensors Actuators, A Phys.*, vol. 103, no. 1–2, pp. 109–115, 2003.

[124] M. Wuttig and N. Yamada, “Phase-change materials for rewriteable data storage,” *Nat. Mater.*, vol. 6, no. 11, pp. 824–832, 2007.

[125] B. Gholipour, J. Zhang, K. F. MacDonald, D. W. Hewak, and N. I. Zheludev, “An all-optical, non-volatile, bidirectional, phase-change meta-switch,” *Adv. Mater.*, vol. 25, no. 22, pp. 3050–3054, 2013.

[126] A. Tittl *et al.*, “A Switchable Mid-Infrared Plasmonic Perfect Absorber with Multispectral Thermal Imaging Capability,” *Adv. Mater.*, vol. 27, no. 31, pp. 4597–4603, 2015.

[127] A. K. U. Michel *et al.*, “Using low-loss phase-change materials for mid-infrared antenna resonance tuning,” *Nano Lett.*, vol. 13, no. 8, pp. 3470–3475, 2013.

[128] D. Y. Lei, K. Appavoo, F. Ligmajer, Y. Sonnefraud, R. F. Haglund, and S. A. Maier, “Optically-Triggered Nanoscale Memory Effect in a Hybrid Plasmonic-Phase Changing Nanostructure,” *ACS Photonics*, vol. 2, no. 9, pp. 1306–1313, 2015.

[129] X. Wang, D. H. Kwon, D. H. Werner, I. C. Khoo, A. V. Kildishev, and V. M. Shalaev, “Tunable optical negative-index metamaterials employing anisotropic liquid crystals,” *Appl. Phys. Lett.*, vol. 91, no. 14, 2007.

[130] B. Kang *et al.*, “Optical switching of near infrared light transmission in metamaterial-liquid crystal cell structure,” vol. 18, no. 16, pp. 16492–16498, 2010.

[131] Q. Wang *et al.*, “1.7 Gbit/in.2 gray-scale continuous-phase-change femtosecond image storage,” *Appl. Phys. Lett.*, vol. 104, no. 12, pp. 12–14, 2014.

[132] C. D. Wright, Y. Liu, K. I. Kohary, M. M. Aziz, and R. J. Hicken, “Arithmetic and biologically-inspired computing using phase-change materials,” *Adv. Mater.*, vol. 23, no. 30, pp. 3408–3413, 2011.

[133] D. Kuzum, R. G. D. Jeyasingh, B. Lee, and H. P. Wong, “Materials for Brain-Inspired Computing,” pp. 2179–2186, 2012.

[134] a Christ, S. G. Tikhodeev, N. a Gippius, J. Kuhl, and H. Giessen, “Waveguide-plasmon polaritons:

strong coupling of photonic and electronic resonances in a metallic photonic crystal slab.," *Phys. Rev. Lett.*, vol. 91, no. 18, p. 183901, 2003.

[135] A. Sobhani *et al.*, "Narrowband photodetection in the near-infrared with a plasmon-induced hot electron device," *Nat. Commun.*, vol. 4, no. August 2016, p. 1643, 2013.

[136] S. J. Kim, P. Fan, J.-H. Kang, and M. L. Brongersma, "Creating semiconductor metafilms with designer absorption spectra," *Nat. Commun.*, vol. 6, no. May, p. 7591, 2015.

[137] S. Fan, W. Suh, and J. D. Joannopoulos, "d1 h," vol. 20, no. 3, pp. 569–572, 2003.

[138] G. D'Aguanno, D. de Ceglia, N. Mattiucci, and M. J. Bloemer, "All-optical switching at the Fano resonances in subwavelength gratings with very narrow slits.," *Opt. Lett.*, vol. 36, no. 11, pp. 1984–1986, 2011.

[139] P. Lalanne and J.-P. Hugonin, "High-order effective-medium theory of subwavelength gratings in classical mounting: application to volume holograms," *J. Opt. Soc. Am. A*, vol. 15, no. 7, p. 1843, 1998.

[140] D. L. Brundrett, E. N. Glytsis, and T. K. Gaylord, "Normal-incidence guided-mode resonant grating filters: design and experimental demonstration.," *Opt. Lett.*, vol. 23, no. 9, pp. 700–702, 1998.

[141] J. Orava, A. L. Greer, B. Gholipour, D. W. Hewak, and C. E. Smith, "Characterization of supercooled liquid Ge2Sb2Te5 and its crystallization by ultrafast-heating calorimetry," *Nat. Mater.*, vol. 11, no. 4, pp. 279–283, 2012.

[142] B. Gholipour, C. C. Huang, and D. W. Hewak, "Low current consuming thermally stable sulphide phase change memory," *J. Mater. Sci. Mater. Electron.*, vol. 26, no. 7, pp. 4763–4769, 2015.

[143] B. Sa, N. Miao, J. Zhou, Z. Sun, and R. Ahuja, "Ab initio study of the structure and chemical bonding of stable Ge(3)Sb(2)Te(6).," *Phys. Chem. Chem. Phys.*, vol. 12, no. 7, pp. 1585–1588, 2010.

[144] T. Siegrist *et al.*, "Disorder-induced localization in crystalline phase-change materials.," *Nat. Mater.*, vol. 10, no. 3, pp. 202–8, 2011.

[145] D. P. San-Rom??n-Alerigi *et al.*, "Electron irradiation induced reduction of the permittivity in chalcogenide glass (As2S3) thin film," *J. Appl. Phys.*, vol. 113, no. 4, 2013.

[146] R. W. Johnson, P. B. & Christy, "Optical Constants of the Noble Metals," *Phys. Rev. B 6, 4370-4379*, 1972.

[147] K. F. Macdonald, A. V Krasavin, and N. I. Zheludev, "Optical modulation of surface plasmon-polariton coupling in a gallium / aluminium composite," vol. 278, pp. 207–210, 2007.

[148] A. D. Rakic, "Algorithm for the determination of intrinsic optical constants of metal films : application to aluminum," vol. 34, no. 22, pp. 4755–4767, 1995.

[149] G. Pflüger, J., Fink, J., Weber, W., Bohnen, K. P. & Crecelius, "Dielectric properties ofTiCx,TiNx,VCx, andVNxfrom 1.5 to 40 eV determined by electron-energy-loss spectroscopy," vol. 30, no. 3, 1984.

[150] Y. G. Chen *et al.*, "Hybrid phase-change plasmonic crystals for active tuning of lattice resonances," vol. 21, no. 11, pp. 1566–1569, 2013.

[151] M. Rudé *et al.*, "materials Optical switching at 1 . 55 l m in silicon racetrack resonators using phase change materials," vol. 141119, pp. 1–5, 2013.

[152] B. Dastmalchi, P. Tassin, T. Koschny, and C. M. Soukoulis, "A New Perspective on Plasmonics: Confinement and Propagation Length of Surface Plasmons for Different Materials and Geometries," *Adv. Opt. Mater.*, vol. 4, no. 1, pp. 177–184, 2016.

[153] Y. Liu *et al.*, “Crystallization of Ge2Sb2Te5 films by amplified femtosecond optical pulses,” vol. 123526, 2012.

[154] J. J. Vos, “Colorimetric and Photometric Properties of a 2 â€™ Fundamental Observer,” pp. 125–128, 1964.

[155] F. F. Schlich, P. Zalden, A. M. Lindenberg, and R. Spolenak, “Color Switching with Enhanced Optical Contrast in Ultrathin Phase- Change Materials and Semiconductors Induced by Femtosecond Laser Pulses,” 2014.

[156] W. Dong, Y. Qiu, J. Yang, R. E. Simpson, and T. Cao, “Wideband Absorbers in the Visible with Ultrathin Plasmonic-Phase Change Material Nanogratings,” 2016.

[157] D. G. Baranov, A. E. Krasnok, T. Shegai, A. Alù, and Y. D. Chong, “Coherent perfect absorbers: advanced structures for linear control of light with light,” *arXiv*, pp. 1–31, 2017.

[158] X. Fang, K. F. MacDonald, and N. I. Zheludev, “Controlling light with light using coherent metadevices: all-optical transistor, summator and invertor,” *Light Sci. Appl.*, vol. 4, no. February, p. e292, 2015.

[159] J. M. Rothenberg *et al.*, “Experimental demonstration of coherent perfect absorption in a silicon photonic racetrack resonator,” *Opt Lett*, vol. 41, no. 11, pp. 2537–2540, 2016.

[160] Z. J. Wong *et al.*, “Lasing and anti-lasing in a single cavity,” *Nat. Photonics*, vol. 10, no. 12, pp. 796–801, 2016.

[161] R. Bruck and O. L. Muskens, “Plasmonic nanoantennas as integrated coherent perfect absorbers on SOI waveguides for modulators and all-optical switches,” *Opt. Express*, vol. 21, no. 23, pp. 27662–7, 2013.

[162] A. K. Jahromi and A. F. Abouraddy, “Coherent perfect absorption in a weakly absorbing fiber,” *arXiv:1706.04968v1*, vol. 40, no. 23, pp. 5550–5553, 2017.

[163] X. Fang, M. L. Tseng, J.-Y. Ou, K. F. Macdonald, D. P. Tsai, and N. I. Zheludev, “Ultrafast all-optical switching via coherent modulation of metamaterial absorption Ultrafast all-optical switching via coherent modulation of metamaterial absorption,” *Appl. Phys. Lett.*, vol. 104, p. 141102, 2014.

[164] Q. P. Su *et al.*, “Generating double NOON states of photons in circuit QED,” *Phys. Rev. A*, vol. 95, no. 2, pp. 1–9, 2017.

[165] Y. D. Chong, L. Ge, H. Cao, and A. D. Stone, “Coherent perfect absorbers: Time-reversed lasers,” *Phys. Rev. Lett.*, vol. 105, no. 5, pp. 1–4, 2010.

[166] L. Baldacci, S. Zanotto, G. Biasiol, L. Sorba, and A. Tredicucci, “Interferometric control of absorption in thin plasmonic metamaterials: general two port theory and broadband operation,” *Opt. Express*, vol. 23, no. 7, p. 9202, 2015.

[167] S. Dutta-Gupta, O. J. F. Martin, S. Dutta Gupta, and G. S. Agarwal, “Controllable coherent perfect absorption in a composite film,” *Opt. Express*, vol. 20, no. 2, p. 1330, 2012.

[168] J. Zhang, K. F. MacDonald, and N. I. Zheludev, “Controlling light-with-light without nonlinearity,” *Light Sci. Appl.*, vol. 1, no. 7, p. e18, 2012.

[169] X. Fang, M. L. Tseng, D. P. Tsai, and N. I. Zheludev, “Coherent Excitation-Selective Spectroscopy of Multipole Resonances,” *Phys. Rev. Appl.*, vol. 5, no. 1, pp. 1–7, 2016.

[170] I. Aharonovich, A. D. Greentree, and S. Prawer, “Diamond photonics,” *Nat. Photonics*, vol. 5, no. 7, pp. 397–405, 2011.

[171] M. J. Burek *et al.*, “Free-standing mechanical and photonic nanostructures in single-crystal diamond,”

Nano Lett., vol. 12, no. 12, pp. 6084–6089, 2012.

[172] M. A. Draganski *et al.*, "The effect of gallium implantation on the optical properties of diamond," *Diam. Relat. Mater.*, vol. 35, pp. 47–52, 2013.

[173] S. Rubanov and A. Suvorova, "Ion implantation in diamond using 30 keV Ga + focused ion beam," *Diam. Relat. Mater.*, vol. 20, no. 8, pp. 1160–1164, 2011.

[174] J. F. F.Zeigler and J. P. Biersak, "SRIM2008." .

[175] V. Nalla, S. Vezzoli, V. João, S. Handong, and N. Zheludev, "100 THz optical switching with plasmonic metamaterial," in *European Conference on Lasers and Electro-Optics - European Quantum Electronics Conference*, 2015.

[176] G. C. Cho, T. Dekorsy, H. J. Bakker, R. Hövel, and H. Kurz, "Generation and Relaxation of Coherent Majority Plasmons," *Phys. Rev. Lett.*, vol. 77, no. 19, pp. 4062–4065, 1996.

[177] M. Hase, S. Nakashima, K. Mizoguchi, H. Harima, and K. Sakai, "Ultrafast decay of coherent plasmon-phonon coupled modes in highly doped GaAs," *Phys. Rev. B*, vol. 60, no. 24, pp. 16526–16530, 1999.

[178] J. Orloff, "Fundamental limits to imaging resolution for focused ion beams," *J. Vac. Sci. Technol. B Microelectron. Nanom. Struct.*, vol. 14, no. 6, p. 3759, 1996.

[179] H. G. Tompkins, *Handbook of Ellipsometry*, vol. 30, no. 7. 2005.

[180] "https://en.wikipedia.org/wiki/Ellipsometry."

[181] "http://www.craictechnologies.com."

[182] L. Liu, L. Kang, T. S. Mayer, and D. H. Werner, "Hybrid metamaterials for electrically triggered multifunctional control," *Nat. Commun.*, p. 13236, 2016.

[183] I. M. Pryce, K. Aydin, Y. A. Kelaita, R. M. Briggs, and H. A. Atwater, "Highly strained compliant optical metamaterials with large frequency tunability," *Nano Lett.*, vol. 10, no. 10, pp. 4222–4227, 2010.